EXTENDED TARGET TRACKING METHODS

IN MODERN SENSOR APPLICATIONS

EXTENDED TARGET TRACKING METHODS IN MODERN SENSOR APPLICATIONS

BY

MEHRNOOSH HEIDARPOUR, B.Sc.

A THESIS

SUBMITTED TO THE DEPARTMENT OF ELECTRICAL & COMPUTER ENGINEERING

AND THE SCHOOL OF GRADUATE STUDIES

OF MCMASTER UNIVERSITY

IN PARTIAL FULFILMENT OF THE REQUIREMENTS

FOR THE DEGREE OF

DOCTOR OF PHILOSOPHY

Doctor of Philosophy (2020)

(Electrical & Computer Engineering)

McMaster University

Hamilton, Ontario, Canada

TITLE: Extended Target Tracking Methods In Modern Sensor Applications

AUTHOR: Mehrnoosh Heidarpour

B.Sc. (Electrical and Computer Engineering),

Islamic Azad University (Najafabad Branch), Isfahan, Iran

SUPERVISOR: Prof. T. Kirubarajan

NUMBER OF PAGES: xx, 193

Abstract

With the recent advances in sensor technology and resulting sensor resolution, conventional point-based target tracking algorithms are becoming insufficient, particularly in application domains such as autonomous vehicles, visual tracking and surveillance using high resolution sensors. This has renewed the interest in extended target (ET) tracking, which aims to track not only the centroid of a target, but also its shape and size over time.

This thesis addresses three of the most challenging problems in the domain of ET tracking applications. The first investigated challenge is the need for an accurate shape and centre estimate for the ET object with an arbitrary unknown star-convex shape in presence of non-Gaussian noise. The proposed method is based on a Student's-t process regression algorithm which is defined in a recursive framework to be applicable for on-line tracking problems.

The second problem tries to relax any constraints, including the star-convex constraint, that is imposed on the shape of the ET object during the course of estimation by defining a novel Random Polytopes shape descriptor. Also, the proposed solution introduces a method to mitigate the troubles caused as a result of self-occlusion in ET tracking applications which its ignorance may cause catastrophic divergence in the ET state estimate.

Finally, a framework for tracking multiple ET objects in the presence of clutter and occlusion is studied and a solution is proposed. The proposed method can estimate the centre and shape of the ET objects in a realistically scenario with the self- and mutual-occlusion challenges being considered. The proposed approach defines a time varying state-dependent probability of detection for each ET that enables the track to prolong even under adverse conditions caused due to mutual-occlusion. Plus, the proposed algorithm uses set-membership uncertainty models to bound the association and target shape uncertainties of occluded ET, to obtain more accurate state and shape estimates of an ET object.

The performance of the proposed methods are quantified on realistically simulated scenarios with self- and mutual-occlusions and their results are compared against existing state-of-the-art methods for ET tracking applications.

To my family

Acknowledgements

I would like to use this opportunity to express my great appreciation to my supervisor, Prof. T. Kirubarajan, first and for most for offering me the Ph.D. program in McMaster university while I was only looking for M.Sc. program, for supporting me financially and emotionally and for all the academical guidance and suggestions through journey of this research. Working under his supervision is one of my deepest honours.

I want to appreciate Dr. R. Tharmarasa, for his unconditional, through and creative advices during these three years. I have learnt most of the knowledge in the field of tracking and estimation in sensor applications in the course of working with him and taking his courses. Also, I want to thank and express my sincere gratitude to my committee members, Prof. I. Bruce and Prof. J. Chen, for all of their generous and helpful suggestions during my degree journey. I appreciate all the time that they have spent on my supervisory meetings and reading my thesis. I feel a need to thank our sponsors and collaborator from L3Harris Wescam, specially Dr. M. Bradford, for sharing their knowledge on the real-world problems and solution techniques covered in this thesis. I also want to thank Prof. J. Thiyagalingam for his valuable help and comments on my research papers.

I want to thank all my dear friends in lab, specially, Tongyu and Ben, for the help

and support during these three years journey of Ph.D. degree. I am pleased to be a part of Electrical and Computer Engineering department and want to express my deepest gratitude for it's administrative staffs, particularly, Ms. C. Gies and Ms. T. Coop.

Finally, I like to express my sincere gratitude and thanks to my mother, my father and my brother for their consistent support and love through all these years.

Contents

List of Figures

List of Tables

Abbreviations

Abbreviations

ET   Extended target

FoV   Field of view

RM   Random matrices

IW   Inverse Wishart

RHM   Random hypersurface models

GP   Gaussian process

EKF   Extended Kalman filter

GP-EKF   Gaussian process based Extended Kalman filter

PDA   Probabilistic Data Association

3D   3 dimensional

SE   Squared exponential

IW	Inverse Wishart
TP	Student's-t process
TP-EKF	Student's-t process based Extended Kalman filter
PCRLB	Posterior Cramer-Rao lower bound
ETT	Extended target tracking
RFS	random finite sets
PHD	Probability hypothesis density
CPHD	Cardinalized probability hypothesis density
GM-PHD	Gaussian mixture probability hypothesis density filter
ET-GM-PHD	Extended target Gaussian mixture probability hypothesis density
ET-GM-CPHD	Extended target Gaussian mixture cardinalized probability hypothesis density
σ-**GLMB**	σ-generalized labeled multi-Bernoulli
PMBM	Poisson multi Bernoulli mixture
PSD	Positive semi-definite
$\mathcal{MVT}$	Multivariate Student's-t distribution
MMSE	Minimum mean square error

STF   Student's-t filter

GSTF   Generalized student's-t filter

MSE   Mean square error

PFIM   Posterior Fisher information matrix

VB   Variational Bayes

IOU   Intersection-Over-Union

RMSE   Root mean square error

RP   Random Polytope

LIDAR   Light detection and ranging

LS   Level-Sets

RP-EKF   Random Polytope extended Kalman filter

GAM   Greedy association method

p_D Probability of detection

PMHT   Probabilistic multiple hypothesis tracking

GLMB   Generalized labelled multi-Bernoulli

PMVB   Poisson mixture variational Bayesian

S-GGM-PHD)

                    Spline gamma Gaussian mixture probability hypothesis density filter

EM	Expectation-Maximization
m-OSPA	Modified optimal sub-pattern assignment
CPEP	Circular position error probability

Declaration of Academic Achievement

This research presents analytical and computational work carried out solely by Mehrnoosh Heidarpour, herein referred to as "the author", with advice and guidance provided by the academic supervisor Prof. T. Kirubarajan. Information that is presented from out-side sources which has been used towards analysis or discussion, has been cited when appropriate, all other materials are the sole work of the author.

Chapter 1

Introduction

1.1 Extended Target Tracking: A Brief Review

One of the main assumptions in target tracking algorithms is that each target can generate at most one measurement per scan. This is the so called famous point target tracking problem. This assumption may be true in situations where the distance between the target and sensor is considerably large or the sensor resolution is not high enough for the target to occupy more than one cell in the sensor's field of view (FoV). But, for long-range applications involving high resolutions modern sensors, such as airborne surveillance, or short-range applications, such as autonomous vehicles, this assumption does not hold true and the target will generate multiple measurements per scan. Figure (1.1) represents the measurements generated from a point target versus an extended target (ET). The point target only resulted in a single measurement whereas the extended target has resolved into multiple scattering points and only some of the scattering points have generated measurements.

Thus, the need for an ET tracking method to handle this situation arises. ET

(a) Point target   (b) Extended target

Figure 1.1: A side-by-side comparison of Point and Extended target. (a): Single source of measurement for a point target and generated measurement. (b): Multiple scattering points and generated measurements from ET.

tracking has applications in several areas including airborne, marine and ground surveillance using high-resolution sensors, such as radar and lidar, autonomous vehicular systems and in video tracking.

The ET tracking algorithms are not only capable of estimating the trajectory of centre of the target but also its size, shape and orientation over time. This additional information about targets can be exploited as input to classification and decision making algorithms. The literature on ET tracking problems is considerably rich. In general three main lines of works to solve the ET tracking problem can be seen in literature.

The first line of work focuses on clustering the observations in each scan and replacing all the measurements in each cluster by a single measurement such as the centroid of the cluster. From there after, these algorithms treat the problem similar to the conventional point target tracking case [1, 2]. In contrast to its simplicity, the major drawback of this approach is that it removes some crucial information about targets such as their shape and orientation through the clustering procedure.

Algorithms belonging to the second line of work try to model the observations generated by targets over the sensor's FoV by some spatial distribution such as a Poisson point process [3, 4, 5]. In these situations the number of observations from the

ET is assumed to be Poisson distributed. Based on this approach Poisson likelihood models for group and extended object tracking were developed. Also, some methods for tracking single extended objects based on random-set techniques are proposed in [6].

The last and most extensive approach in dealing with ET objects is trying to model the ET object extent by simple or sometimes complex geometrical shapes, such as sticks, rectangle and ellipse, and estimate shape parameter by construction of feasible measurement to source assignment hypotheses and their probabilities. Some of the well-known methods belonging to this category are reviewed in the following paragraphs.

In [7], a Bayesian approach, called the random matrices (RM) method, is used to simultaneously estimate the elliptical contour and kinematic state of the ET. The RM method models the extended state by using an inverse Wishart (IW) distribution. This method offers notable performance on ET tracking problems and a number of enhanced versions of this algorithm has also been introduced. For example in [8], a generalized algorithm for estimating ET objects whose its shape can not be modelled with one ellipse is proposed. In this algorithm, the ET object extent is modelled by using N_s elliptic sub-objects, where N_s is assumed known. In [9] the RM method is extended further to handle multiple ET objects in the presence of measurement origin uncertainty by introducing a RM based labelled random finite sets filter. The other proposed method, which belongs to shape-based ET tracking algorithms category, is the random hypersurface model (RHM) [10]. The RHM method relies on the Fourier series expansion of the contour, and different sampling of the contour as the source of measurement.

Another shape-based approach to estimate the ET extent along with the its kinematics through a Bayesian framework, introduced in [11], is to use the Gaussian process (GP). Here, the ET object shape is assumed to be star-convex which can be represented with the help of a radial basis function by means of GP, which underpins a GP-based extended Kalman filter (GP-EKF) algorithm. The GP-EKF algorithm has been used as a basis for some extensions, such as a GP based probabilistic data association (PDA) filter and a GP convolution particle filter in [12, 13], respectively.

B-spline curves, which are a generalized version of Bèzier curves, have also drawn some attention in recent years in the field of ET tracking and shown promising results in modelling the extent of ET objects [14, 15, 16].

Although modeling the contour with a geometrical shape has received considerable effort, existing algorithms are still limited regarding the assumptions about the environment, sensing capability of sensors and problem formulation.

One of the major assumptions in previously proposed ET tracking algorithm is that the system is corrupted with a well-known Gaussian noise. However, the majority of the real-world problems seldom adhere to the assumptions of Gaussian noise models. Thus, the performance of the existing algorithms, with Gaussian noise assumption degrades in the presence of non-Gaussian noise with the problem ascribed to the lightweight tail of the Gaussian distribution [17]. In fact, this problem is commonly seen in high quality sensors which are mainly used in ET tracking applications, such as visual tracking sensors, high resolution radars and robotic platforms [18].

The other base-line assumption of most of the proposed algorithms is that the ET object shape falls in a predefined category, which is known prior. For example the RM method proposed in [7] assumes only elliptical objects are present in the
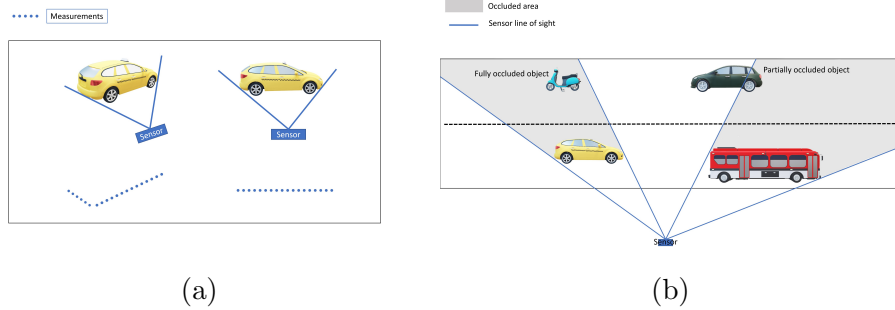
Figure 1.2: (a): Self-occlusion phenomena in ET objects; (b): Mutual occlusion in a road surveillance framework.

scenario. GP-EKF and RHM method have relaxed the shape constraint more to fall in category of star-convex shape. However, the constraint still remains and makes the algorithms inaccurate for applications involving non-convex ET objects. Extension of ET tracking algorithm to handle 3 dimensional (3D) spaces is also another drawback of existing algorithms.

For an ET object, as well as different sections of the object, the necessary condition to be observable by a sensor is that sensor's line of sight should be clear and not blocked either by another or the same object. Self-occlusion [19] happens when some parts of the object is blocking another part of the same object. Whereas, the occlusions caused by a different object is called mutual-occlusion [20]. Figure 1.2 illustrates the self- and mutual-occlusions in a road surveillance framework.

The negligence of the loss of detection due to mutual-occlusion results in track loss, when a new track following the same target is initialized and confirmed after several frames for the same object and leaving a gap between these two confirmed track with different labels [21]. This is one of the difficulties in multiple object tracking applications for which some solutions have been proposed in [22, 23, 24], which mainly focuses on the visual feature extracted from video data and are not

applicable in applications using radar and lidar sensors.

In contrast to mutual-occlusion, self-occlusion has not received much attention in previous works and ignoring it may cause large errors in ET object shape, size and orientation estimation. Consequently, the algorithm which uses these data as their input such as classification and decision making algorithms will have large errors as well.

In this thesis, we address some of the aforementioned flaws in existing ET tracking algorithms by relaxing some of the assumptions and formulating the problem closer to its true nature, to make them more applicable for real world applications.

1.2   Theme and Objectives of Dissertation

In compliance with the terms and regulations of McMaster University, this dissertation has been written in sandwich thesis format by assembling three articles. These articles represent the independent research performed by the author of this dissertation, Mehrnoosh Heidarpour.

The articles in the dissertation are focused on extended target tracking methods for modern sensor applications under realistic conditions. The general focus of the thesis is as follows:

i) To introduce a geometrical shape descriptor for representing the extent of ET object, which is appropriate for being formulated in a Bayesian framework and being estimated online (Paper I, Paper II and Paper III).

ii) To derive an ET tracking framework appropriate for realistic sensor and system noise models, specially for heavy tailed noise (Paper I).

iii) To introduce a novel shape-descriptor, which is free from any constraints in terms of convexity and space dimensions, suitable for using in an ET tracking framework (Paper II).

iv) To address the self-occlusion trouble existing in ET tracking scenarios by defining observable and non-observable sections of tracked ET objects (Paper II and Paper III).

v) To analyse the multiple ET object tracking scenario in presence of false alarm and measurement origin uncertainty (Paper III).

vi) To address the challenges caused by mutual-occlusion in ET tracking applications and improve estimation results (Paper III).

1.3   Summary of Enclosed Articles

The papers included in this thesis are listed as follows:

1.3.1   Paper I (Chapter 2)

Mehrnoosh Heidarpour, Ratnasingham Thamarasa, Jeyarajan Thiyagalingam, Michael Bradford and Thiagalingam Kirubarajan
"Extended Target Tracking Using Student's-t Process With Heavy-Tailed Process and Measurement Noises", Submitted to IEEE Transactions on Signal Processing, May. 2020.
Preface: This paper studies the ET tracking problem by representing the shape of a star-convex ET object with a radial function which is modelled using a Student's-t

process (TP). TP has several benefits compared to the conventional Gaussian process (GP). First of all, since the TP relies on a non-stationary kernel function it is more suitable for modeling the shape of an ET object which is evolving in time compared to the GP that has a stationary kernel function and its performance degrades when the shape evolves or measurements are arising from interior of object as well as the contour of object. In the paper an online, state-space model-based, recursive version of the TP regression algorithm is derived which can be used in a Bayesian setting to estimate the kinematic state of ET object which is augmented by the extent state. Another property of resulting TP filter is that the tails of Student's-t distribution, which are modeling the noise, are heavier compared to the light-tails of Gaussian distribution and can reject the outliers (glint-noise). This property matches the real-world problems underlying noise model, which hardly adhere to the assumptions of Gaussian noises. A novel gating algorithm is derived in the paper to enable the proposed TP based filter to be used in the presence of clutter. The efficiency of the proposed filter is quantified by comparing the results with previously proposed algorithms and also a conditional-Posterior Cramer-Rao lower bound (PCRLB).

1.3.2   Paper II (Chapter 3)

Mehrnoosh Heidarpour, Jeyarajan Thiyagalingam, Ratnasingham Thamarasa, Michael Bradford and Thiagalingam Kirubarajan
"Two- and Three-Dimensional Extended Target Tracking Using Random Polytopes", Submitted to IEEE Transactions on Aerospace and Electronic Systems, August 2020.
Preface: This paper studies the ET tracking problem by representing the shape of an arbitrary ET object with Random Polytopes (RP) shape descriptor. The novel

proposed RP shape descriptor has several benefits compared to the state-of-the-art shape descriptors used to model the extent of the ET objects in the literature. First of all, there is no constraint on the shape of the ET object and it can vary among all arbitrary random non-convex shapes. The second benefit of using RP in ET tracking algorithm is a result of the information which RP provides to mitigate the challenges caused due to self-occlusion. In the paper an online, auxiliary probability of detection is assigned to different parts of each ET object for considering the effects of observable and non-observable parts of ET object in the received measurements. Also, a new metric to evaluate the similarity between the estimated shape and true shape of ET object is proposed and is calculated for comparison purposes. The efficiency of the proposed filter, in terms of the kinematic and extent estimates and tolerance to the different noise levels is quantified by comparing the results with two existing state-of-the-art ET tracking methods and the Posterior Cramer-Rao lower bound (PCRLB).

1.3.3   Paper III (Chapter 4)

Mehrnoosh Heidarpour, Ratnasingham Thamarasa, Michael Bradford, Jeyarajan Thiyagalingam and Thiagalingam Kirubarajan
"Tracking Multiple Extended Targets In Occlusion Using Splines and Set-Membership Uncertainty Models", Submitted to IEEE Transactions on Signal Processing, July 2020.
Preface: This paper studies the multiple ET tracking problem in the presence of measurement origin uncertainty, clutter and occlusions. In the proposed algorithm, that is called the splines gamma Gaussian mixture probability hypothesis density (S-GGM-PHD) filter, the shape of the ET object is replaced with the B-splines approximation.

The local controllability of shapes approximated by B-splines is exploited by the proposed method to mitigate the challenges caused due to self-occlusion in ET tracking application. To deal with the difficulties in estimating the true state of ET objects caused due to mutual-occlusion an online state-dependent probability of detection is defined and used in the update step of the proposed filter in contrast to a constant state-independent probability of detection that is used in the previous state-of-the-art ET tracking algorithms. The set-membership uncertainty models are used in the proposed algorithm to bound the uncertainties associated in the estimation of occluded ET objects. The efficiency of the proposed algorithm, in terms of the the kinematic state estimates, the extent state estimates and the track continuity under adverse conditions caused by occlusion is quantified by comparing the results with two existing state-of-the-art ET tracking methods.

Chapter 2

Extended Target Tracking Using Student's-t Process With Heavy-Tailed Process and Measurement Noises

2.1 Abstract

With the recent advances in sensor technology and resulting sensor resolution, conventional point-based target tracking algorithms are becoming insufficient, particularly in application domains such as autonomous vehicles, visual tracking and surveillance using high resolution sensors. This has renewed the interest on extended target tracking, which aims to track not only the centroid of a target, but also its shape and size

over time. On this problem, Gaussian process (GP)-based extended target tracking algorithms have played an important role, and have been central to the solution space, often with numerous extensions and enhancements. However, the main limitation of the GP, which relies on the squared exponential (SE) kernel, is its inability to completely and correctly model the target extent over time.

In this chapter, by using an Inverse Wishart (IW) distribution as a prior to the SE kernel of the GP, we propose a novel extended target tracking algorithm that addresses the shortcomings of the GP-based filters. Our approach, which prefixes the SE kernel with an IW kernel, results in the Student's-t process (TP), which becomes an ideal option for handling heavy-tailed noise conditions. By carefully formulating and constructing necessary mathematical foundations, we develop a rather sophisticated filter, which we refer to as TP-EKF (T-Process Extended Kalman Filter), to work in the extended target tracking setting. Our simulation studies show that the proposed TP-EKF can outperform a number of contemporary filters, including GP-EKF, Random Matrices, and Random Hypersurface Models-based extended target tracking algorithms, both in terms offering near (conditional) posterior Cramér-Rao Lower Bound (PCRLB) performance, and better shape estimation, including under heavy-tailed noise conditions, and clutter.

2.2   List of Notations

Throughout this chapter, scalars or scalar-valued functions are denoted with non-bold symbols, e.g., y_k, vectors or vector-valued functions are denoted with bold symbols, e.g., $\mathbf{u}_k$, and matrices are denoted with capitalized symbols, e.g., A. Furthermore, a list of some of the notations used through this chapter and their explanations are

listed below.

A Positive definite matrix

μ Mean of distribution

v Degree of freedom of distribution

K Kernel matrix of distribution

$f(u)$ Real-valued function

$\mathbf{y}_k$ Noisy measurement of the function f

$\mathbf{u}_k$ Corresponding inputs of function f for measurement $\mathbf{y}_k$

$\mathbf{u^f}$ Test inputs

$\kappa(u, u')$ Kernel function of distribution

$\mathcal{X}_k$ Augmented target state

$\mathbf{x}_k$ Target center kinematic state

$\mathbf{x}_k^s$ Target extent state

$\mathbf{x}_k^{center}$ Target center state

$f_k(\theta)$ ET radial function at input θ

s_k Contour scaling factor at time k

$\mathbf{o}_k^j$ Orientation vector

H Gradient of the measurement function h_k^j

2.3 Introduction

With recent advances in sensor technologies, receptive resolution of modern sensors has improved so much that they can easily capture the extended nature of objects. The ability to track extended targets, or extended target tracking (ETT), has a number of applications in several areas including airborne, marine and ground surveillance using high-resolution sensors, autonomous vehicular systems and in video tracking. In ETT, objects can no longer be modeled as point targets, and the assumption of one measurement per target (even under ideal conditions) no longer holds. In fact, the ETT algorithms are required not only to estimate the trajectory of a given target, but also the size, shape, and orientation over time. As such, ETT algorithms are considerably more intricate than conventional tracking algorithms.

The literature on ETT methods is considerably rich. One common approach is to rely on the measurement partitioning technique [25, 26, 27, 28, 29, 30], which aims to explicitly avoid data association. The majority of these techniques are underpinned by random finite sets (RFS). For instance, PHD-filter [25], and its derivatives, including the cardinalized probability hypothesis density (CPHD) filter [26], extended target Gaussian mixture PHD filter (ET-GM-PHD) [28], extended target Gaussian mixture CPHD filter (ET-GM-CPHD) [27], and other filtering methods, essentially operate on this principle. Here, the PHD and the CPHD filters explicitly avoid the data association step by moment approximation while the σ-generalized labeled multi-Bernoulli (σ-GLMB) [30] and the Poisson multi-Bernoulli mixture (PMBM) in [29] filters explicitly avoid the data association uncertainty by developing conjugate multitarget distributions.

In addition to this, another successful family of methods rely on the modeling

14

of the scattering points of extended targets using some spatial distribution [7, 10, 31, 32, 33]. In such algorithms, the kinematic state and extent of the target are tracked simultaneously. In [7], a Bayesian approach, called the Random Matrices (RM) method, is used to simultaneously estimate the elliptical contour and kinematic state of the target. RM method models the extended state by using an Inverse Wishart (IW) distribution. This method offers notable performance on ETT problems, and a number of enhanced versions of this algorithm can be found in [10, 31, 32, 33]. A version of the extended algorithm is in [31], where any non-ellipsoidal target shape is represented by a combination of multiple ellipsoidal sub-objects, each represented by a random matrix. Another extension of this model is the random hypersurface model (RHM) [10]. The RHM method outperforms the original RM method, by relying on the Fourier series expansion of the contour, and different sampling of the contour as the source of measurement. This sampling-based approach provides a means for covering the interior scattering points of the extended target. There have also been some attempts to incorporate the RM approach into PHD and GLMB filters, such as the GIW-PHD and GGIW-GLMB filters presented in [32] and [33].

Another way to estimate the target contour along with the target kinematics, introduced in [11], is to use the Gaussian process (GP) to define the target contour function. Here, a radial basis function of a star-convex shape is defined by means of a GP, which underpins a GP-based EKF (GP-EKF) algorithm. The GP-EKF algorithm has been used as a basis for many extensions, such as [12, 13], particularly to handle scenarios characterized by clutter and measurement origin uncertainty. For example, in [12], a GP-PDA filter has been developed to facilitate track an extended target with measurement origin uncertainty. In [13], a GP convolution particle filter

for multiple extended targets has been proposed.

One of the shortcomings of the GP-EKF algorithm [11] is its susceptibility for errors when the measurements originate from the target surface rather than from the contour, leading to a sub-optimal performance on the kinematic state estimation when compared against RM or RHM methods [10]. The GP-EKF algorithm, which is derived from GP, inherently relies on the covariance function to capture the assumptions and properties of the function being learned [34]. A closer inspection of the raw GP algorithm reveals that a squared exponential (SE) function, a Gaussian kernel, is used as the covariance function. Albeit being simple, the SE function is not sophisticated enough to learn complex or hidden features. Thus, by using an appropriate and/or problem-specific kernel, the overall tracking performance can be improved [13].

This chapter aims to overcome this shortcoming by proposing a new kernel function to enhance the overall ETT performance. More specifically, we propose prefixing the standard SE kernel of a GP with an IW kernel. Given the role and importance of the IW distribution in other methods, such as RM, and its capability to properly model the densities of the target extent [35], IW is a logical choice. However, prefixing the SE kernel with an IW kernel makes the GP become Student's-t process (TP) [36]. The resulting TP has a number of properties that are ideal for our case. However, in order to leverage those properties in an ETT context, a number of formulations must be considered. In our case, this transformation yields a particular benefit regarding noisy measurements, due to the capabilities of the TP to handle heavy-tailed (glint) noise cases [37]. The majority of the real-world problems seldom adhere to the assumptions of Gaussian noise models. For instance, the performance of the GP-based

16

EKF algorithm [11], degrades in the presence of non-Gaussian noise — with the problem ascribed to the lightweight tail of the Gaussian distribution [17]. In fact, this problem is commonly seen in high quality sensors, such as visual tracking sensors, high resolution radars and robotic platforms [18]. Although, several other non TP-based approaches, such as [38, 39, 40], have been proposed to overcome these heavy-tailed cases, they are often impractical in real-world cases, owing to the computational complexities. Apart from exploiting TP for handling heavy-tailed noise conditions, TP has also successfully been used to model uncertainties [41, 42, 43, 44, 45, 46]. In fact, there is growing interest in using TP as an alternative to GP, which can be found in several application areas ranging from data mining, to machine learning, to economics and statistics [47, 48, 49, 50, 51, 52, 53].

In utilizing the TP in place of GP for handling ETT problems, we make the following key contributions:

1. We propose to use prefix the standard SE kernel with an IW distribution, so as to transform the GP regression algorithm into a TP regression algorithm to model the target shape;

2. We derive an online, state-space model-based, recursive version of the TP regression algorithm, called TP-EKF, allowing the target extent to be augmented by the target kinematic state;

3. We develop a TP-based measurement model that can be embedded as part of the TP-EKF algorithm to estimate the augmented state;

4. We develop a modified gating technique to enable the TP-EKF algorithm to be used in the presence of clutter; and

5. We develop a recursive, TP-EKF-aware, conditional PCRLB model to evaluate the efficiency of the proposed TP-EKF algorithm.

The rest of this paper is organized as follows: In Section 2.4, we provide the necessary background by introducing the properties of the IW distribution and derive the TP from GP with IW as a prior. We then state and formulate the problem in Section 2.5 by developing a recursive TP to be used in the proposed ETT algorithm along with a TP-based augmented target state and a measurement model for the extended target. This is then followed by Section 2.6, where we introduce the TP-EKF algorithm to compute the posterior distribution of a target state and discuss some of the crucial aspects that underpin the TP-EKF. In Section 2.8, we formulate the gating algorithm to work with the proposed TP-EKF algorithm, and a recursive, online version of the conditional PCRLB so that the overall RMSE errors resulting from the TP-EKF can be compared. We then present the the evaluation results in Section 2.10, before concluding the chapter in Section 2.11.

2.4   Student's-t Process

This section is devoted to the development of TP with an IW inserted prior to the SE kernel. The online recursive TP, which is necessary for online applications of TP regression, has been developed for use in the proposed filter.

2.4.1   Inverse Wishart Distribution

For an $n \times n$ symmetric, real valued and positive definite matrix A, the Wishart distribution with parameter v and positive semi-definite (PSD) kernel K is given

by [54]

$$\mathcal{W}(A; v, K) = c_n(v, K)|A|^{(v-n-1)/2} \exp\left(-\frac{1}{2}\mathbf{tr}\left(K^{-1}A\right)\right), \qquad (2.4.1)$$

for $v > n - 1$, $\mathbf{tr}$ denotes the trace operator and c_n is given by

$$c_n(v, K) = \left(|K|^{\frac{v}{2}} 2^{\frac{vn}{2}} \Gamma\left(\frac{v}{2}\right)\right)^{-1}. \qquad (2.4.2)$$

One of the attractive properties of the Wishart density is that any $n_1 \times n_1$ $(n_1 < n)$ sub-matrix A' of A itself follows the same Wishart distribution. i.e., $A' \sim W_n(v, K')$. However, for defining positive definite process with Wishart distribution, the parameter v should become infinity. This particular property renders the direct Wishart distribution being less useful as a prior over nonparametric Bayesian modeling such as GP [35]. However, the IW distribution, which has the same properties as those of the direct Wishart distribution, does not suffer from this drawback. The IW distribution, for a real valued positive definite matrix A, is defined as

$$\mathcal{IW}(A; v, K) =$$
$$c_n(v, K)|A|^{-(v+2n)/2} \exp\left(-\frac{1}{2}\mathbf{tr}\left(KA^{-1}\right)\right), \qquad (2.4.3)$$

where $v > 2$ and c_n is defined as

$$c_n(v, K) = \frac{|K|^{(v+n-1)/2}}{2^{(v+n-1)n/2}\Gamma_n\left((v+n-1)/2\right)}. \qquad (2.4.4)$$

The fact that the parameter v is independent of the size of X ensures that the

marginalization step in the Bayesian modeling will not encounter any computational issues. The first and second moments of this distribution can be found in [54].

2.4.2   Student's-t Distribution

A Student's-t random variable A can be characterized by a multivariate Student's-t distribution ($\mathcal{MVT}$), characterized by a degree of freedom v, its mean $\mu = \mu(A)$, and a PSD kernel K, as follows:

$$\mathcal{MVT}(A; \mu, v, K) = \frac{\Gamma(\frac{v+n}{2})}{\Gamma(\frac{v}{2})} \times$$

$$\frac{1}{((v-2)\pi)^{\frac{n}{2}}} |K|^{-\frac{1}{2}} \left(1 + \frac{(A-\mu)^T K^{-1}(A-\mu)}{v-2}\right)^{-\frac{v+n}{2}}. \qquad (2.4.5)$$

2.4.3   Embedding Gaussian Kernel into the Student's-t Process

In [11], it was shown that by using GP, one can model the extent of a large variety of objects in target tracking applications, and it demonstrated the possibility of applying the GP for modeling the contour of extended targets. However, the underlying kernel of the GP, namely, the SE, encodes only the prior knowledge about the contour and nothing about the interior of the targets. As such, this algorithm can be sub-optimal for measurements coming from the interior points of the targets. However, IW distribution is used to represent the target extents in RM algorithm [7]. The hypothesis is that, if the same can be applied in the context of GP-based ETT algorithms, a better ETT algorithm can be derived. More specifically, IW is incorporated as part of the kernel function of the GP. However, the GP-based tracking algorithms predominantly

use the SE kernel for modeling the contour characteristics. Motivated by the discussions in [36], we propose to use the IW kernel in conjunction with the SE kernel, so that both exterior and interior measurements can be accounted for during tracking. To formulate this, consider a real valued random function f such that $f : u \to R$. The traditional GP process with kernel function κ is used in conjunction with IW distribution, such that

$$
\begin{aligned}
\Omega &\sim \mathcal{IW}(v, K(\boldsymbol{u}, \boldsymbol{u}')) \\
f(\boldsymbol{u})|\Omega &\sim \mathcal{GP}(\mu(\boldsymbol{u}), (v-2)\Omega).
\end{aligned}
\tag{2.4.6}
$$

Given that IW is a conjugate prior for the kernel of GP, under marginalization, for given data $f(\boldsymbol{u})$ where $\mu(\boldsymbol{u}) = (\mu(u_1), \mu(u_2), \ldots, \mu(u_n))$, one can derive

$$
p\left(f(\boldsymbol{u})|v, K\right) = \int p\left(f(\boldsymbol{u})|\Omega\right) p\left(\Omega|v, K\right) d\Omega.
\tag{2.4.7}
$$

which, when using the IW distribution, can be expressed as

$$
\begin{aligned}
p(f(\boldsymbol{u})|v, K) &\propto \\
&\int \frac{\exp(-\frac{1}{2}\mathbf{tr}((K + \frac{(f(u)-\mu(u))(f(u)-\mu(u))^T}{v-2})\Omega^{-1}))}{|\Omega|^{(v+2n+1)/2}} d\Omega \\
&\propto \left(1 + \frac{(f(\boldsymbol{u}) - \mu(\boldsymbol{u}))^T K^{-1}(f(\boldsymbol{u}) - \mu(\boldsymbol{u}))}{v - 2}\right)^{-\frac{v+n}{2}}.
\end{aligned}
\tag{2.4.8}
$$

Except for a constant term that is independent of $\boldsymbol{u}$, (2.4.8) is same as (2.4.5). Thus, the GP in (2.4.6) can be expressed as a generalization of the multivariate

Student's-t distribution that is expressed in (2.4.9) as follows:

$$f(\boldsymbol{u}) \sim \mathcal{MVT}\left((f(\boldsymbol{u}); \mu(\boldsymbol{u}), v, K\right) \tag{2.4.9}$$

where

$$K = \begin{bmatrix} \kappa(u_1, u_1) & \dots & \kappa(u_1, u_n) \\ \vdots & & \vdots \\ \kappa(u_n, u_1) & \dots & \kappa(u_n, u_n) \end{bmatrix}$$

Here, in (2.4.9), the parameter v determines how heavy-tailed the process is. As $v \to \infty$, TP will converge to GP, implying that the GP is a special case of TP. Thus the use of TP in an ETT algorithm can capture more information relating to interior and contour points of the targets . This can easily lead to an improvement in the overall tracking performance. However, one of the drawbacks of the TP is that the Student's-t distribution is not closed under addition, which makes the TP less attractive for modeling noisy conditions — a critical aspect in tracking [55].

2.4.4   Student's-t Process Regression

In general, the TP concept predicts the unknown function values $\boldsymbol{f} \triangleq [f(u_1^{\boldsymbol{f}}), \dots,$ $f(u_{Nf}^{\boldsymbol{f}})]^T$ for a given set of inputs $\boldsymbol{u^f} \triangleq [u_1^{\boldsymbol{f}}, \dots, u_N^{\boldsymbol{f}}]^T$ and a set of measurements $\boldsymbol{y} \triangleq [y_1, \dots, y_N]^T$ with their corresponding inputs $\boldsymbol{u} \triangleq [u_1, \dots, u_N]^T$, where f is assumed to follow a zero-valued mean Student's-t distribution. Assume that the observations are corrupted by a Student's-t noise ϵ_k. i.e., the noisy process will be

$$y_k = f(u_k) + \epsilon_k \tag{2.4.10}$$

However, the same can be expressed as $y_k = f(u_k)$ if the noise is incorporated into the covariance function. This is a common practice when using regression algorithms, which effectively resolves the closure problem mentioned above. The direct solution to the TP regression for the latent function can be derived with the help of the following joint distribution of $\boldsymbol{f}$ and $\boldsymbol{y}$:

$$\begin{bmatrix} \boldsymbol{y} \\ \boldsymbol{f} \end{bmatrix} \sim \mathcal{MVT}(0, v, K). \tag{2.4.11}$$

where

$$K = \begin{bmatrix} K(\boldsymbol{u}, \boldsymbol{u}) + I_N \otimes R & K(\boldsymbol{u}, \boldsymbol{u^f}) \\ K(\boldsymbol{u^f}, \boldsymbol{u}) & K(\boldsymbol{u^f}, \boldsymbol{u^f}) \end{bmatrix}.$$

where I_N and R are identity matrix (with relevant dimensions), and power spectral density of the noise ϵ_k. From the joint distribution $p(\boldsymbol{f}, \boldsymbol{y})$, the moments of conditional distributions of $\boldsymbol{f}$ and $\boldsymbol{y}$, which are also Student's-t distributions, can be computed as follows:

$$(\boldsymbol{f}|\boldsymbol{y}) = \mathcal{MVT}(\boldsymbol{f}; \mathbb{K}\boldsymbol{y}, v + n, P), \tag{2.4.12a}$$

$$\mathbb{K} = K(\boldsymbol{u^f}, \boldsymbol{u})^T (K(\boldsymbol{u}, \boldsymbol{u}) + I_N \otimes R)^{-1}, \tag{2.4.12b}$$

$$P = \frac{(v-2) + \boldsymbol{y}^T (K(\boldsymbol{u}, \boldsymbol{u}) + I_N \otimes R)^{-1} \boldsymbol{y}}{v - 2 + n}$$

$$(K(\boldsymbol{u^f}, \boldsymbol{u})(K(\boldsymbol{u}, \boldsymbol{u}) + I_N \otimes R)^{-1} K(\boldsymbol{u}, \boldsymbol{u^f})). \tag{2.4.12c}$$

where $\otimes$ denote the Kronecker product. The computational complexity of the TP regression is $\mathcal{O}(n^3)$, where n is the number of observations.

2.4.5   Recursive Student's-t Process

Most of the regression algorithms, including GP and TP, assume that whole training data set is available at the time of processing. Although this assumption is perfectly suited for offline applications, applications like target tracking are often online, and they rely on sequentially arriving measurements, where these algorithms cannot be used directly. Recursive algorithms, which allow sequential training are, however, suitable for online processing. In [56], a recursive GP is presented using the Kalman filter as a state space model. As the core of the contribution of the current chapter relies on TP, having a similar recursive model is crucial. Although the literature is rich with a variety of TP algorithms, such as [47, 57, 58], including extensions for seeking better approximations [47] or for improved computational complexity [57, 58], all of these algorithms are designed to work offline, and hence unsuitable for online processing.

In order to derive a recursive regression method for TP, we reformulate the recursion as a state space model that can be updated by means of a Student's-t filter. For the regression model in (2.4.10), with the assumption of f and ϵ being independent, the following joint TP process can be formulated:

$$\begin{pmatrix} f_i \\ \epsilon_i \end{pmatrix} \sim \mathcal{TP}\left(\begin{pmatrix} \mu_i \\ 0 \end{pmatrix}, v, \begin{pmatrix} \kappa_i & 0 \\ 0 & \kappa_\epsilon \end{pmatrix} \right). \tag{2.4.13}$$

As f is modeled as a TP, the initial distribution $p_0(f)$ is

$$p_0(f) = \mathcal{MVT}(f; \mu_0^f, v_0, C_0^f) \tag{2.4.14}$$

24

where v, $\mu_0^f \triangleq m(u)$ and $C_0^f \triangleq \kappa(u, u)$ represent degrees of freedom, mean, and the kernel function, respectively. For the purpose of deriving a recursive formulation, assume the following squared exponential as the kernel function:

$$\kappa(u, u') = \alpha^2 . \exp\left(-\frac{1}{2}(u - u')^T \Sigma^{-1}(u - u')\right). \tag{2.4.15}$$

where, Σ represents the characteristic length-scale of the process, which determines the length of the wiggles in function f and α^2 denotes the prior output variance, which determines the average distance of the function f from the mean μ.

The overall objective, particularly in the context of online application, is to derive the posterior distribution $p(f|\boldsymbol{y}_{1:k})$ by updating the prior distribution of f from time $k-1$ with $\boldsymbol{y}_{1:k} \equiv (\boldsymbol{y}_1, ..., \boldsymbol{y}_k)$. On this note, it can be noticed that the prior (and hence the posterior) distributions include a vector of hyper-parameters, for instance, $\eta = [\sigma, \alpha, v]^T$, which may need to be accounted when updating the posterior distribution, which makes the whole approach intractable. However, this concern can be overcome by assuming the hyper-parameter vector $\eta = [\sigma, \alpha, v]^T$ as a known prior, which essentially eliminates the need for learning it online. This assumption is acceptable for ETT problems [11], as the main priority lies in estimating the kinematic states of the targets. Although, this issue can be overcome by using the sigma-point method when using TP regression [56], we do not address this issue here, and thus assume that the hyper-parameter vector is a known prior. With this assumption, the posterior distribution $p(f|y_{1:k})$ can be expressed by the following recursive formulation

$$p(\boldsymbol{f}|y_{1:k}) \propto \underbrace{p(y_k|\boldsymbol{f}, y_{1:k-1})}_{\text{likelihood}} \underbrace{p(\boldsymbol{f}|y_{1:k-1})}_{\text{prior}}. \tag{2.4.16}$$

Given the Markovian property, (i.e., current measurement is independent of past measurements $y_{1:k-1}$), the likelihood term can be approximated as $p(y_k|\boldsymbol{f})$, i.e.,

$$p(y_k|\boldsymbol{f}, y_{1:k-1}) \sim p(y_k|\boldsymbol{f})$$

This approximation will be exact if the prior measurements were included in the input value for $\boldsymbol{f}$. However, if the input values $y_{1:k-1}$ are to remain close to the characteristic length-scale of the kernel function [11], this approximation will be acceptable. One method for ensuring that the input values remain close to the function $\mathbf{f}$, is to utilize a well-defined, yet small, number of basis angles, when modeling the target shape using TP.

Now, as per (2.4.11), the measurement y_k and the model $\boldsymbol{f}$ are jointly Student's-t distributed. Thus,

$$\begin{bmatrix} y_k \\ \boldsymbol{f} \end{bmatrix} \sim \mathcal{MVT}\left(0, v, \begin{bmatrix} \kappa(u_k, u_k) + R & K(u_k, \boldsymbol{u^f}) \\ K(\boldsymbol{u^f}, u_k) & K(\boldsymbol{u^f}, \boldsymbol{u^f}) \end{bmatrix}\right) \tag{2.4.17}$$

Using (2.4.17) in (2.4.16), assuming (2.4.14) holds true, one will obtain

$$p(y_k|\boldsymbol{f}) = \mathcal{MVT}(y_k; G_t^s \boldsymbol{f}, v + n, R_k^s), \tag{2.4.18a}$$

where

$$G_t^s \triangleq K(u_k, \boldsymbol{u^f})(K(\boldsymbol{u^f}, \boldsymbol{u^f}))^{-1}, \tag{2.4.18b}$$

$$R_t^s = \frac{(v-2)}{(v-2)+n}B + \frac{\Delta}{(v-2)+n}B, \tag{2.4.18c}$$

$$\Delta \triangleq (\boldsymbol{f})^T(K(\boldsymbol{u^f}, \boldsymbol{u^f}))^{-1}(\boldsymbol{f}), \tag{2.4.18d}$$

$$C_0^s = K(\boldsymbol{u^f}, \boldsymbol{u^f}). \tag{2.4.18e}$$

where B is defined as,

$$B = \left(\kappa(u_k, u_k) + R - K(u_k, \boldsymbol{u^f})(K(\boldsymbol{u^f}, \boldsymbol{u^f}))^{-1}K(\boldsymbol{u^f}, u_k) \right)$$

With the possibility of expressing both the likelihood and prior terms using multivariate Student's-t distribution, a recursive filter, based on the state space model, can now be formulated. However, Kalman filter or its non-linear extensions cannot be used as state space model here owing to the fact that they are minimum mean square error (MMSE) estimators intended for transition models corrupted by the Gaussian noise. If used, the heavy-tailed non-Gaussian noise and outliers can simply add a notable bias leading to a sub-optimal performance. Instead, one can use the Student's-t filter (STF) [59], which offers a route for estimating the posterior probability using Student's-t distribution, particularly where the process and measurement noise are heavy-tailed non-Gaussian.

Consider a linear system with the following state space model

$$f_{k-1}(\mathbf{x}_{k-1}) = F_{k-1}\mathbf{x}_{k-1} + V_k \tag{2.4.19}$$

where $V_k \sim \mathcal{MVT}(\mathbf{0}, v, Q_k)$ is a heavy-tailed process noise and F_{k-1} is the state dynamic model. Also assume that the initial state vector $\mathbf{x}_0$ follows $\mathbf{x}_0 \sim \mathcal{MVT}(\hat{\mathbf{x}}_{0|0}, v, P_{0|0})$, and a corresponding measurement space

$$h_k(\mathbf{x}_k) = H_k\mathbf{x}_k + W_k \tag{2.4.20}$$

where $W_k \sim \mathcal{MVT}(\mathbf{0}, v, R_k)$ is a heavy-tailed measurement noise and H_k is the measurement matrix model. In order to use the STF filter in conjunction with the proposed recursive TP regression algorithm, the state-, and the measurement-updates have to be derived for the linear system defined in (2.4.19)and (2.4.20), respectively. These are covered by lemmas L1 and L2 below. The lemma L1 is derived using the Chapman-Kolmogorov and affine transformation of Student's-t random variables, while L2 is derived by exploiting the Bayes theorem [59].

Lemma 1 The prediction step for the state space model is

$$\hat{\mathbf{x}}_{k|k-1} = F_{k-1}\hat{\mathbf{x}}_{k-1|k-1}, \tag{2.4.21a}$$

$$P_{k|k-1} = F_{k-1}P_{k-1|k-1}F_{k-1} + Q_{k-1}. \tag{2.4.21b}$$

Lemma 2 Using Student's-t distribution, the posterior can be updated as follows:

$$p(\mathbf{x}_k|\mathbf{z}_k) = \mathcal{MVT}(\hat{\mathbf{x}}_{k|k}, v, P_{k|k}). \tag{2.4.22}$$

where

$$v' = v + n_z, \tag{2.4.23a}$$

$$\hat{\mathbf{x}}_{k|k} = \hat{\mathbf{x}}_{k|k-1} + K_k(\mathbf{z}_k - \hat{\mathbf{z}}_{k|k-1}), \tag{2.4.23b}$$

$$K_k = P_{k|k-1}H_k^T(H_k P_{k|k-1}H_k^T + R_k)^{-1}, \tag{2.4.23c}$$

$$d_k = (\mathbf{z}_k - \hat{\mathbf{z}}_{k|k-1})^T \underbrace{(H_k P_{k|k-1}H_k^T + R_k)}_{S}^{-1}$$

$$(\mathbf{z}_k - \hat{\mathbf{z}}_{k|k-1}), \tag{2.4.23d}$$

$$P'_{k|k} = \frac{v + d_k}{v + n_z}(I - K_k H_k)P_{k|k-1}, \tag{2.4.23e}$$

$$\hat{\mathbf{z}}_{k|k-1} = H_k \hat{\mathbf{x}}_{k|k-1}. \tag{2.4.23f}$$

Although these developments enable the use of the STF, the presence of a state-dependent measurement noise R_k^s in (2.4.18) will add a conditional bias to the final estimation, which is highly undesirable. We will be addressing this by considering the dependency in the conventional STF context, and by deriving a new filter, namely, the generalized STF (GSTF), which is similar to the one introduced in [60] for an additive state-dependent measurement noise Kalman filter.

Before formulating an expression for GSTF, we separate the state component R_t^s into two parts: state-dependent component $R^{s,D}$, and state-independent component

$R^{s,I}$. With this,

$$R_k^{s,I} \triangleq \frac{(v-2)}{(v-2)+n}\big(\kappa(u_k,u_k)+R-K(u_k,\boldsymbol{u^f})$$

$$(K(\boldsymbol{u^f},\boldsymbol{u^f}))^{-1}K(\boldsymbol{u^f},u_k)\big) \tag{2.4.24}$$

$$R_k^{s,D} \triangleq \frac{1}{(v-2)+n}\big(\kappa(u_k,u_k)(K(\boldsymbol{u^f},\boldsymbol{u^f}))^{-1}+$$

$$R(K(\boldsymbol{u^f},\boldsymbol{u^f}))^{-1}-K(u_k,\boldsymbol{u^f})(K(\boldsymbol{u^f},\boldsymbol{u^f}))^{-2}K(\boldsymbol{u^f},u_k)\big),$$

$$\tag{2.4.25}$$

To facilitate the derivation, the structure of a measurement equation with dependent noise v, defined by $y = Hx + J(x)v$ can be changed to have an independent noise v^L, where L denotes linear, with zero-mean noise with covariance $R^L = J(x)RJ(x)^T$. This can be achieved by replacing v by two additive terms e_k^I and e_k^D, as follows [61, 62] :

$$\begin{aligned} y_k &= G^s\boldsymbol{f} + \boldsymbol{f}e_k^D + e_k^I \\ &= G^s\boldsymbol{f} + e_k' \end{aligned} \tag{2.4.26}$$

where

$$\begin{aligned} e_k^I &\sim \mathcal{MVT}(0,v,R_k^{s,I}), \\ e_k^D &\sim \mathcal{MVT}(0,v,R_k^{s,D}), \\ e_k' &\sim \mathcal{MVT}(0,v,R_k'). \end{aligned}$$

and

$$R'_k = \mathbf{Cov}\{e'_k, e'_k\} = R_k^{s,D} M_k + R_k^{s,I}, \qquad (2.4.27\text{a})$$

$$M_k = \mathbf{diag}\{\boldsymbol{f} P_{k|k-1} \boldsymbol{f}^T\}. \qquad (2.4.27\text{b})$$

This new measurement covariance leads to the same update equation in conventional STF in Lemma 2, with the only difference being the replacement of R_k by R'_k.

2.5   Problem Formulation

In the context of extended target tracking, the majority of the existing algorithms rely on scattering points at the contour of the target. In this chapter, a generalized version of the solution is provided accounting scattering points both from the interior surface and contour of the targets, addressing the shortcomings of the GP-based ETT solutions. We achieve this by replacing the GP by TP. In this section, we develop TP-based augmented target state and measurement models, focusing on the two-dimensional ETT case. Although we have not explicitly covered the three-dimensional extension of this work, an effort for that extension is trivial. Prior to developing an extended target and measurement model, we illustrate the basis of our target and coordinate space in Figure 2.1.
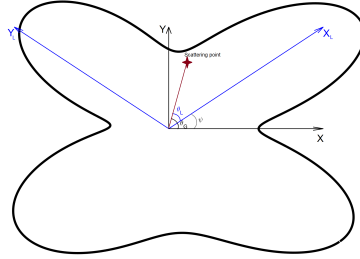
Figure 2.1: Illustration of target extent and measurements. Here, each measurement is referred with respect to a global and local coordinate spaces (X, Y), and (X^L, Y^L), and corresponding angles θ and θ^L.

2.5.1   Extended Target Model

To derive the extended target model in the context of TP, consider the following state space system:

$$\mathcal{X}_k = \mathcal{F}_k \mathcal{X}_{k-1} + \mathcal{V}_{k-1}, \tag{2.5.1}$$

where $\mathcal{F}_k = \mathbf{diag}[F_k, F_k^s]$ is the state transition matrix with F_k and F_k^s representing the dynamic behaviour of target center and extent, respectively, $\mathcal{X}_{k-1} = [(\mathbf{x}_{k-1})^T, (\mathbf{x}_{k-1}^s)^T]$ is the target state consisting of two parts $\mathbf{x}_{k-1}$ and $\mathbf{x}_{k-1}^s$. The process noise $\mathcal{V}_{k-1}$, as outlined in Section 2.4, is a combination of two independent Student's-t distributions, and can be expressed as

$$\mathcal{V}_{k-1} \sim \mathcal{MVT}(0, v_{k-1}, \mathbf{diag}[T_{k-1}, T_{k-1}^s]). \tag{2.5.2}$$

where T_{k-1} and T_{k-1}^s are covariance matrices of process noise for kinematic and extent state, respectively. Furthermore, $\mathbf{x}_{k-1}$ represents the kinematic state vector, i.e., the

kinematic attributes of the extended target center, and $\mathbf{x}_{k-1}^s$ represents the extended target extent state. These can be expressed as follows:

$$\mathbf{x}_{k-1} = [x_k, y_k, \dot{x}_k, \dot{y}_k, \psi_k, \dot{\psi}_k]^T, \tag{2.5.3}$$

and

$$\mathbf{x}_{k-1}^s = [f_k(\theta_1), \ldots, f_k(\theta_n)]^T. \tag{2.5.4}$$

where $f_k(\theta)$ is the radius function represented as a TP, modeled by

$$f_k(\theta) \sim \mathcal{TP}(\mu(\theta), v, \kappa(\theta, \theta')). \tag{2.5.5}$$

Also, the term $\mathbf{x}^{center}$ used in the following section is defined according to

$$\mathbf{x}^{center} = [x_k, y_k]^T. \tag{2.5.6}$$

2.5.2   Measurement Model

The recursive state space TP regression model introduced in 2.4.5 enables the augmentation of the target kinematic state with the target contour information, and recursive estimation of the state information. As such, the TP regression model can be used for tracking an extended target. More specifically, when using TP in an ETT application, the inputs are angles expressed by a vector $\boldsymbol{\Theta} = [\theta_1, \ldots, \theta_i, \ldots]$ such that $\theta_i \in [0, 2\pi]$, and corresponding outputs are the radius of the target contour for each θ_i. From (2.4.10), the measurement y_k and the function f are joint Student's-t,

$$\begin{bmatrix} y_k \\ \boldsymbol{f} \end{bmatrix} \sim \mathcal{MVT}(0, v, K), \tag{2.5.7}$$

where

$$K = \begin{bmatrix} \kappa(\theta_k, \theta_k) + R & K(\theta_k, \Theta) \\ K(\Theta, \theta_k) & K(\Theta, \Theta) \end{bmatrix}$$

The relevant prior in (2.4.14) and the conditional distribution $p(y_k|\mathbf{f})$ resulting from the joint Student's-t distribution $p(\mathbf{f}, y)$ can be computed as

$$p(\boldsymbol{f}|y) = \mathcal{MVT}(y_k; G_k^{s,j}\boldsymbol{f}, v, R_k^{s,j}), \tag{2.5.8}$$

$$p(f) = \mathcal{MVT}(\boldsymbol{f}; 0, v, P_0^s) \tag{2.5.9}$$

where $\boldsymbol{f} = \mathbf{x}_k^s = [f_k(\theta_1), \dots, f(\theta_n)]^T$, and

$$G_k^{s,j} \triangleq G_k^{s,j}(\theta_k^{j,Local}) = K(\theta_k^{j,Local}, \Theta)K(\Theta, \Theta)^{-1} \tag{2.5.10a}$$

$$R_k^{s,j} \triangleq R_k^{s,j}(\theta_k^{j,Local}) = \frac{(v-2) + \Delta}{(v-2) + n}\Big(\kappa(\theta_k^{j,Local}, \theta_k^{j,Local}) +$$

$$R - K(\theta_k^{j,Local}, \Theta).K(\Theta, \Theta)^{-1}.K(\Theta, \theta_k^{j,Local})\Big) \tag{2.5.10b}$$

$$\Delta = (\mathbf{x}_k^s)^T K(\Theta, \Theta)^{-1}(\mathbf{x}_k^s) \tag{2.5.10c}$$

$$P_0^s = K(\Theta, \Theta). \tag{2.5.10d}$$

where $K(\Phi, \Xi)$ is defined over input vectors Φ and Ξ such that

$$K(\Phi, \Xi) \triangleq \begin{bmatrix} \kappa(\Phi, \Xi) & \dots & \kappa(\Phi, \Xi) \\ \vdots & & \vdots \\ \kappa(\Phi, \Xi) & \dots & \kappa(\Phi, \Xi) \end{bmatrix}. \qquad (2.5.11)$$

with the definition of κ being the modified SE kernel, which will be used as the covariance function [11], and defined as,

$$\kappa(\theta, \theta') = \sigma_f^2 \exp(-\frac{2\sin^2(\theta - \theta')/2}{l^2}) + \sigma_r^2. \qquad (2.5.12)$$

From (2.4.27a), the state dependent noise $R_k^{s,j}$ is now replaced by a modified noise term $R_k'^{s,j}$ to conform with the GSTF formulation. Having the likelihood and prior both in Student's-t distribution form, allows one to use the STF filter on the state space model for estimating target contours. Thus,

$$\mathbf{x}_{k+1}^s = \mathbf{x}_k^s, \qquad (2.5.13)$$

$$y_k = G^{s,j}(\theta_k)\mathbf{x}_k^s + e_k'^{s,j}, \qquad (2.5.14)$$

$$\mathbf{x}_0^s \sim \mathcal{MVT}(\mathbf{x}_0^s; 0, v, P_0^s). \qquad (2.5.15)$$

where

$$e_k'^{s,j} \sim \mathcal{MVT}(0, v, R_k'^{s,j}(\mathbf{x}_k^s)),$$

and

$$\mathbf{x}_k^s = [f(\theta_1), \ldots, f(\theta_{N^s})]^T.$$

To classify the measurements originating from the target, which are variable, and may originate either from interior or contour points of the target, a parameter $s_k^j \in [0, 1]$ is defined, with the definition of $s_k^j = 1$ representing the measurements from the target contour and $s_k^j \neq 1$ representing interior measurements. With this, each measurement can be expressed as a summation of the target center state, x_k^{center}, radial function $f_k(\theta_k^{j,Local})$ associated with angle θ, and measurement noise w_k^j, as follows:

$$\mathbf{z}_k^j = \mathbf{x}_k^{center} + s_k^j \mathbf{o}_k^j(\mathbf{x}_k^{center}) f_k(\theta_k^{j,Local}) + \mathbf{w}_k^j. \qquad (2.5.16)$$

where w_k^j follows a Student's-t distribution $w_k^j \sim \mathcal{MVT}(0, v_2, R)$, and $\mathbf{o}_k^j(\mathbf{x}_k^{center})$ is the orientation vector, which can be computed using

$$
\begin{aligned}
\mathbf{o}_k^j(\mathbf{x}_k^{center}) &= \frac{\mathbf{z}_k^j - \mathbf{x}_k^{center}}{||\mathbf{z}_k^j - \mathbf{x}_k^{center}||_2} \\
&= \left[\cos(\theta_k^{j,G}), \sin(\theta_k^{j,G})\right].
\end{aligned}
\qquad (2.5.17)
$$

and,

$$\theta_k^{j,L} = \theta_k^{j,G} - \psi_k. \qquad (2.5.18)$$

In a Bayesian framework-driven algorithm, the measurement model is used to generate the predicted measurement and innovation covariance matrix. However,

the measurement model in (2.5.16) is not accurate. However, replacing the radial function with its TP model outlined in (2.5.14) can circumvent this issue. In other words, by replacing the TP model of contour in (2.5.16), a finalized form of the TP-based measurement model can be derived as

$$\mathbf{z}_k^j = \mathbf{x}_k^{center} + s_k^j \mathbf{o}_k^j G_k^{s,j} \mathbf{x}_k^s + s_k^j \mathbf{o}_k^j e_k^{\prime s,j} + \mathbf{w}_k^j \tag{2.5.19}$$

In [10], with the assumption that the scattering points are uniformly distributed over the star-convex region of ET object, it was proved that the scaling factor satisfies $s_k^{j\,2} \sim \mathcal{U}(0,1)$. The mean and variance of the s_k^j was computed analytically in [11] and is equal to $\mu_s = \frac{2}{3}$ and $\sigma_s^2 = \frac{1}{18}$, respectively. Thus, the distribution is approximated by following the Student's-t distribution

$$s_k^j \sim \mathcal{MVT}(\mu_s, v, \frac{v-2}{v}\sigma_s^2).$$

Let

$$s_k^j \mathbf{o}_k^j G_k^{s,j} \mathbf{x}_k^s = \mu_s^j \mathbf{o}_k^j G_k^{s,j} \mathbf{x}_k^s + (s_k^j - \mu_s) \mathbf{o}_k^j G_k^{s,j} \mathbf{x}_k^s, \tag{2.5.20}$$

and

$$\hat{\mathbf{w}}_k^j = (s_k^j - \mu_s) \mathbf{o}_k^j G_k^{s,j} \mathbf{x}_k^s + s_k^j \mathbf{o}_k^j e_k^{\prime s,j} + w_k^j. \tag{2.5.21}$$

Using (2.5.20) and (2.5.21) in (2.5.19) results in

$$\mathbf{z}_k^j = \underbrace{\mathbf{x}_k^{center} + \mu_s \mathbf{o}_k^j G_k^{s,j} \mathbf{x}_k^s}_{\mathbf{h}_k^j(\mathcal{X}_k)} + \hat{\mathbf{w}}_k^j. \tag{2.5.22}$$

37

The first moment of the derived Student's-t noise $\hat{w}_k^j$ can be computed based on the assumption of independence between the scaling parameter s_k^j and $e_k'^{s,j}$ by $E[\hat{w}_k^j] = 0$. The second moment of term $\hat{w}_k^j$ can be computed simply by using the properties of the Student's-t distribution, as shown in Appendix 2.12.1:

$$
\begin{aligned}
\mathbf{Var}[\hat{w}_k^j] &= \mathbf{Var}\left[(s_k^j - \mu_s)\mathbf{o}_k^j G_k'^{s,j}\mathbf{x}_k^s + s_k^j \mathbf{o}_k^j e_k'^{s,j} + w_k^j\right] \\
&= \left(\mu_s^2 + \left(\frac{v-2}{v}\sigma_s\right)^2\right)\left[\mathbf{o}_k^j\left(\frac{v-2}{v}R_k'^{s,j}(\mathbf{x}_k^s)\right)(O_k^j)^T\right] \\
&\quad + \left(\frac{v-2}{v}\sigma_s\right)^2\left[(\mathbf{o}_k^j G_k'^{s,j}\mathbf{x}_k^s)(\mathbf{o}_k^j G_k'^{s,j}\mathbf{x}_k^s)^T\right] \\
&\quad + \mu_s^2 \mathbf{o}_k^j G_k'^{s,j}(\mathbf{o}_k^j)^T(\nabla_x R_k'^{s,j})P_k^s + \frac{v-2}{v}R.
\end{aligned}
\tag{2.5.23}
$$

Here, note that the degrees of freedom of noise is constant under this transformation. If one would like to consider only the measurements that are generated from the target contour, the terms μ_s, and σ_s may need to be updated accordingly, i.e., by setting $\mu_s = 1$ and $\sigma_s = 0$.

2.6 TP-EKF Filter with State-Dependent Noise Observation

In this section, a new filter for simultaneously estimating the target kinematic and extent state is proposed. The proposed TP-EKF filter is an extension to the traditional EKF method, and is capable of tracking extended targets with multiple unstable and unknown scattering points. However, an augmented measurement model, where

all measurements within one scan are accounted, is essential to recursively update the posterior, if TP is to be under in conjunction with EKF. Consider the following augmented models for measurements,

$$\mathbf{z}_k = [\mathbf{z}_{k,1}^T, \ldots, \mathbf{z}_{k,n_k}^T]^T \tag{2.6.1a}$$

$$R_k = \mathrm{diag}[R_{k,1}, \ldots, R_{k,n_k}]^T \tag{2.6.1b}$$

$$\mathbf{h}_k(\mathcal{X}_k) = [\mathbf{h}_k^1(\mathcal{X}_k), \ldots, \mathbf{h}_k^{n_k}(\mathcal{X}_k)]^T. \tag{2.6.1c}$$

and corresponding state and measurement models,

$$\mathcal{X}_{k+1} = \mathcal{F}_k \mathcal{X}_k + \mathbf{v}_k \tag{2.6.2a}$$

$$\mathbf{z}_k = \mathbf{h}_k(\mathcal{X}_k) + \mathbf{w}_k \tag{2.6.2b}$$

$$\mathcal{X}_0 \sim \mathcal{MVT}(\mu_0, v_0, P_0). \tag{2.6.2c}$$

where $\mathbf{v}_k \sim \mathcal{MVT}(0, v, Q_k)$ and $\mathbf{w}_k \sim \mathcal{MVT}(0, v, R_k)$ are multivariate Student's-t distributions. Using the derived state and measurement models in (2.6.2a) and (2.6.2b), one can use the STF update procedure described in Lemma 2, for estimating the augmented state. The partial derivatives of the relevant measurement equation are shown in Appendix 2.12.2, since the recursion in Lemma 2 needs the $H = \frac{d\mathbf{h}_k(\mathcal{X}_k)}{d(\mathcal{X}_k)}$.

2.7 Approximations for TP-EKF

As discussed in previous sections, the core contribution of this manuscript relies on Student's-t distribution. However, a Student's-t distribution can become a Gaussian distribution when the underlying degrees of freedom v becomes large, i.e. when $v \to \infty$. This is a particular concern in our case, especially when $k \to \infty$, the degrees of freedom v_k, outlined in (2.4.23a) in Section 2.4, becomes very large, i.e. infinity. With the underlying Student's-t distribution becoming a Gaussian distribution, all the benefits of the TP-EKF will dissipate. From [37, 63], the heavy-tailed distribution of the posterior density can be preserved as,

$$\mathcal{MVT}(\mathcal{X}; \hat{\mathcal{X}}, v_k, P_k) \approx \mathcal{MVT}(\mathcal{X}; \hat{\mathcal{X}}, \bar{v}_k, \tau P_k), \qquad (2.7.1)$$

where $\bar{v}_k$ is a user-defined, application-sensitive degrees of freedom, and τ is the perspective parameter computed by using Kullback-Leibler [64] or other moment matching methods [59], as follows:

$$\tau \triangleq \frac{v_k(\bar{v}_k - 2)}{(v_k - 2)\bar{v}_k}. \qquad (2.7.2)$$

Here, the computation of τ in (2.7.2) follows [65]. We define Lemma 3, for rendering a more generic TP-EKF algorithm.

Lemma 3 The proposed TP-EKF algorithm assumes similar degrees of freedom for process noise, measurement noise, and initial state vector. Although, this was helpful

in the derivation of the final algorithm, in reality, it is seldom that they have similar values. Consider a realistic process noise, measurement noise, and initial state vector with non-equal degrees of freedom, defined by

$$\mathbf{v}_k \sim \mathcal{MVT}(\mathbf{0}, v_1, Q_k) \tag{2.7.3}$$

$$\mathbf{w}_k \sim \mathcal{MVT}(\mathbf{0}, v_2, R_k) \tag{2.7.4}$$

$$\mathbf{x}_0 \sim \mathcal{MVT}(\hat{\mathbf{x}}_{0|0}, v_3, P_{0|0}) \tag{2.7.5}$$

The original TP-EKF algorithm can be utilized by the following approximations:

$$\mathbf{v}_k \sim \mathcal{MVT}(\mathbf{0}, v, \tilde{Q}_k), \tag{2.7.6a}$$

$$\tilde{Q}_k \triangleq c_Q Q_k. \tag{2.7.6b}$$

$$\mathbf{w}_k \sim \mathcal{MVT}(\mathbf{0}, v, \tilde{R}_k), \tag{2.7.7a}$$

$$\tilde{R}_k \triangleq c_R R_k. \tag{2.7.7b}$$

and

$$\mathbf{x}_0 \sim \mathcal{MVT}(\hat{\mathbf{x}}_{0|0}, v, \tilde{P}_{0|0}), \tag{2.7.8a}$$

$$\tilde{P}_{0|0} \triangleq c_P P_{0|0}. \tag{2.7.8b}$$

Here, c_P, c_Q, and c_R are constants, which can be computed using the same moment matching method discussed above. With this approximation, the proposed filter becomes applicable to real-world scenarios with an unequal degree of freedom among measurement noise, process noise, and prior Student's-t distribution.

2.8   TP-EKF Gating

In formulating a generic TP-based ETT algorithm, we have been gradually relaxing the constraints laid out when the original algorithm was derived. Along this line, the proposed algorithm assumes a clutter-free environment with perfect detections. However, in a problem that inherently deals with multiple targets and measurement origin uncertainty, this assumption is unrealistic. One simple yet effective method for handling the measurement origin uncertainty caused by clutter and missed detections is, data association. The extension of our work to the general multitarget tracking problem using the Random Finite Sets (RFS) [66] and Probabilistic Data Association (PDA) [67] frameworks is the topic of a forthcoming work. The most commonly used method for data association is the tracking gate, by which valid measurements are distinguished from invalid ones, and passed on to the subsequent processes. Although, rectangular and ellipsoidal gating are the most commonly used [68] algorithms, the latter accounts for the distribution of target measurements, and hence more appropriate for our case, particularly when used incorporating the Mahalanobis distance. Traditional gating approaches consider Gaussian noise, and the Mahalanobis distances becomes Chi-square distributed. In the context of measurements with Student's-t distribution, the Mahalanobis distance D_k for a measurement $\mathbf{z}_k$, $p(\mathbf{z}_k) = \mathcal{MVT}(\mathbf{z}_k; \hat{\mathbf{z}}_k, v_k, S_k)$, follows an F distribution [59]. Thus,

$$\frac{1}{n_z} D_k(\mathbf{z}) \sim f(\mathbf{z}; d_1, d_2)$$

$$= \frac{1}{\boldsymbol{B}(d_1/2, d_2/2)} \left(\frac{d_1}{d_2}\right)^{\frac{d_1}{2}} \mathbf{z}^{\frac{d_1}{2}-1} \left(1 + \frac{d_!}{d_2}\mathbf{z}\right)^{-\frac{d_1+d_2}{2}} \tag{2.8.1}$$

for $d_1, d_2 > 0$, and $\boldsymbol{B}(a,b) = \frac{\Gamma(a)\Gamma(b)}{\Gamma(a+b)}$ denotes the Beta function. With this, the Mahalanobis distance for the proposed TP-EKF becomes,

$$D_k(\mathbf{z}_k) = (\mathbf{z}_k - H\hat{\mathcal{X}}_{k+1|k})^T S_{k+1}^{-1} (\mathbf{z}_k - H\hat{\mathcal{X}}_{k+1|k}) \tag{2.8.2}$$

where H and S are the same as in (2.4.23c) and (2.4.23d), respectively. Then, the measurement $\mathbf{z}_k$ will be within the gating region

$$\mathcal{V}(k, Th_g) = \{\mathbf{z}_k : D^2 \leq Th_g\} \tag{2.8.3}$$

with the corresponding probability defined by the gating threshold Th_g. The gating threshold can be obtained from the inverse cumulative distribution function of $f(n_z, v_z)$ at a desired level of significance α. Typical values for α are usually $0.95 \leq \alpha \leq 0.99$. Lowering the value of α implies that $(1 - \alpha)$ of the true measurements are rejected, and thus lower gating performance.

2.9 Conditional Cramér-Rao Lower Bound for TP-EKF

The posterior Cramér-Rao lower bound (PCRLB) [69] provides a performance bound on the mean square error (MSE) general nonlinear filtering problems. The PCRLB is defined as the inverse of the posterior Fisher information matrix (PFIM), where the Fisher information matrix is derived using the expected value of the observed random variables, namely the measurements and the system states. This formulation, and hence the conventional notion of PCRLB, relies on sequential updates of the measurement and state models, and is, hence bound to be an offline method. However, the updated covariance matrix of the proposed EKF filter is partially dependent on the actual and underlying system dynamics. This presents a circular dependency problem, where the covariance matrix cannot be computed offline, and thus, the conventional PCRLB, which is offline bound, cannot be used to evaluate the performance of the proposed EKF filter.

There are a number of techniques outlined in the literature to circumvent this problem. For instance, in [70], a time-varying, observation-dependent lower bound on the performance of a variational Bayes (VB) estimator is presented to handle non-Gaussian measurement noise and well-behaved process noise. In [71], a concept of conditional PCRLB that is dependent on the actual measurement up-to the current time is presented, which is generic enough to be extended for our case. More specifically, we will use the recursive formula derived in [71] to compute the conditional PCRLB for the proposed filter with a Student's-t based noise.

To begin with, the conditional mean square error (MSE) is defined as

$$MSE(\hat{X}_{0:k+1}|Z_k) \triangleq$$

$$E\left[(\hat{\mathcal{X}}_{0:k+1} - \mathcal{X}_{0:k+1})(\hat{\mathcal{X}}_{0:k+1} - \mathcal{X}_{0:k+1})^T|Z_{1:k}\right]$$

$$= \int (\hat{\mathcal{X}}_{0:k+1} - \mathcal{X}_{0:k+1})(\hat{\mathcal{X}}_{0:k+1} - \mathcal{X}_{0:k+1})^T p_{k+1}^c dZ_{k+1},$$

$$(2.9.1)$$

where $p_{k+1}^c \triangleq p(\mathcal{X}_{0:k+1}, Z_{k+1}|Z_{1:k})$. The conditional Fisher information matrix, denoted by $I(\mathcal{X}_{0:k+1}, Z_{k+1}|Z_{1:k})$, is defined as

$$I(\mathcal{X}_{0:k+1}|Z_{1:k}) \triangleq E\left[-\Delta_{\mathcal{X}_{0:k+1}}^{\mathcal{X}_{0:k+1}} \log p_{k+1}^c|Z_{1:k}\right]$$

$$= -\int \left[-\Delta_{\mathcal{X}_{0:k+1}}^{\mathcal{X}_{0:k+1}} \log p_{k+1}^c|Z_{1:k}\right] p_{k+1}^c d\mathcal{X}_{0:k+1} dZ_{k+1}.$$

$$(2.9.2)$$

Furthermore, following [71, 72], the MSE of any estimator cannot go below the inverse of the conditional Fisher information matrix. Thus,

$$E\left[(\hat{\mathcal{X}}_{0:k+1} - \mathcal{X}_{0:k+1})(\hat{\mathcal{X}}_{0:k+1} - \mathcal{X}_{0:k+1})^T|Z_{1:k}\right] \geq$$

$$I^{-1}(\mathcal{X}_{0:k+1}|Z_{1:k}).$$

$$(2.9.3)$$

The direct method for computing $I^{-1}(\mathcal{X}_{0:k+1}|Z_{1:k})$ in (2.9.2) involves dealing with large matrices at every time step k. Instead, we resort to computationally efficient

techniques outlined in [69, 71], where the conditional FIM, $L_A(\mathcal{X}_{k+1}|Z_{1:k})$, and thus the conditional PCRLB, are computed recursively. Thus,

$$L_A(\mathcal{X}_{k+1}|Z_{1:k}) = B_k^{22} + B_k^{21}(L_A(\mathcal{X}_k|Z_{1:k}) + B_k^{11})^{-1}B_k^{12}, \tag{2.9.4a}$$

where

$$\Delta_{\mathcal{X}_k}^{\mathcal{X}_k} \triangleq \nabla_{\mathcal{X}_k}\nabla_{\mathcal{X}_k} \tag{2.9.4b}$$

$$L_A(\mathcal{X}_k|Z_{1:k}) = N_k^{22} - N_k^{21}[N_k^{11} + L_A(\mathcal{X}_{k-1}|Z_{1:k-1})]^{-1}N_k^{12} \tag{2.9.4c}$$

$$B_k^{11} = E_{p_{k+1}^c}\{-\Delta_{\mathcal{X}_k}^{\mathcal{X}_k}\log p(\mathcal{X}_{k+1}|\mathcal{X}_k)\} \tag{2.9.4d}$$

$$B_k^{12} = [B_k^{21}]^T = E_{p_{k+1}^c}\{-\Delta_{\mathcal{X}_k}^{\mathcal{X}_{k+1}}\log p(\mathcal{X}_{k+1}|\mathcal{X}_k)\} \tag{2.9.4e}$$

$$B_k^{22} = E_{p_{k+1}^c}\{-\Delta_{\mathcal{X}_{k+1}}^{\mathcal{X}_{k+1}}\log p(\mathcal{X}_{k+1}|\mathcal{X}_k)\}+$$

$$E\{-\Delta_{\mathcal{X}_{k+1}}^{\mathcal{X}_{k+1}}\log p(z_{k+1}|\mathcal{X}_{k+1})\} \tag{2.9.4f}$$

$$N_k^{11} = E_{p(\mathcal{X}_{0:k}|Z_{1:k})}\{-\Delta_{\mathcal{X}_{k-1}}^{\mathcal{X}_{k-1}}\log p(\mathcal{X}_k|\mathcal{X}_{k-1})\} \tag{2.9.4g}$$

$$N_k^{12} = (N_k^{21})^T = E_{p(\mathcal{X}_{0:k}|Z_{1:k})}\{-\Delta_{\mathcal{X}_{k-1}}^{\mathcal{X}_k}\log p(\mathcal{X}_k|\mathcal{X}_{k-1})\}$$

$$\tag{2.9.4h}$$

$$N_k^{22} = E_{p(\mathcal{X}_{0:k}|Z_{1:k})}\{-\Delta_{\mathcal{X}_k}^{\mathcal{X}_k}[\log p(\mathcal{X}_k|\mathcal{X}_{k-1}) + \log p(z_k|\mathcal{X}_k)]\} \tag{2.9.4i}$$

The partial derivatives used in (2.9.4b) are derived in Appendix 2.12.3, and the integration corresponding to the expected values are approximated by numerical integration.

2.10   Simulations

In this section, we perform a number of simulation-based evaluations to assess the efficacy of the proposed TP-EKF filter. In doing that, we use the GP-EKF filter, Random Matrix (RM) and Random Hyper-surface Matrix (RHM) methods as different baselines. We perform our evaluations as follows:

- **Evaluation Scenarios**: We consider three different scenarios, namely, S_1, S_2 and S_3, with relevant maneuvering motion models and shapes. These scenarios are outlined in Table 2.1

Table 2.1: Scenarios for the experimental evaluation.

Scenario	Measurement Noise Noise	Process Noise Noise	Clutter	Number of Shapes	Baselines
S_1	Gaussian	Gaussian	-	2	GP-EKF, RHM
S_2	Student's-t	Student's-t	-	2	GP-EKF, RHM
S_3	Student's-t	Student's-t	Uniform	1	RM

It is worth noting that, given the fact the RHM method (used in Scenarios S_1 and S_2) is overly sensitive to the parameter initialization step [11], particularly to the number of Fourier Coefficients and their covariances, we observed that no set of common parameters can satisfy both shapes T_1 and T_2. Hence, careful initializations were carried out to maximize the performance of RHM as in [10].

- **Performance Metrics**: We consider three performance metrics: Mean Square Error (MSE), Intersection-Over-Union (IOU) [73], and PCRLB, in assessing their performance. Here, the IOU is used to assess the performance of different

filters in their target shape estimation, which is defined by

$$\mathbf{IOU}(R, \hat{R}) = \frac{\mathbb{A}(\hat{R} \cap R)}{\mathbb{A}(\hat{R} \cup R)}. \qquad (2.10.1)$$

where $\mathbb{A}(.)$ denotes the area operator that returns the area of a region, R represents the true region that is occupied by the extended target, and $\hat{R}$ represents the estimated region of the extended target. With this definition, the closer the value of the $\mathbf{IOU}$ to unity, the better the shape estimation is;

- **Reproducibility**: All evaluations were repeated across 100 Monte Carlo runs, and we only show the average performances.

- **Computational Costs**: To ensure that the improvements from the proposed method do not come with unacceptably large computational costs, we measured the average CPU time for the prediction and update stages upon receiving each measurement, averaged across multiple runs. We report these runtimes in relevant sections below.

In all cases, the target moves across a two-dimensional surveillance region with the dimensions of $[-1000, 1000]$m $\times$ $[-1000, 1000]$m over a 100-second time interval, and surface scattering points are considered to be the source of measurements. The number of scattering points is assumed to be known for the tracker, which follows a Poisson distribution with event rate $\lambda = 5 \times 10^{-2}$m^{-2}. The number of angle segments, N, is set to $N = 10$.

2.10.1   Evaluation of Scenario S_1

In this scenario, which mimics a system without heavy-tailed noise, we evaluate the performance of the proposed TP-EKF algorithm against two baselines GP-EKF and RHM, using two different shapes of extended targets, namely T_1 and T_2. In both cases the motion has three stages. In the first stage, 1-25s, the target moves with a nearly constant velocity. In the second stage, 26-75s, the motion model changes to a constant turning model with a small turn rate. Finally, during the final stage, 76-100s, the target moves with the original constant velocity model. The relevant parameters of the simulation are shown in Table 2.2.

Table 2.2: Parameter values for the simulation of scenario S_1.

Parameter	Notation	Value (Range)
Sampling time of the sensor	$T^{Sampling}$	1s
SD of the sensor noise covariance	$\sigma_{x,y}^R$	0.25 ms^{-1}
Initial state of the target	X_0^{True}	$[0\text{m}, 2.4 \text{ ms}^{-1}, 0\text{m}, 0 \text{ ms}^{-1}, 0 \text{ rad}, 0 \text{ rads}^{-1}]^T$
SD of the process noise covariance (velocity)	$\sigma_{x,y}^Q$	0.1 ms^{-1}
SD of the process noise covariance (heading)	σ_ψ^Q	0.001 rads^{-1}

The filter is initialized as,

$$\mathbf{x}_0 = \mathbf{x}_0^{True} + \tilde{\mathbf{x}}, \tag{2.10.2a}$$

$$\tilde{\mathbf{x}} \sim \mathcal{N}(0, P_0). \tag{2.10.2b}$$
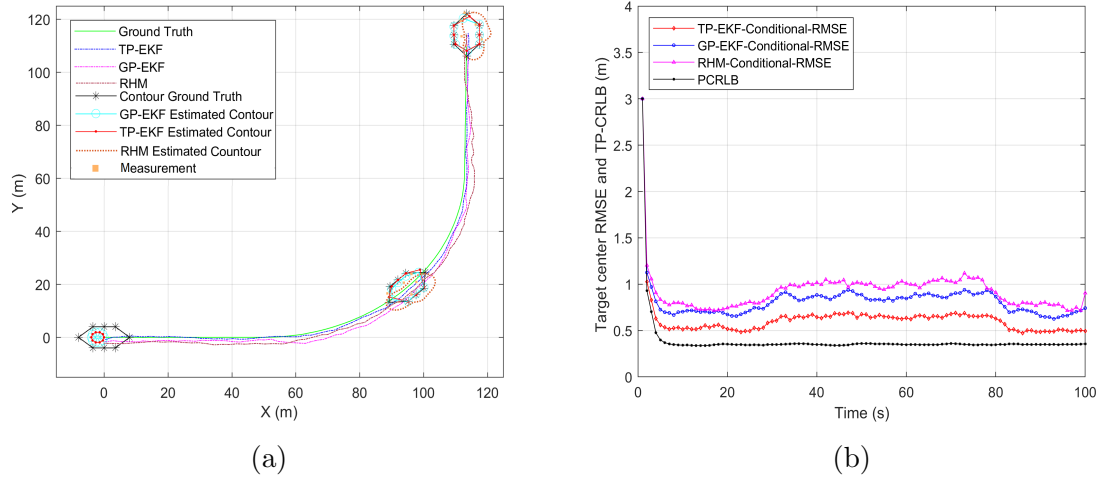
Figure 2.2: Performance Results for Scenario S_1 for Shape T_1: (a) Estimated trajectory and shape. (b) RMSE of the position against target center and conditional PCRLB.

where

$$
P_0 = \mathbf{diag}
\begin{bmatrix}
2.5\text{m} \\
0.15 \text{ ms}^{-1} \\
2.5\text{m} \\
0.15 \text{ ms}^{-1} \\
0.1 \text{ rad} \\
0.001 \text{ rads}^{-1}
\end{bmatrix} .
\tag{2.10.3}
$$

We show the resulting performance of the evaluation for shapes T_1 and T_2 in Figures 2.2 and 2.3, respectively. In both cases, we show (Figures 2.2(a) and 2.3(a)) the estimated trajectories, and estimated shapes for different values of k. To avoid cluttering the illustration, we show these for three different values of k, $k = \{1, 60, 100\}$ s. In addition to this, for both cases, in Figures 2.2(b) and 2.3(b), we show the evolution of RMSE compared to the PCRLB.

Table 2.3: Performance Results for Scenario S_1 using **IOU** and average RMSE values of the heading estimates (Gaussian noise).

Target Shape	IOU			RMSE (rad)	
	GP-EKF	**RHM**	**TP-EKF**	**GP-EKF**	**TP-EKF**
T_1	0.9100	0.7300	0.9400	0.0716	0.0641
T_2	0.8700	0.8500	0.8900	0.0807	0.0763
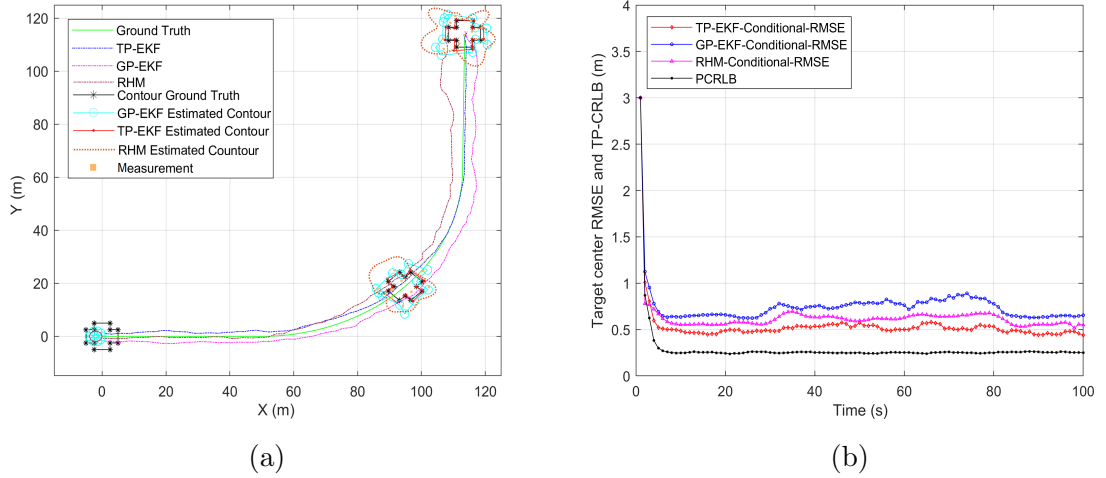
Figure 2.3: Performance Results for Scenario S_1 for Shape T_2: (a) Estimated trajectory and shape. (b) RMSE of the position against target center and conditional PCRLB.

These results show that the proposed TP-EKF method outperforms both GP-EKF and RHM methods, especially in terms of target contour estimation, for both the shapes. Furthermore, it is evident that although RMSEs of all the methods converge, the overall absolute error between the theoretical PCRLB and the RMSE of the proposed method is significantly lower than GP-EKF and RHM. We then show the the **IOU** performance and the average steady-state RMSE values of the heading estimates in Table 2.3. It is worth noting that the RHM method does not offer heading angle estimation (since the state information does not capture this). When comparing the runtime performance of the TP-EKF and GP-EKF, there is no

notable difference in their performance, with both the methods taking an average 2.3 ms for the overall computation. It can be seen that this tuned RHM initialization offers some occasional benefits, but these benefits are not sustained throughout the simulation. However, the proposed method does not suffer from such issues. Overall, the proposed TP-EKF method can outperform the GP-EKF and RHM methods on ETT in the presence of Gaussian noise (both measurement and process) conditions.

2.10.2   Evaluation of Scenario S_2

Although this scenario is similar to S_1 in terms of settings (see Table 2.2) and shapes of targets, this scenario simulates the heavy-tailed noise by considering the additive measurement and process noise, to follow the Student's-t distribution. Following [74], the heavy-tailed process and measurement noises are generated by relying on the following model:

$$
\mathcal{V}_k \sim \begin{cases} \mathcal{N}(0, Q), & \text{with probability } 0.9 \\ \mathcal{N}(0, 2Q), & \text{with probability } 0.1 \end{cases}
$$

$$
w_k \sim \begin{cases} \mathcal{N}(0, R), & \text{with probability } 0.9 \\ \mathcal{N}(0, 100R), & \text{with probability } 0.1. \end{cases}
$$

where Q and R denotes the same process and measurement noise models used in Section 2.4, namely, the Gaussian Noise. The main intention of this particular simulation scenario is to demonstrate the ability of the model to robustly handle a heavy-tailed noise case when estimating the shapes of extended targets. As such, the process noise is not accounted to be an extreme case of heavy-tailed noise, and hence the trajectory

estimations are expected to be similar to scenario S_1.

We show the resulting performance of the evaluation for shapes T_1 and T_2 in Figures 2.4 and 2.5, respectively. In both cases, like before, we show (Figures 2.4(a) and 2.5(a)) the estimated trajectories, and estimated shapes for different values of $k = \{1, 60, 100\}$s, and the evolution of RMSE compared against the PCRLB in Figures 2.4(b) and 2.5(b). In addition to these, we also show the performance of target orientation estimation, for one of the shapes, namely, T_1, in Figure 2.6. Although a number of observations, similar to that of Scenario S_1, can be drawn here, it is worth noting that the proposed TP-EKF method outperforms the GP-EKF method, when compared using RMSE and heading orientation estimations. It can be clearly seen that the estimations from GP-EKF suffers high variations while the same from TP-EKF method are very stable, both on RMSE and heading. Finally, we show the **IOU** performance and the average steady-state RMSE values of the heading estimates in Table 2.4. When comparing the runtime performance of the TP-EKF and RHM methods, we found that the runtimes were 2.3 ms and 3.5 ms, respectively, indicating that TP-EKF can outperform the RHM method. Overall, the proposed TP-EKF method can outperform the GP-EKF and RHM methods on ETT in the presence of Student's-t noise (both measurement and process) conditions.

2.10.3   Evaluation of Scenario S_3

In the previous sets of simulation scenarios, S_1 and S_2, the baselines were GP-EKF and RHM. Although these were sufficient enough to demonstrate the capability of the proposed filter, given the fact that RM method can also offer complex shape deductions, a more compelling evaluation would to assess the TP-EKF against RM

(a)   (b)
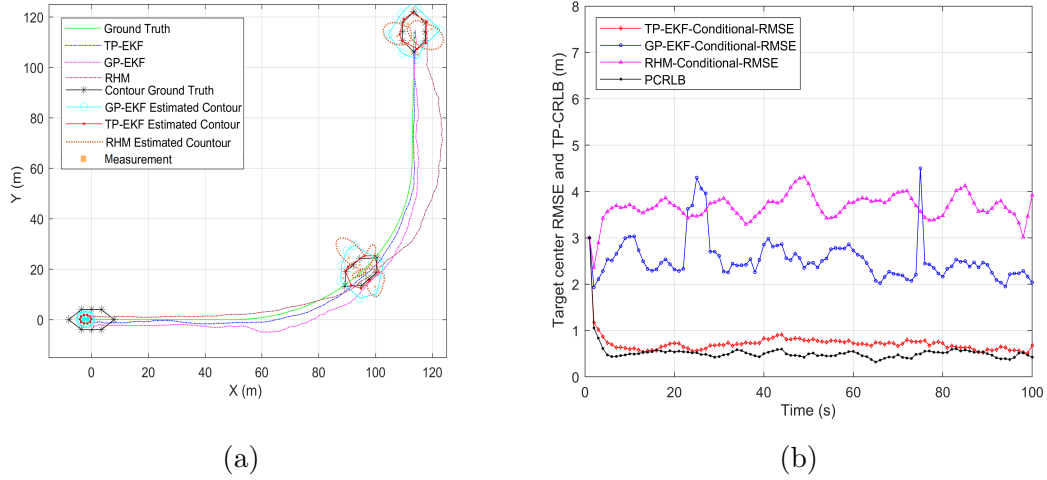
Figure 2.4: Performance Results for Scenario S_2 for Shape T_1: (a) Estimated trajectory and shape. (b) RMSE of the position against target center and conditional PCRLB.

Table 2.4: Performance Results for Scenario S_2: IOU and average RMSE values of the heading estimates (TP noise).

Target Shape	IOU			RMSE (rad)	
	GP-EKF	RHM	TP-EKF	GP-EKF	TP-EKF
T_1	0.6800	0.4800	0.9300	0.0972	0.0642
T_2	0.6300	0.5300	0.8900	0.1180	0.0714

method. Scenario S_3 attempts to offer this, particularly in a more realistic setting with clutter. However, to avoid complex experimental combinations, and to simplify the analysis, especially in line with the RM method, we opt for a simpler target shape T_3, which is ellipsoidal. Such an assumption is perfectly valid given that the RM-method assumes that the shape of the extended target is ellipsoidal. The presence of clutter mimics a case whereby the shape inferencing is done amidst false alarms. Apart from the target shape and clutter, other parameter settings, and sensor and target configurations remain similar to scenarios S_1 and S_2, except:
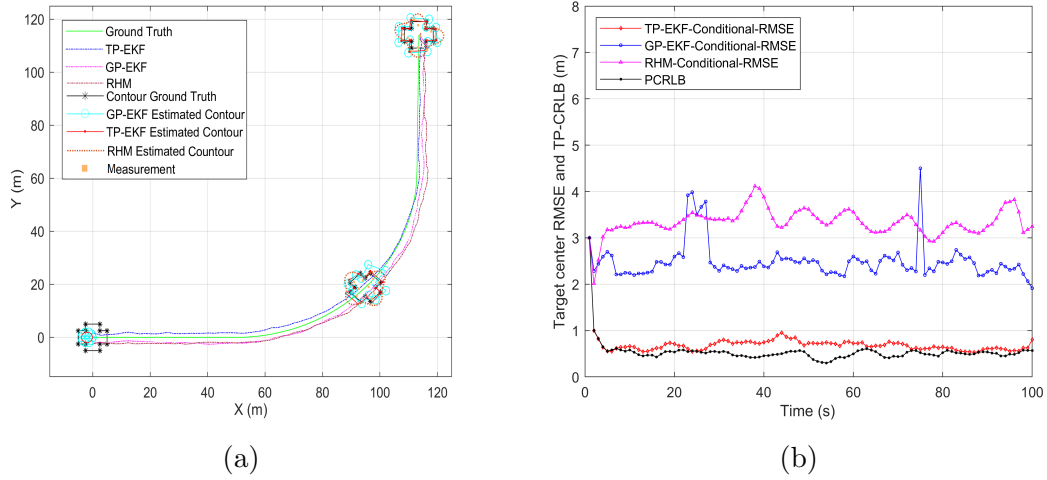
Figure 2.5: Performance Results for Scenario S_2 for Shape T_2: (a) Estimated trajectory and shape. (b) RMSE of the position against target center and conditional PCRLB.

- The motion model of the target is split into three phases: In the first phase, 0-40s, the target follows a nearly constant velocity model with velocity vectors of $V_x = 1$ ms^{-1}, $V_y = 0$ ms^{-1}. In the second stage, 41-55s, it switches to a constant turn model with turn rate of $6.14°$ s^{-1}. Finally, in the third stage, from 76 -100s, the target returns back to the constant velocity model of $V_x = 0$ ms^{-1}, $V_y = 1$ ms^{-1};

- Sensor's field of view(FoV) contains a uniformly distributed clutter. The number of clutters are Poisson distributed with a rate parameter of $\lambda_c = 1e^{-4}$ m^{-2}. The gating strategy used in this section ensures that 99% of target generated measurements fall into the gating region of the target ($\alpha = 0.99$). The gating region for TP-EKF is constructed with the strategy proposed in section 2.8, and the gating region for the RM method is calculated according to the traditional Chi-Square distribution.

55
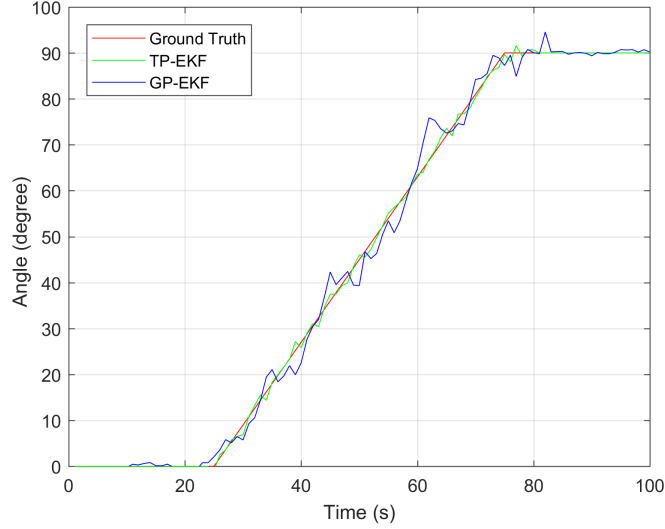
Figure 2.6: Performance on target orientation estimation for Scenario S_2 for Shape T_1 (TP noise).

We show the resulting performance of the evaluation for the shape T_3 in Figures 2.7 and 2.8. Figure 2.7(a) shows the estimated trajectory, and the estimated shapes at different time points of $k = \{15, 30, 45, 60, 75, 90\}$s, and the evolution of RMSE compared against the PCRLB in Figure 2.7(b). Figure 2.8 shows the variation of the estimation of the target orientation with time. From these results, it is clear that both RM and the proposed method offers similar accuracy in terms of centroid estimation, when compared against the PCRLB. However, this is an expected outcome, as the RM method, as opposed to TP-EKF, uses the average of all centroid measurements. However, a closer inspection of these algorithms revealed that there was a notable difference in terms of **IOU** criteria. The average **IOU** for the proposed algorithm (over 100 Monte Carlo runs) is 0.93, which is far superior to the **IOU** resulting from RM, which was 0.64. Furthermore, the variation of the orientation estimation shows the proposed TP-EKF easily outperforming the RM method. When
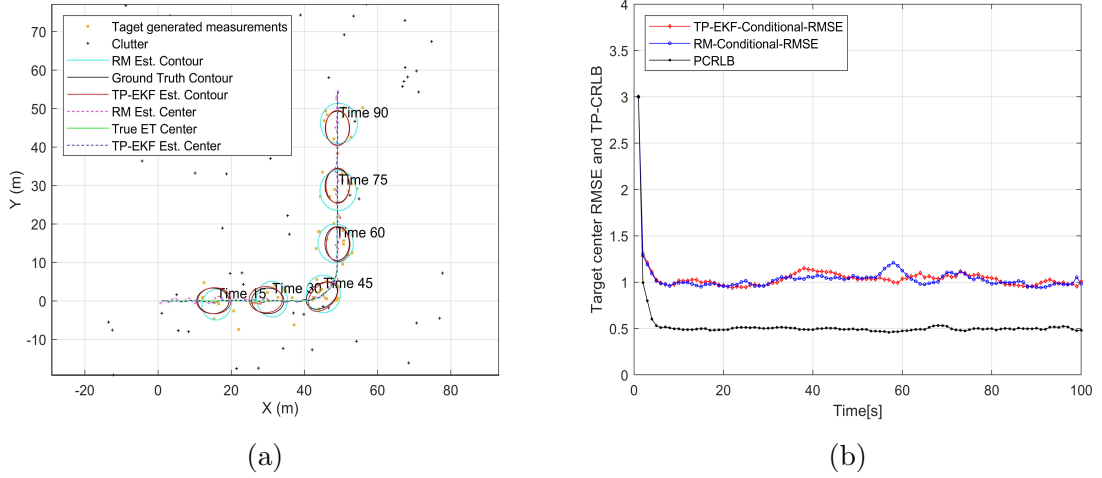
Figure 2.7: (a) True and estimated trajectory and shape. (b) The position Error corresponding to target center and conditional PCRLB.

comparing the runtime performance of the TP-EKF and RM methods, we found that the runtimes were 2.5 ms and 1.1 ms, respectively. Although the RM method was able to outperform the proposed technique in terms of runtime performance, the overall performance on shape inference, orientation and path tracking was remarkably good. Overall, the proposed method offers excellent results when compared against the RM method albeit taking extra runtime.

2.11 Conclusions

In this chapter, a novel TP-based approach for the extended target tracking problem was proposed. We proposed the use of TP for modeling the hidden target extent, in parallel to estimating the kinematic state of the target. An efficient recursive TP algorithm that does not suffer from dimensionality increase was derived. In doing so, we have considered all necessary (re)formulations for addressing extended target
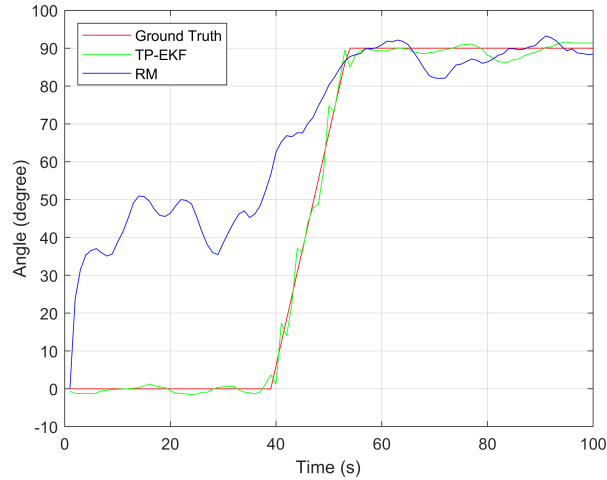
Figure 2.8: Ellipsoidal ET orientation estimation in presence of clutter, Student's-t process and measurement noise.

tracking problems using the proposed TP-EKF algorithm, including TP-based state-space and measurement models, gating, and online PCRLB models for assessing the RMSE errors. We evaluated the proposed algorithm under different conditions, using different target shapes and baselines, and the results show that the proposed algorithm outperforms a number of baseline methods, including in complex cases, where clutter, heavy-tailed noise and outliers are present. These results render the proposed algorithm as a better option for object classification and recognition purposes. In the future, we aim to use non-linear measurement models, multiple model estimators and the RFS and PDA frameworks to further increase the applicability of the proposed algorithm for general multitarget tracking problems.

2.12 Appendices

2.12.1 Moment of Measurement Noise

According to the common properties of Student's-t and Gaussian distribution [59], for a random variable $z = Ax + b$, the associated probabilities are

$$p(x) = \mathcal{MVT}(x; \hat{x}, v, P), \tag{2.12.1a}$$

$$p(z) = \mathcal{MVT}(z; A\hat{x} + b, v, APA^T). \tag{2.12.1b}$$

This property follows from deriving the Student's-t distribution with an IG kernel, prior to the Gaussian kernel. The relevant affine transformation of Gaussian random variables is, following [64], as follows:

$$Var[s_k^j(\mathbf{o}_k^j G_k^{s,j}\mathbf{x}_k^s + \mathbf{o}_k^j e_k^j)] = E[(s_k^j(\mathbf{o}_k^j G_k^{s,j}X_k^s + \mathbf{o}_k^j e_k^j))^2]$$

$$-E[s_k^j(\mathbf{o}_k^j G_k^{s,j}X_k^s + \mathbf{o}_k^j e_k^j)]^2 = E[(s_k^j\mathbf{o}_k^j G_k^{s,j}\mathbf{x}_k^s + s_k^j\mathbf{o}_k^j e_k^j)^2]$$

$$-\mu_s^2[\mathbf{o}_k^j G_k^{s,j}\mathbf{x}_k^s][\mathbf{o}_k^j G_k^{s,j}\mathbf{x}_k^s]^T, \tag{2.12.2}$$

$$E[(s_k^j\mathbf{o}_k^j G_k^{s,j}\mathbf{x}_k^s + s_k^j\mathbf{o}_k^j e_k^j)^2] = (\mathbf{o}_k^j G_k^{s,j}\mathbf{x}_k^s)E[(s_k^j)^2]$$

$$(\mathbf{o}_k^j G_k^{s,j}\mathbf{x}_k^s)^T + E[(s_k^j)^2]\mathbf{o}_k^j E[(e_k^j)^2](\mathbf{o}_k^j)^T = (\mu_s^2 +$$

$$(\frac{v-2}{v}\sigma_s)^2)[(\mathbf{o}_k^j G_k^{s,j}\mathbf{x}_k^s)(\mathbf{o}_k^j G_k^{s,j}\mathbf{x}_k^s)^T + \mathbf{o}_k^j(\frac{v-2}{v}R_k^{s,j}$$

$$(\mathbf{x}_k^s))(\mathbf{o}_k^j)^T] + 2\mu_s^2 G_k^{s,j}\mathbf{o}_k^j(\nabla_x R_k^{s,j})P_k^s(\mathbf{o}_k^j)^T. \tag{2.12.3}$$

2.12.2   Partial Derivative of Measurement Equation

The partial derivatives of the measurement equation, with respect to the augmented state for linearization purposes, is as follows:

$$
H_k = \frac{d\mathbf{h}_k(\mathcal{X}_k)}{d\mathcal{X}_k} =
$$
$$
\frac{d}{d\mathcal{X}_k}[\mathbf{h}_k^1(\mathcal{X}_k)^T, \ldots, \mathbf{h}_k^n(\mathcal{X}_k)^T] =
$$
$$
\frac{d}{d\mathcal{X}_k}\mathbf{h}_k^j(\mathcal{X}_k) = \left[\begin{array}{cc} \frac{d\mathbf{h}_k^j(\mathcal{X}_k)}{d\mathbf{x}_k} & \frac{d\mathbf{h}_k^j(\mathcal{X}_k)}{d\mathbf{x}_k^s} \end{array} \right] \tag{2.12.4}
$$

The kinematic state partition can be calculated by

$$
\frac{d\mathbf{h}_k^j(\mathcal{X}_k)}{d\mathbf{x}_k} = \left[\begin{array}{cc} \frac{dh_k^j(\mathcal{X}_k)}{d\mathbf{x}_k^{center}} & \frac{dh_k^j(\mathcal{X}_k)}{d\psi_k} \end{array} \right] \tag{2.12.5a}
$$

$$
\frac{dh_k^j(\mathcal{X}_k)}{d\mathbf{x}_k^{center}} = I + \frac{\partial \mathbf{o}_k^j(b)}{\partial b}|_{b=\mathbf{x}_k^{center}}
$$
$$
G^s(\theta_k^{Local,j}(\mathbf{x}_k^{center}, \psi_k))\mathbf{x}_K^s + \mathbf{o}_k^j(\mathbf{x}_k^{center})
$$
$$
\frac{\partial G^s(u)}{\partial u}|_{u=\theta_k^{Local,j}(\mathbf{x}_k^{center}, \psi_k)} \frac{\partial \theta_k^{Global,j}(\mathbf{a})}{\partial \mathbf{a}}|_{\mathbf{a}=\mathbf{x}_k^{center}}\mathbf{X}_k^s
$$
$$
\tag{2.12.5b}
$$

$$
\frac{dh_k^j(\mathcal{X}_k)}{d\psi_k} = -\mathbf{o}_k^j(\mathbf{x}_k^{center})\frac{\partial G^s(u)}{\partial u}|_{u=\theta_k^{Local,j}(\mathbf{x}_k^{center}, \psi_k)} \tag{2.12.5c}
$$

$$
\frac{\partial \theta_k^{Global,j}(\mathbf{a})}{\partial \mathbf{a}} = \frac{1}{||\mathbf{z}_k^j - \mathbf{a}||^2}\left[\begin{array}{cc} z_k^y - a^y, & -(z_k^x - a^x) \end{array} \right] \tag{2.12.5d}
$$

$$\frac{\partial G^s(u)}{\partial u} = \frac{\partial K(u, \boldsymbol{u}^f)}{\partial u}[K(\boldsymbol{u}^f, \boldsymbol{u}^f)]^{-1} \qquad (2.12.5e)$$

$$\frac{\partial K(u, \boldsymbol{u}^f)}{\partial u} = \frac{\partial}{\partial u}[\kappa(u, u_1^s), \dots, \kappa(u, u_{N^s}^s)] \qquad (2.12.5f)$$

$$\frac{\partial \mathbf{o}_k^j(\mathbf{b})}{\partial \mathbf{b}} = \frac{(\mathbf{z}_k^j - \mathbf{b})(\mathbf{z}_k^j - \mathbf{b})^T}{||\mathbf{z}_k^j - \mathbf{b}||^3} - \frac{1}{||\mathbf{z}_k^j - \mathbf{b}||}I. \qquad (2.12.5g)$$

where

$$\frac{\partial K(u, \boldsymbol{u}^f)}{\partial u} = -\frac{1}{l^2}\sin(u - u_i^f)\kappa(u, u_i).$$

Furthermore, the extent state portion can be calculated based on the following:

$$\frac{d\mathbf{h}_k^j(\mathcal{X}_k)}{d\mathbf{x}_k^s} = \mathbf{o}_k^j(\mathbf{x}_k^{center})G_k^s(\theta_k^{Local,j}(\mathbf{x}_k^{center}, \psi_k)). \qquad (2.12.5h)$$

2.12.3   TP-CRLB Derivation

The following statements are derived according to the Student's-t distribution,

$$-\log p(\mathcal{X}_{k+1}|\mathcal{X}_k) = c_1 +$$

$$\left(-\frac{n}{2} - v\right)\log\overbrace{\left(1 + [\mathcal{X}_{k+1} - \mathcal{F}_k\mathcal{X}_k]^T(\frac{\mathcal{Q}_k^{-1}}{v - 2})[\mathcal{X}_{k+1} - \mathcal{F}_k\mathcal{X}_k]\right)}^{\mathbb{T}},$$

$$(2.12.6a)$$

$$-\log p(z_{k+1}|\mathcal{X}_{k+1}) = c_2 + \left(-\frac{n}{2} - v\right)$$

$$\underbrace{\log\left(1 + [z_{k+1} - \mathcal{H}_{k+1}\mathcal{X}_{k+1}]^T(\frac{\mathcal{R}_{k+1}^{-1}}{v-2})[z_{k+1} - \mathcal{H}_{k+1}\mathcal{X}_{k+1}]\right)}_{\mathbb{Y}},$$

$$(2.12.6b)$$

$$-\log p(\mathcal{X}_k|\mathcal{X}_{k-1}) = c_1' + \overbrace{\left(-\frac{n}{2} - v\right)}^{\mathbb{E}}$$

$$\log\left(1 + [\mathcal{X}_k - \mathcal{F}_{k-1}\mathcal{X}_{k-1}]^T(\frac{\mathcal{Q}_{k-1}^{-1}}{v-2})[\mathcal{X}_k - \mathcal{F}_{k-1}\mathcal{X}_{k-1}]\right),$$

$$(2.12.6c)$$

$$-\log p(z_k|\mathcal{X}_k) = c_2' + \left(-\frac{n}{2} - v\right)$$

$$\underbrace{\log\left(1 + [z_k - \mathcal{H}_k\mathcal{X}_k]^T(\frac{\mathcal{R}_k^{-1}}{v-2})[z_k - \mathcal{H}_k\mathcal{X}_k]\right)}_{\mathbb{U}}.$$

$$(2.12.6d)$$

where c_1, c_2, c_1' and c_1' are constants, which are independent of $\mathcal{X}_\bullet$, and n is the dimension of the state space model. Assuming that $\mathcal{F}$ and $\mathcal{H}$ being linear and logarithmic, the following intermediate formulations can be made:

$$-\nabla_{\mathcal{X}_k} \log p(\mathcal{X}_{k+1}|\mathcal{X}_k) =$$

$$\left(-v - \frac{n}{2}\right) \times \frac{(\mathcal{F}_k^T)(\frac{\mathcal{Q}_k^{-1}}{v-2})(\mathcal{X}_{k+1} - \mathcal{F}_k\mathcal{X}_k)}{\mathbb{T}},$$

$$(2.12.7a)$$

$$- \nabla_{\mathcal{X}_{k+1}} \log p(\mathcal{X}_{k+1}|\mathcal{X}_k) =$$

$$(-v - \frac{n}{2}) \times \frac{(\frac{\mathcal{Q}_k^{-1}}{v-2})(\mathcal{X}_{k+1} - \mathcal{F}_k \mathcal{X}_k)}{\mathbb{T}}, \qquad (2.12.7\text{b})$$

$$- \nabla_{\mathcal{X}_{k+1}} \log p(z_{k+1}|\mathcal{X}_k) =$$

$$(-v - \frac{n}{2}) \times \frac{(\mathcal{H}_k^T)(\frac{\mathcal{R}_{k+1}^{-1}}{v-2})(z_{k+1} - \mathcal{H}_{k+1} \mathcal{X}_{k+1})}{\mathbb{Y}}, \qquad (2.12.7\text{c})$$

$$- \nabla_{\mathcal{X}_{k-1}} \log p(\mathcal{X}_k|\mathcal{X}_{k-1}) =$$

$$(-v - \frac{n}{2}) \times \frac{(\mathcal{F}_{k-1}^T)(\frac{\mathcal{Q}_{k-1}^{-1}}{v-2})(\mathcal{X}_k - \mathcal{F}_{k-1} \mathcal{X}_{k-1})}{\mathbb{E}}, \qquad (2.12.7\text{d})$$

$$- \nabla_{\mathcal{X}_k} \log p(\mathcal{X}_k|\mathcal{X}_{k-1}) =$$

$$(-v - \frac{n}{2}) \times \frac{(\frac{\mathcal{Q}_{k-1}^{-1}}{v-2})(\mathcal{X}_k - \mathcal{F}_{k-1} \mathcal{X}_{k-1})}{\mathbb{E}}, \qquad (2.12.7\text{e})$$

$$- \nabla_{\mathcal{X}_k} \log p(z_k|\mathcal{X}_k) =$$

$$(-v - \frac{n}{2}) \times \frac{(\mathcal{H}_k^T)(\frac{\mathcal{R}_k^{-1}}{v-2})(z_k - \mathcal{H}_k \mathcal{X}_k)}{\mathbb{U}}. \qquad (2.12.7\text{f})$$

63

With these, the derivatives in (2.9.4a) can be derived as:

$$B_k^{11} = E\{-\Delta_{\mathcal{X}_k}^{\mathcal{X}_k} \log p(\mathcal{X}_{k+1}|\mathcal{X}_k)\} = (-v - \frac{n}{2}) \times$$
$$E\left\{ \frac{\mathcal{F}_k^T (\frac{\mathcal{Q}_k^{-1}}{v-2})\mathcal{F}_k \times \mathbb{T} - [\mathcal{F}_k^T (\frac{\mathcal{Q}_k^{-1}}{v-2})(\mathcal{X}_{k+1} - \mathcal{F}_k \mathcal{X}_k)]^2}{\mathbb{T}^2} \right\},$$

$$\text{(2.12.8a)}$$

$$B_k^{12} = [B_k^{21}]^T = E\{-\Delta_{\mathcal{X}_k}^{\mathcal{X}_{k+1}} \log p(\mathcal{X}_{k+1}|\mathcal{X}_k)\} = (-v - \frac{n}{2}) \times$$
$$E\left\{ \frac{\mathcal{F}_k^T (\frac{\mathcal{Q}_k^{-1}}{v-2}) \times \mathbb{T} - \mathcal{F}_k^T \left[(\frac{\mathcal{Q}_k^{-1}}{v-2})(\mathcal{X}_{k+1} - \mathcal{F}_k \mathcal{X}_k) \right]^2}{\mathbb{T}^2} \right\}, \qquad \text{(2.12.8b)}$$

$$B_k^{22} = \underbrace{E\{-\Delta_{\mathcal{X}_{k+1}}^{\mathcal{X}_{k+1}} \log p(\mathcal{X}_{k+1}|\mathcal{X}_k)\}}_{B^{22a}} +$$
$$\underbrace{E\{-\Delta_{\mathcal{X}_{k+1}}^{\mathcal{X}_{k+1}} \log p(z_{k+1}|\mathcal{X}_{k+1})\}}_{B^{22b}}, \qquad \text{(2.12.8c)}$$

$$B^{22a} = (-v - \frac{n}{2}) \times$$
$$E\left\{ \frac{(\frac{\mathcal{Q}_k^{-1}}{v-2}) \times \mathbb{T} + \left[(\frac{\mathcal{Q}_k^{-1}}{v-2})(\mathcal{X}_{k+1} - \mathcal{F}_k \mathcal{X}_k) \right]^2}{\mathbb{T}^2} \right\}, \qquad \text{(2.12.8d)}$$

64

$$B^{22b} = (-v - \frac{n}{2}) \times E\left\{ \frac{\mathcal{H}_{k+1}^T (\frac{\mathcal{R}_{k+1}^{-1}}{v-2})\mathcal{H}_{k+1}}{\mathbb{Y}} - \right.$$

$$\left. \frac{[\mathcal{H}_{k+1}^T (\frac{\mathcal{R}_{k+1}^{-1}}{v-2})(z_{k+1} - \mathcal{H}_{k+1}\mathcal{X}_{k+1})]^2}{\mathbb{Y}^2} \right\}, \qquad (2.12.8e)$$

$$N_k^{11} = E\{-\Delta_{\mathcal{X}_{k-1}}^{\mathcal{X}_{k-1}} \log p(\mathcal{X}_k|\mathcal{X}_{k-1})\} = (-v - \frac{n}{2}) \times$$

$$E\left\{ \frac{\mathcal{F}_{k-1}^T (\frac{\mathcal{Q}_{k-1}^{-1}}{v-2})\mathcal{F}_{k-1}}{\mathbb{E}} - \right.$$

$$\left. \frac{[\mathcal{F}_{k-1}^T (\frac{\mathcal{Q}_{k-1}^{-1}}{v-2})(\mathcal{X}_k - \mathcal{F}_{k-1}\mathcal{X}_{k-1})]^2}{\mathbb{E}^2} \right\}, \qquad (2.12.8f)$$

$$N_k^{12} = [N_k^{21}]^T = E\{-\Delta_{\mathcal{X}_{k-1}}^{\mathcal{X}_k} \log p(\mathcal{X}_k|\mathcal{X}_{k-1})\} = (-v - \frac{n}{2}) \times$$

$$E\left\{ \frac{\mathcal{F}_{k-1}^T (\frac{\mathcal{Q}_{k-1}^{-1}}{v-2}) \times \mathbb{E} - \mathcal{F}_{k-1}^T [(\frac{\mathcal{Q}_{k-1}^{-1}}{v-2})(\mathcal{X}_k - \mathcal{F}_{k-1}\mathcal{X}_{k-1})]^2}{\mathbb{E}^2} \right\}, \qquad (2.12.8g)$$

$$N_k^{22} = \underbrace{E\{-\Delta_{\mathcal{X}_k}^{\mathcal{X}_k} \log p(\mathcal{X}_k|\mathcal{X}_{k-1})\}}_{N^{22a}} + \underbrace{E\{-\Delta_{\mathcal{X}_k}^{\mathcal{X}_k} \log p(z_k|\mathcal{X}_k)\}}_{N^{22b}}, \qquad (2.12.8h)$$

$$N^{22a} = (-v - \frac{n}{2}) \times$$

$$E\left\{ \frac{(\frac{\mathcal{Q}_{k-1}^{-1}}{v-2}) \times \mathbb{E} + [(\frac{\mathcal{Q}_{k-1}^{-1}}{v-2})(\mathcal{X}_k - \mathcal{F}_{k-1}\mathcal{X}_{k-1})]^2}{\mathbb{E}^2} \right\}, \qquad (2.12.8i)$$

65

$$N^{22b} = (-v - \frac{n}{2}) \times$$

$$E\left\{ \frac{[\mathcal{H}_k^T](\frac{\mathcal{R}_k^{-1}}{v-2})[\mathcal{H}_k^T]^T \times \mathbb{U} - [\mathcal{H}_k^T(\frac{\mathcal{R}_k^{-1}}{v-2})(z_k - \mathcal{H}_k \mathcal{X}_k)]^2}{\mathbb{U}^2} \right\}.$$

(2.12.8j)

Chapter 3

Two- and Three-Dimensional Extended Target Tracking Using Random Polytopes

3.1 Abstract

Extended Target (ET) generates multiple measurements in a single scan from unknown sources of measurements distributed along their bodies. In this paper, a novel extended target tracking approach for filled extended objects in two- and three-dimensional spaces with arbitrary shapes using a Random Polytope (RP) shape constructor is introduced. The proposed algorithm is capable of handling the important challenge that arises when tracking extended targets, namely, self-occlusion. The proposed shape function based on the Random Polytopes leads to a recursive Gaussian state estimator for tracking extended targets in the presence of measurement noise and occlusions. The performance of proposed algorithm is demonstrated using

a number of simulations covering two- and three-dimensional cases. Our result indicate that the proposed algorithm outperforms other relevant methods both in terms of state estimation, when compared against the Posterior Cramer-Rao Lower Bound, and in shape estimation, evaluated based on a distance metric defined based on the proposed RP shape description.

3.2   List of Notations

Throughout this chapter, scalars or scalar-valued functions are denoted with non-bold symbols, e.g., y_k, vectors or vector-valued functions are denoted with bold symbols, e.g., $\mathbf{u}_k$, and matrices are denoted with capitalized symbols, e.g., A. Furthermore, a list of some of the used notations and their explanations are listed below.

$\Phi(\mathbf{x}, \mathbf{w})$ Random Polytopes shape function

$h(\mathbf{x}_i)$ Half-space over point $\mathbf{x}_i$

$\mathbf{w}$ Weights of half-spaces

$\mathbf{x}_k$ Augmented state

$\bar{\mathbf{x}}_k$ Kinematic state

$\mathbf{x}_k^{shape}$ Extent state

$\mathbf{w}$ Weights of half-space

$\mathbf{y}_k$ Actual measurements

$\mathbf{z}_k$ Source of measurements

ω Measurement noise

s_k Contour scaling factor

3.3   Introduction

Extended target (ET) tracking (ETT) has a number of applications in several areas, including airborne, maritime, and ground surveillance using high-resolution sensors, autonomous vehicular systems, and in video tracking [7]. The key challenge in ETT compared with conventional target tracking is that targets are no longer point targets, and as such, they can take any filled shape. This difference leads to an important phenomenon: more than one measurement can be returned per target whereas in point target (PT) tracking (PTT), at-most one measurement is received per target per scan. The actual number of measurements often varies with time, depending on the shape of the target, location of the sensor, and whether any part of the target is occluded by another part of the same target (self-occlusion). Inevitably, ETT algorithms are required not only to estimate kinematic states of the target, but also their shapes. Although the kinematic state estimation problem is often simplified by treating the target as a point target, where the centroid of the ET represents the target as a PT, the shape estimation still remains a challenge in ETT.

Several methods are proposed in the literature for shape estimation [4, 6, 7, 10, 11, 31, 75, 76, 77, 78, 79, 80]. Often the shape of a target is assumed as rectangular [75, 76], elliptical [7, 10], or sticks [77]. Complex shapes are often estimated using the composition of geometrical shapes, such as multiple overlapping ellipses [31]. The star-convex shape descriptor using the radial function is proposed in [11, 78], where

the radial basis functions are used for recursively estimating the extent and kinematic state of a target using the Gaussian Process (GP). In [4], an approach for shape description is provided using the Random Finite Sets (RFS) theory. The key idea here is to represent a set of measurements over the field of view of a sensor as a spatial point process, such as an inhomogeneous Poisson Point process. A number of enhancements to this approach have also been developed in [6, 79].

However, one major assumption in existing literature is that the observations are generated only from the contour points (and/or a scaled version of the contour points) of the target [80]. Although this assumption is acceptable in some cases, it effectively disregards the notion of filled objects, and thus possible measurements from the of the ETs. Assuming measurements originating only from the contour points can limit the ability of the algorithms to accurately estimate the centroid of the target, in addition to yielding poor shape estimates when measurements indeed originate from the interior points of targets.

One of the subtle, but important aspects that underpins the shape inferencing procedure is self or mutual occlusion [81], where a part of an extended target occludes another part of itself or that of another, respectively. This poses a serious challenge to the shape estimation process due to potentially conflicting sets of measurements over time. Without accounting for the possibility of occlusion, these measurements can misguide not only the shape inferencing process with temporally varying shapes, but also the kinematic state estimation process with incorrect, time-varying centroids. The issues become more pronounced in the presence of noise and clutter. ETT in the presence of self or mutual occlusion has not received much attention in the literature. In [73, 81], self occlusion is handled using the concept of observable sides from

multiple measurements. However, this approach is limited to two primitive shapes, namely, rectangular and ellipsoidal, and more importantly limited to measurements originating only from target contours. In [82], self occlusion is handled using partial likelihoods. However, this approach is also limited to measurements originating from contour points and the notion of self occlusion is limited to specific cases.

To the best of our knowledge, the only work in the ETT literature we are aware of that accounts for filled targets and measurements from the interior of the target is the generalized Random Hyper-surface Models using Level-Sets (LS-RHM) algorithm [80]. The LS-RHM approach has some limitations:

- It requires a regularization term to capture different features of the extended object. For instance, regularization is used as a correction mechanism for handling incorrect initialization or the curvature of the estimated shape [80]. This is because the LS-RHM approach inherits the non-parametric characteristics of the underlying level-set methods [83];

- Its computational time complexity is $\mathcal{O}(n^3)$, which may be prohibitive in real-time tracking applications; and

- It cannot be generalized both in terms of regularization term (between applications) and in terms of dimensionality. That is, there is no generalization to higher dimensional spaces, and it is not directly usable for three-dimensional object tracking.

In this paper, we propose a novel ETT algorithm that is capable of estimating both the shape and kinematic states, while addressing the above shortcomings. More specifically, we use Random Polytopes (RPs) [84, 85], to approximate the shapes of

convex bodies. Although the notion of using RPs for approximating shapes has long existed in computer science (see [84, 85, 86, 87]), the use of RPs in the context of ETT has not been done before. We see this as a major step towards deriving realistic and practically useful ETT algorithms. However, this is not without challenges. One of the key challenges is embedding shape inferencing using RP as part of a state estimation framework. This has to be achieved while ensuring low and accurate estimations. The proposed RP-based algorithm for shape inferencing results in a simplified and effective approach to handle self occlusions. This paper makes the following key contributions:

- introduces the notion of using RPs for shape inferencing in the context of ETT;

- enables the definition of any extended target shapes, going beyond simple shapes such as rectangles, ellipses or star-convex shapes, that have been studied hitherto;

- embeds shape inferencing using RP as part of the Bayesian framework for kinematic state and shape estimation;

- provides an estimation approach for accounting for all measurements from an extended target, without being limited to contour points; and

- results in robust approach for handling self occlusions by correctly partitioning target measurements;

- yields a generic and extensible shape inferencing algorithm for extended targets that can operate in higher dimensions and is free from the notion of regularization.

These contributions render the proposed algorithm applicable to real world problems in higher dimensions. The rest of this paper is organized as follows. We first present the relevant mathematical background into RPs and shape descriptor functions in Section 3.4. We then show how the self occlusion problem can be addressed in the proposed algorithm with the help of shape descriptor functions in Section 3.5. This is then followed by Section 3.6, where we address RP-based shape inferencing in a Bayesian framework. To facilitate the benchmarking process, we derive the Posterior Cramér-Rao Lower Bound (PCRLB) for our case in Section 3.7. We present our simulation studies in Section 3.8 before concluding the paper in Section 3.9.

3.4 Random Polytopes as Shape Function For Extended Target

3.4.1 Random Polytopes

Let $\mathcal{S}$ be a set containing a number of non-empty, convex, compact bodies in a d-dimensional Euclidean space. Furthermore, let $S \in \mathcal{S}$ be one of those compact bodies. Let there be n independent random points, $\{x_1, x_2, \ldots, x_n\}$, chosen uniformly over S. Then, the convex hull constructed by these points is called a Random Polytope (RP) in the convex set S. Here, it is a Polytope since it is the convex hull of a set of points, and it is random as these points are randomly distributed across the compact body [84, 88, 89, 90, 91].

RPs are used in several application areas, including algorithmic complexity, compilers, mathematical optimization, statistics and biology [92, 93]. In our case, the primary interest is on expressing the shape of a compact body (in a d-dimensional

Euclidean space) using a set of RPs. This technique provides a method for capturing the complex shapes of extended targets, and thus underpins the key contributions of this paper.

An RP can be constructed using a number of methods, including convex hulls of random points, Gaussian polytopes, intersections of random half-spaces, and random projections of high-dimensional polytopes [94, 95]. The exact choice of methods for generating RPs, can often be subjective, based on a number of factors, including the asymptotic outcome, computational complexity, and algorithmic simplicity. In this paper, we will be using the intersections of the random half-spaces method where the RPs are generated by computing the intersection of the supporting half-spaces (due to its simplicity). More specifically, intersections are calculated over a set of random points x_i on the differentiable boundary of the shape S of the extended target. The half-spaces over the set of points $\mathbf{x}_i$ are denoted by $h(\mathbf{x}_i)$.

3.4.2 Shape Function of Random Polytopes

The shape function, Φ, of RPs can be defined as the intersection of supporting lines (in two-dimensional cases) and hyperplanes (in higher dimensions) at chosen points on their line/plane boundaries. Thus, the shape function $\Phi(\mathbf{x})$ defined over the intersection of half-spaces on a set of n points $\mathbf{x} = \{\mathbf{x}_1, \mathbf{x}_2, \ldots, \mathbf{x}_n\}$ is given by

$$\Phi(\mathbf{x}) = \bigcap_{i=1}^{n} h(\mathbf{x}_i) \tag{3.4.1}$$

The d-dimensional half-space $h(\mathbf{x}_i)$ over point $\mathbf{x}_i$ on the boundary of RP can be defined as

$$h(\mathbf{x}_i) = \begin{cases} 1, & l \geq 0 \\ 0, & \text{Otherwise} \end{cases} \tag{3.4.2}$$

where

$$l = \sum_{p=0}^{d} w_p.x_p \tag{3.4.3}$$

with w_p being the coefficients of the given half-space, and points $\mathbf{x}_i$ are represented in homogeneous coordinate form [96]. That is, $\mathbf{x}_i = [x, y, 1]^T$ and $\mathbf{x}_i = [x, y, z, 1]^T$ in $\mathbb{R}^2$ and $\mathbb{R}^3$ respectively. Now, as per set theory, a point $\mathbf{x}(\in \mathbb{R}^d)$ belongs to an intersection set, $\phi(n)$, iff:

$$(\mathbf{x} \in h(\mathbf{x}_1)) \wedge (\mathbf{x} \in h(\mathbf{x}_2)) \wedge \cdots \wedge (\mathbf{x} \in h(\mathbf{x}_n)) = \bigwedge_{i=1}^{n} h(\mathbf{x}_i) \tag{3.4.4}$$

Given that each half-space is represented as a binary value in (3.4.2), the logical operator ($\wedge$) can be replaced by the product operator ($\prod$). Thus,

$$\Phi(\mathbf{x}) = \prod_{i=1}^{n} h(\mathbf{x}_i) \tag{3.4.5}$$

However, the shape function defined in (3.4.2) is not continuously differentiable, and hence its direct use in filtering algorithms is limited. This issue, however, can be overcome by replacing the shape function with an approximated version of it, so
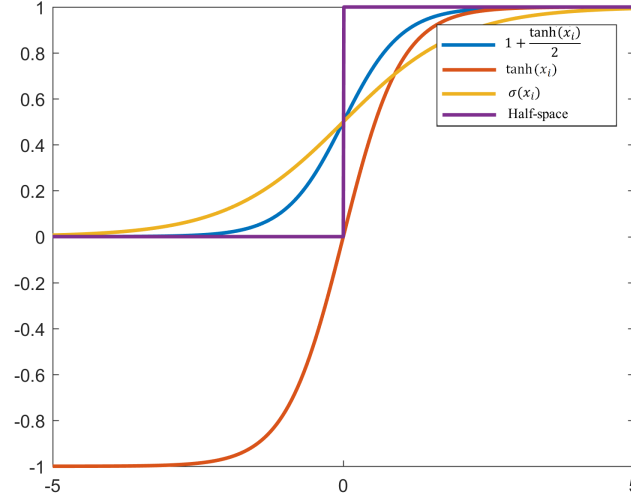
Figure 3.9: Examples of approximated versions of shape functions in $\mathbb{R}^2$.

that it can be differentiated everywhere. We show a number of such approximations in Figure 3.9. These include hyperbolic tangent (tanh) and logistic sigmoid, both continuous and differentiable across the domain. However, the range of the raw hyperbolic tangent can be negative, and hence the derivative can reach negative values. This can be addressed by using the modified version, namely, $\frac{1+\tanh(l)}{2}$, instead of $\tanh(l)$. These functions, and their derivatives are shown in Table 3.5. We also illustrate how these shape functions can be used to capture a realistic shape of an extended target in Figure 3.9.

Table 3.5: Derivatives of approximated half-space functions

Function	$\mathbf{h(x_i)}$	$\mathbf{h'(x_i)}$
Original tanh	$\tanh(x_i)$	$(1 - \tanh(x_i)^2)$
Modified tanh	$\frac{1+\tanh(x_i)}{2}$	$\frac{1}{2}(1 - \tanh(x_i)^2)$
Sigmoid ($\sigma(x_i)$)	$\frac{1}{1+e^{-x_i}}$	$\sigma(x_i)(1 - \sigma(x_i))$

A number of shape functions can now be obtained by replacing $h(\mathbf{x}_i)$ with the
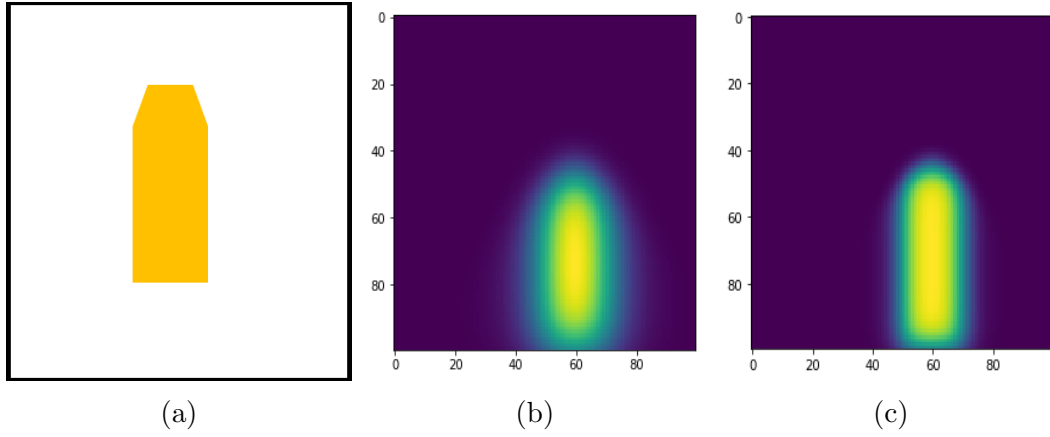
Figure 3.10: (a) Original shape (b) RP-based target shape constructed using the sigmoid shape function (c) RP-based target shape constructed using the tanh shape function.

corresponding half-space functions. For instance, in our case, shape functions when using the logistic sigmoid and modified hyperbolic tangent half-space functions are given by

$$\Phi(\mathbf{x}, \mathbf{w})_1 = \prod_{i=1}^{n} \frac{1}{1 + \exp(l)} \tag{3.4.6}$$

$$\Phi(\mathbf{x}, \mathbf{w})_2 = \prod_{i=1}^{n} \frac{1}{2}\left(1 + \frac{\exp(-2l) - 1}{\exp(-2l) + 1}\right) \tag{3.4.7}$$

where l is defined in (3.4.3), and $\mathbf{w} = [\mathbf{w}_0, \ldots, \mathbf{w}_n]$ represents the weights of the half-spaces. Both approximations of the half-spaces can generate the value of the shape function Φ between $[0, 1]$. However, half-space approximations with the hyperbolic tangent results in a much sharper contour than the sigmoid counterpart, owing to the differences in their slopes. Although it is possible to define additional transformations to the sigmoid function to increase its slope, the hyperbolic tangent is simpler, and

hence, is preferred over the sigmoid. Furthermore, we make two assumptions in defining the shape of an arbitrary target with the proposed method. The first is that the intersection of half-spaces is bounded, and the second assumption is that the computational complexity of deciding the existence of a point inside (or outside) the intersection is a constant.

Representing an extended target using the proposed RP shape function leaves parameters $\mathbf{w}_p$ (for $p = 0, \ldots, d$) to be computed. In fact, $\mathbf{w}_p$ (for $p = 0, \ldots, d$) are the coefficients and biases (intercepts) of the linear tangent half-spaces that form the contour of the extended target. These are used as adaptive variables and are updated during the filtering process. When using the hyperbolic tangent-based shape function as in (3.4.7), the level sets $\Phi(\mathbf{x}, \mathbf{w}) \gtrless 0.5$, for a given point $\mathbf{x}$, and decides where the point x lies in relation to the contour. That is, level sets $\Phi(\mathbf{x}, \mathbf{w}) > 0.5$, $\Phi(x, W) = 0.5$, and $\Phi(\mathbf{x}, \mathbf{w}) < 0.5$ denote that the point x is at the interior, boundary, and exterior of the extended target, respectively. This method, in comparison to the signed Mahalanobis distance shape function used in the RHM method [80], is relatively simple and has a constant-time computational complexity. More specifically, the signed Mahalanobis distance can assume different values at different sampling times due to occlusion, and additional computations are needed for eliminating such variability, rendering the method heavily compute-bound with a time complexity of $\mathcal{O}(n^3)$.

3.4.3 Representing Non-Convex Shapes

The use of RPs for capturing convex shapes can be extended to represent non-convex shapes by defining a generalized shape function that represents a non-convex shape

as a union of m convex RPs [97]. This can be achieved using the DeMorgan Law as follows:

$$\Phi(x, \mathbf{W}) = 1 - \prod_{j=1}^{m} \left(1 - \prod_{i=1}^{n} \left(\frac{1 + \frac{exp(-2\sum_{D=0}^{d} w_{j,i}^D \cdot x^D) - 1}{exp(-2\sum_{D=0}^{d} w_{j,i}^D \cdot x^D) + 1}}{2} \right) \right) \tag{3.4.8}$$

where $\mathbf{w} = [\mathbf{w}_0, \ldots, \mathbf{w}_m]$, as before, represents the weights of half-spaces of each polytope.

3.4.4 Augmented Extended Target State and Evolution Model

Let $\mathbf{x}_k$ be the augmented state of an extended target that is defined as

$$\mathbf{x}_k = \begin{bmatrix} \bar{\mathbf{x}}_k \\ \mathbf{x}_k^{shape} \end{bmatrix} \tag{3.4.9}$$

where $\bar{\mathbf{x}}_k$ and $\mathbf{x}_k^{shape}$ are the kinematic, and shape extension parts of the target. The kinematic part of the state often contains the positions and their derivatives as determined by the state transition model of choice, while the shape component, as discussed before, is expressed by the weights of half-spaces, namely, $\mathbf{w}$, whose length may vary depending on the number of half-spaces used in the shape description. To simplify the process, assume a two-dimensional spatial domain where the extended targets are moving with a constant velocity motion model, and a shape description using n half-spaces. Thus,

$$\bar{\mathbf{x}}_k = \begin{bmatrix} x_k \\ \dot{x}_k \\ y_k \\ \dot{y}_k \end{bmatrix} \tag{3.4.10}$$

and

$$\mathbf{x}_k^{shape} = \begin{bmatrix} \mathbf{w}_1(k) \\ \mathbf{w}_2(k) \\ \vdots \\ \mathbf{w}_n(k) \end{bmatrix} \tag{3.4.11}$$

If the assumptions on the spatial domain can be relaxed to consider a three-dimensional space, the kinematic and shape components will be extended using the homogeneous coordinate system. The state evolution model for an extended target then becomes

$$\mathbf{x}_{k+1} = F_k \mathbf{x}_k + \mathbf{v}_k \tag{3.4.12}$$

where F_k and $\mathbf{v}_k$ are representing the state transition matrix and the process noise at time k, where

$$F_k = diag\{\bar{F}_k, F_k^{shape}\}$$

with $\bar{F}$ and F_k^{shape} modeling the transitions of target centroid and target shape with time, respectively. Given that the shape of a target is invariant to time, F_k^{shape} can be replaced by an identity matrix, I. The process noise $\mathbf{v}_k$ is modeled by a zero mean Gaussian distribution with covariance matrix

$$Q_k = diag\{\bar{Q}_k, Q_k^{shape}\}$$

The extended target representation used in the generalized RHM method that uses the level-set method [80] is a chain of two-dimensional points constructing a polygon. Thus, it is a special case of the augmented state-space model outlined above, where the shape component is replaced by the vertices constructed by the intersection of half-spaces.

In our case, the number of half-spaces required to represent an extended target is assumed to be known a priori, and the RP shape function was observed to be less sensitive to the number of discriminate half-spaces. Although it is possible to develop a technique that dynamically estimates the number of discriminate half-spaces, it is beyond the scope of this paper.

3.4.5   Measurement Model for Extended Targets

As the core contributions of this paper rely on the augmented state-space model outlined above, it is essential to develop a pseudo-measurement model that conforms to the augmented model. In order to develop a pseudo-measurement model, we will rely on the following lemma:

Lemma 1.   Implicit Measurement Equation: *Consider a circular extended*

target. In the augmented state-space model, the extension part of the state vector $\mathbf{x}_k^{shape} = r_k$. *This is defined in [10] using a signed Euclidean distance shape function as follows:*

$$\Phi^c(\mathbf{x}_k, \mathbf{z}_k) = r_k - ||\mathbf{z}_k|| \tag{3.4.13}$$

where $||\mathbf{z}_k||$ *is represents the Euclidean norm of measurement.*

Here, the value of the shape description function Φ^c becomes $\Phi^c = 0$ if the measurement $\mathbf{z}_k$ is on the boundary of the shape, positive for observations belonging to the interior of the target, and negative for measurements falling outside the target. By assuming that the measurements only originate from the boundary of the target, and the actual noise-corrupted measurements are represented by $\mathbf{y}_k$, a pseudo-measurement model can be expressed as

$$h(\mathbf{x}_k, \mathbf{y}_k, \omega_k) := \Phi^c(\mathbf{x}_k, \underbrace{\mathbf{y}_k - \omega_k}_{\mathbf{z}_k}) = 0 \tag{3.4.14}$$

where ω_k is the noise term and $\mathbf{z}_k$ is the actual source of the measurements on the contour of the target. Thus, this pseudo-measurement model aids the filter in estimating the state of the target X_k in (3.4.9) when $h(\mathbf{x}_k, \mathbf{z}_k, w_k)$ is as close as possible to zero.

To account for the measurements originating from the interior of the target, a transformation parameter, $s_k \in [0, 1]$, can be used to tune this model further [78]. The derivation of a new implicit measurement model entails a practical value for

s_k, chosen from a known prior distribution, which is independent of the state, and scalable with the radius r_k. To aid this, the following transformed shape description function can be derived:

$$\Phi^s(\mathbf{x}_k, \mathbf{z}_k) = s_k.r_k - ||\mathbf{z}_k|| \tag{3.4.15}$$

By replacing Φ^c in (3.4.14) with Φ^s, an implicit measurement model that accounts for measurements originating from the interior of the targets can be developed. Using the concepts of RP and Lemma 1, the following pseudo-measurement model, which is the cornerstone of the proposed algorithm, can be derived:

$$h(\mathbf{x}_k, \mathbf{y}_k, \omega_k, s_k) := s_k^{-1}.\Phi(\underbrace{\mathbf{y}_k - \omega_k}_{\mathbf{z}_k}, \mathbf{x}_k^{shape}) = 0.5 \tag{3.4.16}$$

where $\mathbf{y}_k$, ω_k and $\mathbf{z}_k$ are the actual observation, noise and the source of the measurement, respectively. Furthermore, function Φ represents the RP shape function described before. We describe the method for finding an optimal value for the scaling factor $s_k \in [1, 2]$ in the latter sections of this paper.

3.5 Handling Self Occlusion

In estimating the shape of extended targets, self occlusion is an important aspect that requires careful attention. The relative position, and the angle of the observer with respect to the object influence the overall outcome of the estimation. This

effect is more pronounced in the three-dimensional case. We illustrate this problem in Figure 3.11, where the observable sides, and thus of the derived shape, of an extended target in a three-dimensional observable space is heavily influenced by the relative positioning of the target with respect to the observer.
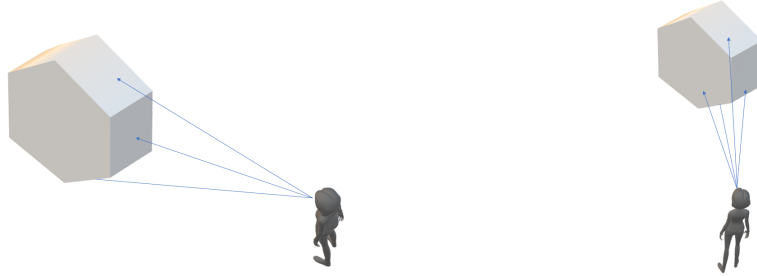
Figure 3.11: Dependency of observable sides on object and observer location in three-dimensional space.

Thus, algorithms producing shape estimations that are less influenced by the target-observer relationship, are useful in real world applications. In our case, we can optimize the pseudo-measurement model to differentiate between the measurements originating from the interior points and the contour points, and thereby infer the unobservable sides (or facets) of the targets. With these, it is possible to accurately estimate the true shape of an extended target over time.

Consider the plane $h_f(i)$ that contains the facet s_1 of the constructed RPs. The facet s_1 is observable from a point if the point lies in the open half-space on the other side of plane $h_f(i)$ [99]. For example, the facet s_1 in Figure 3.12(a) is observable from point A, but not from point B. Equally, the edge L_1 is observable from point A but not from point B, as shown in Figure 3.12(b).

The observability of a facet is underpinned by the fact that the center of an extended target is defined as a feasible interior point for the convex body built by

(a)   (b)
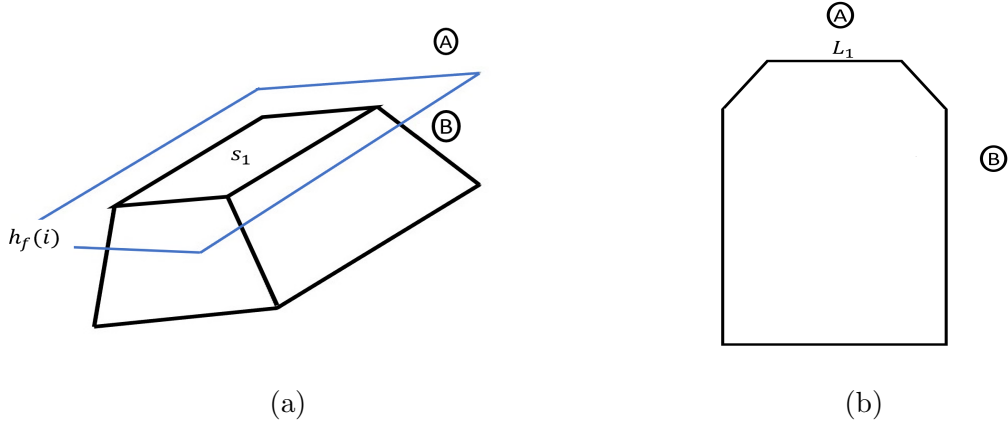
Figure 3.12: The visibility of a facet from two different half-spaces.

intersection of half-spaces. This intersection of half-spaces also defines the border of the extended target. Thus, at every time step, it is possible to estimate the side where the sensor is located. If the sensor is located on the open half-space, measurements can originate from that facet. This is repeatedly exploited for computing the probability of detection for each side of the extended target. However, the uncertainty in estimating the center and the RP representing the shape of target, must be accounted for, to ensure that the probability of detection is acceptable.

For each of the half-spaces constructing the convex body of the target, we define the probability of detection (P_d), as follows:

$$
\begin{aligned}
PD(h_i) &= 1 - h(\mathbf{w}_i) \\
&= 1 - \left(\frac{1 + \frac{\exp(-2\sum_{D=0}^{d} w_i^D.s_D)-1}{\exp(-2\sum_{D=0}^{d} w_i^D.s_D)+1}}{2} \right)
\end{aligned}
\tag{3.5.1}
$$

where s_D is the sensor location denoted by a homogeneous coordinate system, and w_D are the weights corresponding to the half-space for which the P_d is computed. Since,

the weights corresponding to half-space h_i are associated with some uncertainty, their covariances must be accounted for. For this purpose, instead of computing the exact P_d for a half-space h_i as in (3.5.1), the following P_d value is assigned to each of the facets:

$$P_d(h_i) = \sigma_h \cdot PD(h_i) \tag{3.5.2}$$

which accounts for the uncertainty in weights of the intended half-space (3.5.2). Furthermore, σ_h is the half-space measure of predictability. This value can be defined by inverse of the largest eigenvalue, inverse of the sum of the eigenvalues and continuous entropy of the covariance function of the corresponding facet. The entropy $H(\mathbf{w})$, for an information $\mathbf{w}$, can be computed as follows:

$$H(\mathbf{w}) = \int p(\mathbf{w}) \log p(\mathbf{w}) dL \tag{3.5.3}$$

for random variable L. If the random variable follows a multivariate Gaussian distribution with covariance Σ, which represents our case, the entropy will be computed as follows:

$$H(\mathbf{w}) = \frac{1}{2} \log((2 * \pi e)^n \det(\Sigma^{-1})) \tag{3.5.4}$$

where n is the dimension of the random variable. To ensure that the this entropy falls

into the standard half-space representation, the resulting entropy must be mapped onto the interval $[0, 1]$. This can be achieved as follows:

$$\sigma_h = \frac{\sin(H(\mathbf{w})) + 1}{2} \tag{3.5.5}$$

Therefore, at each time step k, the probability that the half-space i is observable by the sensor is now known.

3.5.1 Scaling Parameter as an Association Hypothesis

The distribution of the transformation parameter s_k in the pseudo-measurement model plays an important role in estimating the true shape of the extended target. However, in the literature, the distribution of s_k is assumed to be known a priori [10]. For instance, for the measurements originating from the contour of the extended targets, $s_k = 1$, with no spread. However, when considering extended targets, where measurements can also originate from the interior part of objects, the distribution of s_k becomes application-specific.

For extended targets, measurements are considered to be uniformly distributed along the target contour [101]. This can be used to find an approximate distribution of the scaling factor, $p(s_k)$, by using the RP shape function Φ. More specifically, a histogram of s_k can be generated across a number of measurements based on different RPs defining different half-spaces. However, as the histogram is relying on the shape function, it is heavily influenced by the shape of the target. We illustrate this for three different shapes in Figure 3.13.

As can be seen in Figure 3.13, the valid interval for the scaling parameter s_k is, $1 \leq s_l \leq 2$. Apart from this, the shape of the target decides the exact distribution
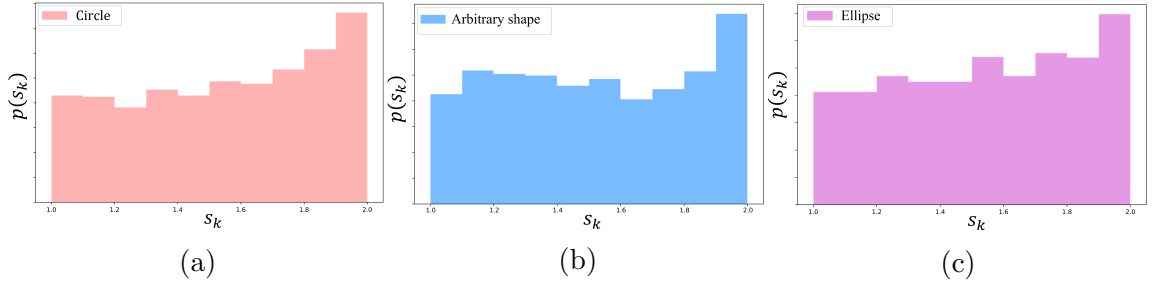
Figure 3.13: Distribution of scaling parameter s_k for different shapes (circle, arbitrary, and ellipse).

of the parameter. As such, there is no general approximation for the scaling factor. In fact, self occlusions exacerbate this problem even more. Even if self occlusions are to be ignored, in most tracking applications, target shapes are seldom known in advance. Hence, opting for a pre-determined scaling parameter is infeasible.

A common method for choosing the transformation parameter s_k is the Greedy Association Model (GAM), which does not need the distribution of transformation parameter s_k as a prior [82, 102]. However, GAM attempts to find the distribution of s_k by seeking the best source of measurements on the boundary of the extended target, which are closest to the measurements using a chosen metric. Widely used metrics include Mahalanobis distance [103], radial distance [78] and signed distance [104]. We illustrate this in Figure 3.14, where the GAM method is used to estimate the transformation parameter s.

However, when using RPs, and thus RP shape function Φ, the value of the half-space itself is a quantifiable metric for finding the best source corresponding to a given measurement. This eliminates the need for any additional metrics. More specifically, each particular value of the parameter s_k is similar to a distinct association hypothesis where a correct observation $\mathbf{z}$ is associated to a source $\tilde{\mathbf{z}}$ on the boundary of an RP. Furthermore, assuming that the sensor covariance noise is isotropic, the source, which
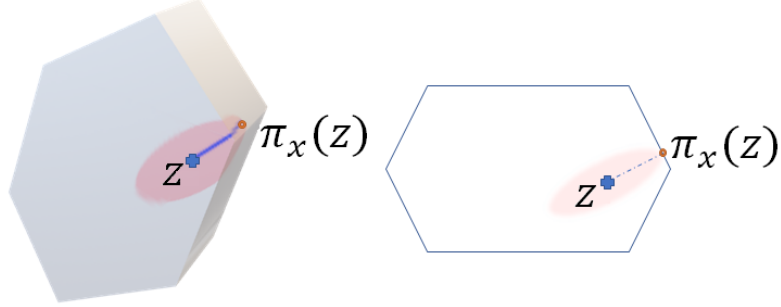
Figure 3.14: Finding the most likely source on the contour for a given observation.

can be traced back to a measurement $\mathbf{z}$, is the one that maximizes the following likelihood function:

$$\tilde{\mathbf{z}}_{\mathbf{x},s'} = \arg \max_{\tilde{\mathbf{z}}_{\mathbf{x},s} \in \tilde{Z}_x} \mathcal{N}(\mathbf{z} - \tilde{\mathbf{z}}_{\mathbf{x},s}, C_w) \qquad (3.5.6)$$

where $\tilde{\mathbf{z}}_x$ represents all possible sources on the boundary of the object, and C_w is sensor noise. In reality, $\tilde{\mathbf{z}}_x$ is replaced by an analytic expression using the proposed RP implicit shape function introduced in (3.4.8). Furthermore, the spatial probability mass function of the scaling parameter s is modeled with the Dirac delta function, δ, as follows:

$$p(s) = \delta(s - s') \qquad (3.5.7)$$

where all probability is concentrated in value s' that is dependent to the observation $\mathbf{z}$.

The problem of finding the most probable half-space that is responsible for generating the measurement $\mathbf{z}$ can be formulated as the following optimization problem,

$$
\mathbf{w}'_s = \begin{cases} \min_{\mathbf{w}_i \in \{\text{Observable half spaces}\}} & \frac{1+\tanh(\mathbf{z},\mathbf{w}_i)}{2} - 0.5, & \text{if } \Phi(\mathbf{z}) > 0.5 \\ \min_{\mathbf{w}_i \in \{\text{Observable half spaces}\}} & \frac{1+\tanh(\mathbf{z},\mathbf{w}_i)}{2}, & \text{if } \Phi(\mathbf{z}) < 0.5 \end{cases} \tag{3.5.8}
$$

where the observable half-spaces are chosen according to a threshold, which is applied to the auxiliary P_d of half-spaces. In cases where (3.5.8) leads to multiple minima, one is chosen randomly.

3.6   Filtering

3.6.1   Initialization

As mentioned in Section 3.4, the RP shape function is less sensitive to the number of half-spaces defining the shape of the extended target. That is, the number of hyperbolic-tangent components, N, becomes application-specific. From our simulations in Section 3.8, it is observed that, to obtain a smooth boundary in a two-dimensional domain, $N \approx 8$. In order to achieve a similar smoothness in a three-dimensional domain, $N \approx 2d_2$, where d_2 is the number of half-spaces in $\mathbb{R}^2$.

In the absence of any prior knowledge about the shape of the extended targets, the initial shape is assumed be either a disk or sphere, both with a fixed radius r, in two-dimensional and three-dimensional spaces. Let

$$
\pi_i = \frac{\pi i}{N}
$$

and

$$\pi_i^1 = \frac{\pi(i-1)}{N}$$

The parametric representations of weights of half-spaces for these initial shapes are given by [97]

$$W_D = \begin{cases} \cos(2\pi_i), & k = 0 \\ \sin(2\pi_i), & k = 1 \\ -\left[r + x\cos(2\pi_i^1) + y\sin(2\pi_i^1)\right]. & k = 2 \end{cases} \qquad (3.6.1)$$

and

$$W_D = \begin{cases} \sin(\pi_i)\cos(2\pi_i), & k = 0 \\ \sin(\pi_i)\sin(2\pi_i), & k = 1 \\ \cos(\pi_i), & k = 2 \\ -\left[r + x\sin(\pi_j^1)\cos(2\pi_i^1) + y\sin(\pi_i^1)\sin(2\pi_i^1) + z\cos(\pi_i^1)\right]. & k = 3 \end{cases} \qquad (3.6.2)$$

where x, y and z are the coordinates of the centroid of the extended target and $i \in 0, \ldots, N-1$ is representing the index of the half spaces. However, this is method is applicable only if r is known a priori. When this is not the case, the corresponding r value can be initialized using the RHM method. More specifically, the RHM algorithm with circle or sphere shapes is used in the first few iterations of the loop to obtain an

initial estimation for r.

3.6.2   Prediction

The prediction step is performed using the model that describes the evolution of the target over time, similar to (3.4.12) in Section 3.4.4. In our work, in line with the literature, we will be using an identity matrix to model the evolution of the target extension over time [80]. This will result in the following prediction step in the proposed algorithm.

$$\mathbf{x}_k = F_k.\mathbf{x}_{k-1} + \mathbf{v}_k \tag{3.6.3}$$

where $F_k = [\bar{F}_k, I]$ is the model transition matrix, with I being the identity matrix, and $\mathbf{v}_k$ is the Gaussian process noise.

3.6.3   Gating

The gating step is crucial for handling measurement origin uncertainty [105], particularly in the context of multitarget tracking applications. The gating is performed before the update step, and handles the measurement origin uncertainty by differentiating possible false alarms from possible target-originated observations, by processing each measurement individually. In our case, this is performed using the following predictive likelihood function

$$p(\mathbf{z}_k|\mathbf{z}_{1:k-1}) = \mathcal{N}(\hat{\mathbf{z}}_{k|k-1}, S_k) \tag{3.6.4}$$

where S_k is the measurement prediction covariance given by

$$S_k = H_k P_{k|k-1} H_k^T + R_k \tag{3.6.5}$$

where H_k is the Jacobian of the pseudo-measurement model defined in Section 3.4.5. More specifically, each measurement is verified whether it is originating from inside or outside the gating region. This is achieved using the residual distance between the predicted and observed values. This is usually denoted as $\tilde{\mathbf{z}} = |\hat{\mathbf{z}}_k - \mathbf{z}_k|$. Thus,

$$\tilde{\mathbf{z}}^T S^{-1} \tilde{\mathbf{z}} \gtrless g^2 \tag{3.6.6}$$

where g is the gating threshold. In practice, g relies on a user-defined parameter ϵ, where $0 < \epsilon \leq 1$. As $\epsilon \to 1$, the acceptance rate of measurements increases. Since the measurements are assumed to follow a Gaussian distribution, the left side quadratic form in (3.6.6) has a Chi-Square distribution [106] as follows:

$$g^2 \ \sim \ \mathcal{X}_n^2 \tag{3.6.7a}$$

$$p(g^2) \ = \ \frac{1}{2^{\frac{n}{2}} \Gamma(\frac{n}{2}) g^{n-2} \exp^{\frac{g^2}{2}}} \tag{3.6.7b}$$

where n is the degrees of freedom, and in our case, $n = 1$. Thus, the value of the gating threshold can be chosen using the inverse of the cumulative Chi-distribution with a unit degree of freedom [105].

3.6.4 Update

For recursively updating the posterior distribution using Bayes' theorem, all measurements $\{\mathbf{z}_{k,l}\}_{l=1}^{n}$ up-to time step k are augmented as follows:

$$\mathbf{z}_k = [\mathbf{z}_{k,1}, \ldots, \mathbf{z}_{k,l}]^T \tag{3.6.8}$$

By assuming that all measurements are independent, and assuming that scaling parameter s_k and measurement noise are uncorrelated, the likelihood function $p(\mathbf{z}_k | \hat{X}_k)$ can be constructed as follows:

$$p(\mathbf{z}_k | \mathbf{x}_k) = \prod_{l=1}^{n} p(\mathbf{z}_{k,l} | \mathbf{x}_k) \tag{3.6.9}$$

Furthermore, as the measurement noise model is additive, the likelihood value for each single measurement $\mathbf{z}_{k,l}$ can be expressed as follows:

$$p(\mathbf{z}_{k,l} | \mathbf{x}_k) = \int \underbrace{p(\mathbf{z}_{k,l} | \mathbf{z})}_{\text{sensor model}} \cdot \underbrace{p(\mathbf{z} | \mathbf{x}_k)}_{\text{source model}} \, dz \tag{3.6.10}$$

By assuming the scaling factor s as an iterator, which iterates through all possible

actual source of measurements, $\tilde{\mathbf{z}}_{x,s}$, and by assuming that the noise model follows the Gaussian distribution, (3.6.10) can be transformed into

$$p(\mathbf{z}_{k,l}|\mathbf{x}_k, s_k) = \int \mathcal{N}(\mathbf{z}_{k,l} - \mathbf{z}, \Sigma_\omega).\delta(\mathbf{z} - \tilde{\mathbf{z}}_{\mathbf{x}_k,s})dz \qquad (3.6.11)$$

where δ is the Dirac delta function and Σ_ω is the covariance of the sensor noise. Thus, each s represents an association hypothesis. There are at least two different options to handle these different hypotheses. One approach is to fuse all of these different hypotheses into a single best hypothesis. The other approach is to retain all of the hypotheses along with a set of relevant likelihoods and posteriors, and compute the final hypothesis similar to the Joint Probabilistic Data Association (JPDA) method [105]. However, in this work, to reduce the computational complexity, we use the former approach, which is outlined in Section 3.5.1. Once the products of likelihoods are found, using the Bayes' formula, the posterior distribution can be expressed as follows:

$$p(\mathbf{x}_k|\mathbf{z}_k) \propto \underbrace{p(\mathbf{z}_k|\hat{\mathbf{x}}_k)}_{\text{Likelihood}} \cdot \underbrace{p(\mathbf{x}_{k-1})}_{\text{Prior}}. \qquad (3.6.12)$$

The best estimate of the extended target state can then be established by maximizing the posterior distribution in (3.6.12). For simplicity, we use the extended Kalman Filter (EKF), which is an approximate maximum a posteriori (MAP) algorithm for nonlinear estimation problems. Better alternatives to nonlinear filtering, such as the unscented Kalman filter (UKF) [107] and the particle filter (PF) [108],

can be used as well.

3.6.5 Extended Kalman Filter

One of the key benefits of modeling extended targets by the RP shape function, which conforms to the pseudo-measurement model in (3.4.16), is that it is differentiable everywhere. Hence, the first order Extended Kalman Filter (EKF) [109], which approximates the nonlinear measurement model with its first order Taylor series expansion, can be used for the update step. The derivative of the non-linear pseudo-measurement model can be calculated analytically (See Appendix 3.10.1). Hence, the updated values of state and covariance matrices for the proposed RP-EKF algorithm can be computed as follows:

$$\frac{dh(\mathbf{x}_k)}{d\mathbf{x}_k} = H(\mathbf{x}_k), \tag{3.6.13a}$$

$$\mathcal{K} = P_{k|k-1} \times H_k \times S_k^{-1}, \tag{3.6.13b}$$

$$\mathbf{x}_k = \mathbf{x}_{k|k-1} + \mathcal{K} \times \text{Weight}^T \times (\mathbf{z}_k - s_k \times 0.5), \tag{3.6.13c}$$

$$P_{k|k} = P_{k|k-1} - \text{Weight}^T \times \mathcal{K} \times S_k \times \mathcal{K}^T. \tag{3.6.13d}$$

where Weight^T is the vector containing the thresholded auxiliary P_d values for each half-space in the augmented state vector. The value of s_k for each measurement is computed based on the GAM concept, as outlined in Section 3.5.1, and as follows:

$$s_k = \frac{\frac{1 + \tanh(\mathbf{z}_{k,l}, \mathbf{w}_s')}{2}}{0.5}. \tag{3.6.14}$$
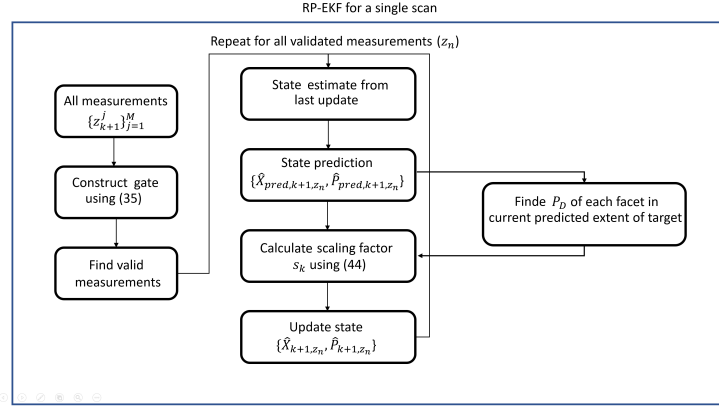
Figure 3.15: Block diagram for the proposed RP-EKF.

where $\mathbf{w}_s'$ is as defined in (3.5.8).

3.7 Posterior Cramér-Rao Lower Bound

The posterior Cramér-Rao lower bound (PCRLB) [69] is a standard method for quantifying a performance bound on the mean square error (MSE) for nonlinear filtering problems. As such, a derivation of PCRLB is required for our proposed approach. In deriving the PCRLB, which is defined as the inverse of the posterior Fisher information matrix (PFIM), it is worth stating the following two crucial assumptions:

- The shape and kinematic parts of the target state are independent of each other; and

- The evolution of the shape and kinematic parts over time are also independent of each other.

That is, the measurements at time k from an extended target provides additional information about the target. Furthermore, given a ground truth state $\mathbf{x}_{k+1}$ and its

corresponding unbiased estimated state $\hat{\mathbf{x}}_{k+1}$, which is conditioned upon the measurement set $\mathbf{z}_{1:k+1}$, the PFIM, denoted by $J(k+1)$, is a lower bound for the covariance matrix P_{k+1} [69]. Thus,

$$P_{k+1} = E\{(\hat{X}_{k+1} - X_{k+1})(\hat{X}_{k+1} - X_{k+1})^T\} \geq J^{-1}(k+1) \qquad (3.7.1)$$

However, the PFIM can be computed using the Riccati-like recursion [69] as follows:

$$J(k+1) = (F_k \times J_k^{-1} \times F_k^T + Q_k)^{-1} + J_{z,k+1} \qquad (3.7.2)$$

where the initial value $J_0 = P_0^{-1}$, and the measurement contribution is denoted by $J_{\mathbf{z},k+1}$. For scenarios without any clutter,

$$J_{\mathbf{z},k+1} = \text{Weight}_k^T \times H_k \times R_k \times H_k^T \qquad (3.7.3)$$

where H is the Jacobian of the pseudo-measurement, and Weight_k is the vector containing the thresholded auxiliary information P_d, for each facets of the target extent state at time k. In the presence of clutter, the loss of information extracted from observations due to measurement origin uncertainty is to be accounted for. This is usually achieved by scaling (3.7.3) by q, where $0 \leq q \leq 1$, to signify the information reduction.

3.8   Results

3.8.1   Overview of Evaluation

To effectively asses the performance of the proposed RP-EKF algorithm, we consider the shape estimations under the following conditions:

1. different noise conditions

2. in a two-dimensional space, and

3. in a three-dimensional space.

Each of these conditions stresses on different aspects of the proposed approach. More specifically, (1) assesses the capability of the proposed approach to handle different noise conditions, and (2) and (3) evaluate the capability of the proposed filter to handle the shape estimation problem in two- and three-dimensional spaces, respectively. In addition to the evaluation under different conditions, we also summarize the computational performance at the end of this section. To compare the performance of different algorithms in their capability to estimate target shapes, we use two different metrics. One is the intersection-over-union (IOU) measure [73], which has been used in state-of-the-art ET tracking algorithms to compare the accuracy of shape estimates. The IOU metric defined for the interval of $\in [0, 1]$ and is defined as follows:

$$\text{IOU}(\hat{R}, R^{\text{G}}) = \frac{A(\hat{R} \cap R^{\text{G}})}{A(\hat{R} \cup R^{\text{G}})} \qquad (3.8.1)$$

where $A(\bullet)$ represents the area, $\hat{R}$ is the region that is covered by the estimated shape

and R^{G} is the region covered by the true shape. An IOU value closer to one shows better performance in shape estimation.

The second metric is a custom, polytope-aware distance metric $\mathfrak{D}(.,.)$, which is defined as the *difference between the normalized weights of the half-spaces constructing true and estimated polytopes.* Here, the polytopes are representing the extended target. Thus,

$$\mathfrak{D}(\hat{W}, \check{W}) = \sum_{i=1}^{n} \sum_{D=0}^{d} \left(\left| \frac{\hat{w}_{iD} - \check{w}_{iD}}{\bar{w}_D} \right| \right). \tag{3.8.2}$$

where $\hat{w}$, $\check{w}$, and $\bar{w}$ are the estimated, ground truth and the average weights among all half-spaces building the required RP. It is worth noting that this metric is, in fact, based on the notion of overlapping regions, similar to the IOU metric [80] or area error [11]. However, a metric that helps identifying the subtle cases of visually different shapes with overlapping regions is more desirable. On this note, this metric results in a very high-score, effectively differentiating the visually non-identical shapes using to the discriminant half-spaces [97]. Furthermore, we use this metric in conjunction with two state-of-the-art algorithms, one for two-dimensional and one for three-dimensional spatial domains, to benchmark the performance of the proposed approach. We describe these baseline algorithms in the following subsection, prior to the actual evaluations.

3.8.2   Baseline Algorithms

As stated above, in the absence of any universal algorithm that can work across multiple spatial dimensions, we rely on two different baseline algorithms, namely, the

LS-RHM [80] and Gaussian processes [110], for evaluating the proposed approach for the two- and three-dimensional cases, respectively.

Baseline algorithm for two-dimensional cases: LS-RHM

The LS-RHM is a Bayesian algorithm capable of tracking two-dimensional non-convex extended and filled targets [80]. The original LS-RHM method relies on a sequence of Cartesian points in a two-dimensional space for representing a polygon $S(\mathbf{x}_k)$, with the Mahalanobis distance as its shape function. The signed distance function of the LS-RHM method is given by

$$\Phi^\pi(\mathbf{x}_k, \mathbf{z}) = \begin{cases} d(\mathbf{x}_k, \mathbf{z}), & \text{if } \mathbf{z} \in S(\mathbf{x}_k) \\ -d(\mathbf{x}_k, \mathbf{z}). & \text{otherwise} \end{cases} \tag{3.8.3}$$

where d is the minimum Mahalanobis distance between the polygon and an observation $\mathbf{z}$, and defined as

$$d(\mathbf{x}_k, \mathbf{z}) = \min \sqrt{(\mathbf{z} - \mathbf{z}^\pi)\Sigma^{-1}(\mathbf{z} - \mathbf{z}^\pi)} \tag{3.8.4}$$

where point $\mathbf{z}^\pi$ is the closest point from the measurement $\mathbf{z}$ to the polygon and Σ is measurement noise covariance. Furthermore, the implicit measurement model expressed by

$$h(s_k, \mathbf{y}_k, \mathbf{x}_k, \omega_k) = s_k . \Phi^{max}(\mathbf{x}_k) - \Phi^b(\mathbf{x}_k, \mathbf{y}_k - \omega_k). \tag{3.8.5}$$

is used update the state information in linear filters that use the LS-RHM method. However, the LS-RHM method cannot easily be generalized and extended to three-dimensional targets.

Baseline algorithm for three-dimensional cases: Gaussian Process

In [110], an approach for expressing a three-dimensional extended target as a radial function is presented. This radial function can be, in fact, modeled by a Gaussian Process. More specifically, the relationship between the extent of the surface and the radial function is modeled by the following Gaussian Process:

$$\boldsymbol{f}(\gamma) = \mathcal{GP}(0, \kappa(\gamma, \gamma') + \sigma_r^2). \tag{3.8.6}$$

where $\boldsymbol{f}(\gamma)$ is the radial function with an input γ that captures both the azimuth and elevation of the target, and κ is a covariance function of the GP. Here, the covariance function is often replaced by the Squared Exponential function. Thus,

$$\kappa(\gamma, \gamma') = \sigma_f^2 \exp(-\frac{||\gamma - \gamma'||^2}{2l^2}). \tag{3.8.7}$$

where l represents the length scale, and σ_f^2 represents the prior variance. The augmented state space model $\mathbf{x}_k$ is then updated through an EKF filter, as follows:

$$\mathbf{x}_{k+1} = F_k \mathbf{x}_k + \omega_k, \tag{3.8.8a}$$

$$m_{k,l} = h_k(\mathbf{x}_k) + \mathbf{e}_k$$

$$= c_k + \mathbf{p}_{k,l}(c_k)[H^{\boldsymbol{f}}(\gamma_{k,l}(c_k, q_k))\boldsymbol{f}_k + e^{\boldsymbol{f}}_{k,l}] + \bar{e}_{k,l}, \tag{3.8.8b}$$

$$\mathbf{p}_{k,l}(c_k) = \frac{m_{k,l} - c_k}{||m_{k,l} - c_k||}, \tag{3.8.8c}$$

$$H^{\boldsymbol{f}}(\gamma_{k,l}(c_k, q_k)) = K(\gamma_{k,l}(c_k, q_k), \gamma^{\boldsymbol{f}})[K(\gamma^{\boldsymbol{f}}, \gamma^{\boldsymbol{f}})]^{-1}. \tag{3.8.8d}$$

where c_k and q_k are representing centre and heading angle of target and

$$e^{f}_{k,l} \sim \mathcal{N}(\mathbf{0}, R^{\boldsymbol{f}}_{k,l}), \tag{3.8.9a}$$

$$\bar{e}_{k,l} \sim \mathcal{N}(\mathbf{0}, R), \tag{3.8.9b}$$

$$\mathbf{x}_0 \sim \mathcal{N}(\mu_0, P_0). \tag{3.8.9c}$$

3.8.3   Tolerance to Noise Conditions

The fidelity of the proposed algorithm to different noise conditions can be evaluated in a number of different ways. However, to simplify the analysis, we limit the scope of the evaluation to three immobile, static targets, in a two-dimensional space, namely Z-, H-, and L-shaped, non-convex objects from [80]. We then corrupt the measurements with three different sensor noise levels, namely low ($\sigma = 10^{-4}$m), medium ($\sigma = 0.1$m) and high ($\sigma = 1.5$m). We then estimate the shape using the proposed approach

under these noise conditions, before evaluating them against the ground truth using the distance metric in (3.8.2), and we report the average metrics over 50 Monte Carlo runs. To benchmark the relative performance, we use the LS-RHM method outlined in [80], which considers the same shapes in their evaluation. Since the objective here is to assess the noise tolerance capability of the filter in estimating the extended state, the occlusion assumption is relaxed, and thus, it is assumed that all parts of the objects are observable and can generate observations.

One of the main advantages of the proposed shape function is that the value of the shape parameter is bound within the interval of $[0, 1]$. In contrast, in the case of LS-RHM, an extra step is required to find the maximum possible value of the shape function. The values of the proposed RP shape function, for all three shapes, are shown in Figure (3.16).
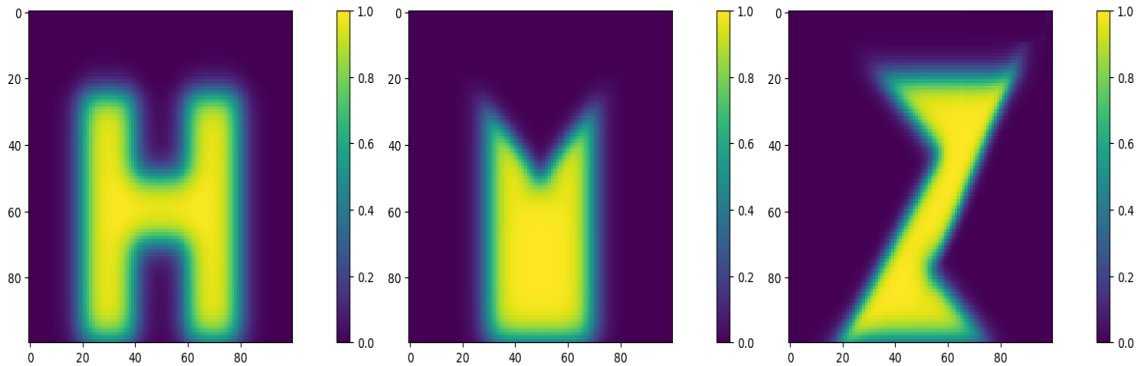
Figure 3.16: The values of shape function for the H-, M- and Z-shaped non-convex two-dimensional targets.

We show the overall performance in Figures 3.17 and 3.18, and in Table 3.6. Figure 3.17 shows the said non-convex shapes under three different noise conditions while Figure 3.18 shows the average distance errors in estimating different shapes under different noise conditions, compared against the LS-RHM method. Finally,

Table 3.6: Average steady state distance (m) between true and estimated shapes of targets under different noise conditions, namely low ($\sigma = 10^{-4}$m), medium ($\sigma = 0.1$m), and high ($\sigma = 1.5$m).

Filter / Target Shape	Low Noise			Medium Noise			High Noise		
	Z	H	M	Z	H	M	Z	H	M
LS-RHM	1.15	2.18	1.02	2.40	2.62	1.42	4.60	3.50	1.75
RP-EKF	1.16	2.18	1.15	2.43	2.56	1.33	3.72	2.89	1.54

Table 3.7: Average steady state IOU between true and estimated shapes of targets under different noise conditions, namely low ($\sigma = 10^{-4}m$), medium ($\sigma = 0.1m$), and high ($\sigma = 1.5m$).

Filter / Target Shape	Low Noise			Medium Noise			High Noise		
	Z	H	M	Z	H	M	Z	H	M
LS-RHM	0.92	0.89	0.94	0.79	0.84	0.89	0.63	0.66	0.71
RP-EKF	0.93	0.91	0.93	0.83	0.86	0.89	0.68	0.71	0.72

Table 3.6 summarizes the overall performance.

Finally, Table 3.7 summarizes the overall performance of both filters in terms of IOU metric.

A number of conclusions can be drawn from these results:

- as the measurement noise level increases, the number of observations required for the true shape estimation increases;

- the mean absolute difference of the steady state errors between the two filters increases with noise levels; and

- the proposed filter can reconstruct the true shape with fewer measurements when compared against the LS-RHM.

Overall, the proposed filter is more tolerant to different noise conditions.
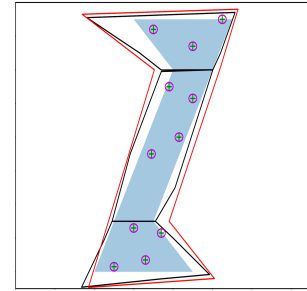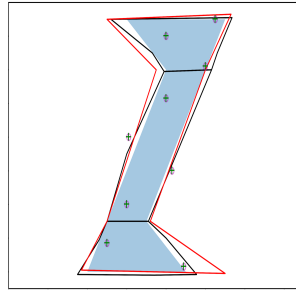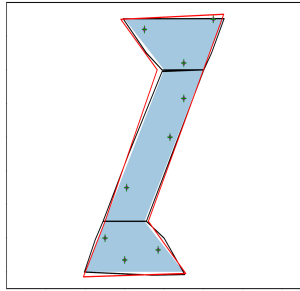
(a) Z-Shape (Low Noise)   (b) Z-Shape (Medium Noise)   (c) Z-Shape (High Noise)
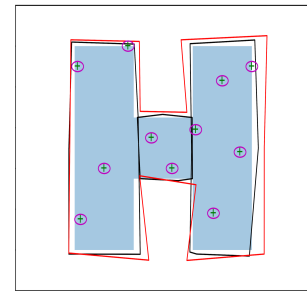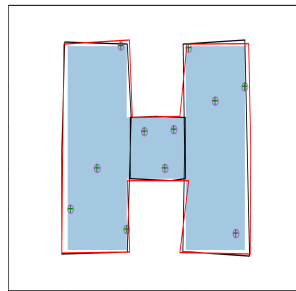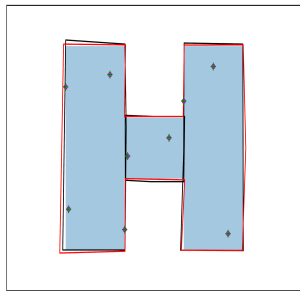
(d) H-Shape (Low Noise)   (e) H-Shape (Medium Noise)   (f) H-Shape (High Noise)
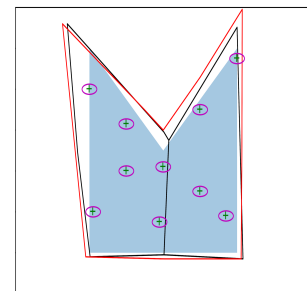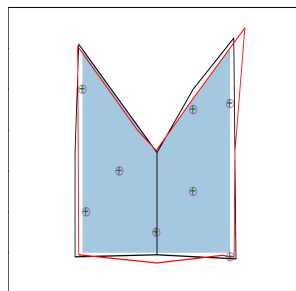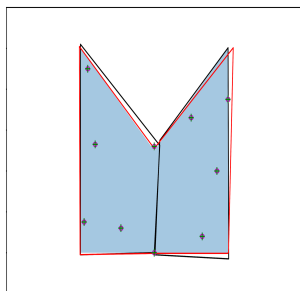
(g) M-Shape (Low Noise)   (h) M-Shape (Medium Noise)   (i) M-Shape (High Noise)

Figure 3.17: An example set of runs, with three different noise conditions, for three non-convex-shaped objects. The sample measurements and corresponding uncertainty in noise are shown with a + and ∘ symbols.

(a) Z-Shape (Low Noise)   (b) Z-Shape (Medium Noise)   (c) Z-Shape (High Noise)

(d) H-Shape (Low Noise)   (e) H-Shape (Medium Noise)   (f) H-Shape (High Noise)

(g) M-Shape (Low Noise)   (h) M-Shape (Medium Noise)   (i) M-Shape (High Noise)
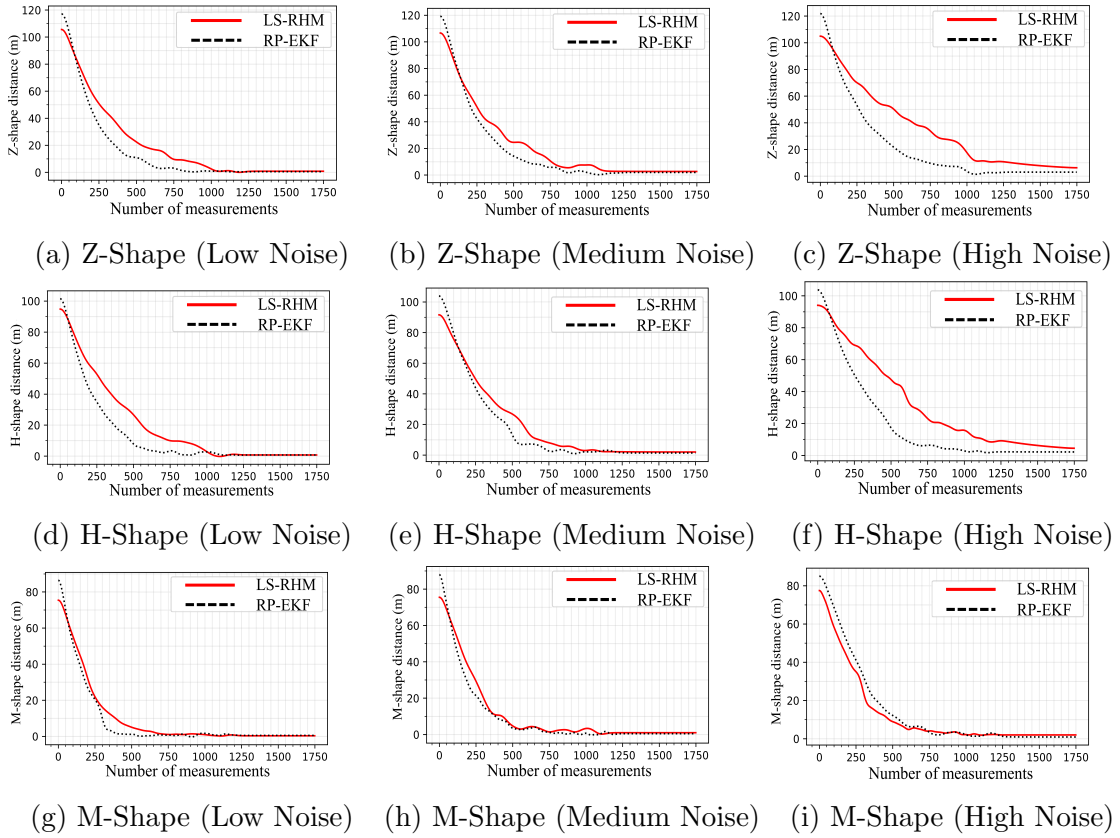
Figure 3.18: The average distance errors in estimating target shapes by the proposed approach vs. LS-RHM method under different noise conditions.

3.8.4   Evaluation for the Two-Dimensional Scenario

For this case, we use a convex-shaped extended target. The targets are fully-filled, and only a single target is used to assess the performance. Other relevant data for the simulation, which are common to these cases, are as follows:

- The initial kinematic state of the target for this case is given by $\mathbf{x}_0 = \mathbf{x}_0^{True} + \tilde{\mathbf{x}}_0$ where $\tilde{\mathbf{x}}_0 \sim \mathcal{N}(\mathbf{0}, P_0)$.

- The process noise covariance matrices for the position, velocity, and heading angle have the standard deviation of $\sigma_q = 0.1$m, $\sigma_{q^v} = 0$, and $\sigma_{q^\psi} = 0.001$rad/s,

respectively.

- The standard deviation of the sensor noise covariance matrix, however, is set to $\sigma_z = 0.001$m.

- The motion model is such that the initial dynamic state $\mathbf{x}_0$ is $x_0 = \{0, 1, 0, 0\}$ following a constant velocity motion model from time 0 to 150s, followed by a constant turn model from 150 to 250s, followed by another constant velocity model from 250 to 400s and finally another constant turn model. The extent of the target is modeled similar to a car in a two-dimensional space.

For the convex-shaped extended target, we use an object mimicking the shape of a car in a two-dimensional space. During the simulations, the position of the sensor platform and the center of the target are used to detect the visible facets of the object, and thus to generate the measurements. Here, the LS-RHM method is initialized by a polygon. In contrast, the proposed RP-EKF method is initialized using three convex polytopes, assuming that the number of convex polytopes required for estimating the true shape is known in advance. The center location of the three convex polygons are chosen to cover all parts of the target. We show the results of the shape and trajectory estimations for the target in Figures 3.19 and 3.20.

First, from Figures 3.19a and 3.19b, it can be seen that the proposed RP-EKF can estimate the shape better than the LS-RHM method. In addition to this, in Figure 3.20, we use the PCRLB to show the lower bound of the RMSE. From these results, it can be observed that the proposed RP-EKF method outperforms the LS-RHM method with its steady state RMSE being significantly closer to the PCRLB. This shows that accounting for occlusion can significantly improve the performance.

(a) Results of LS-RHM   (b) Results of the RP-EKF
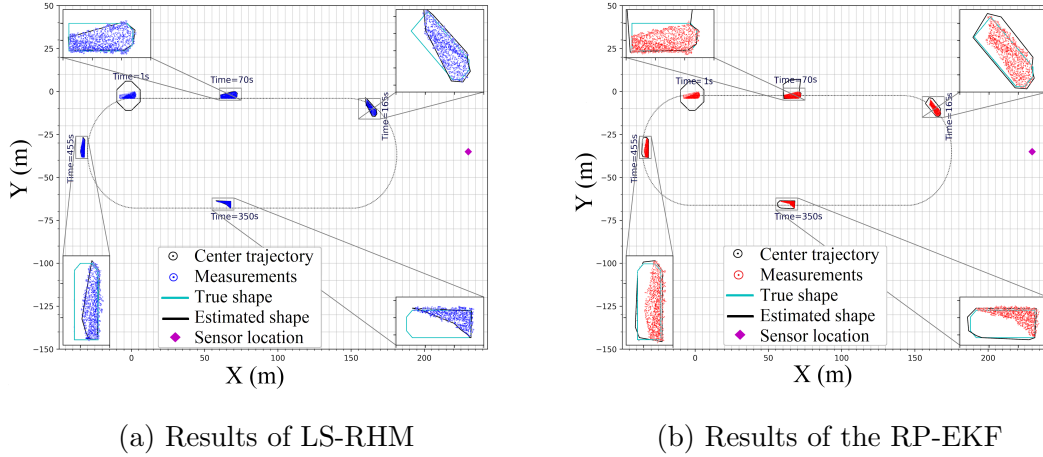
Figure 3.19: The state and shape estimates for the two-dimensional scenario for a convex target (a) LS-RHM (b) proposed RP-EKF.

The average values of the IOU metric for the convex shape by the LS-RHM and proposed RP-EKF filters are summarized in Table 3.8.

Table 3.8: Average IOU values for the convex target for the two-dimensional case.

Filter / Target Shape	Convex
LS-RHM	0.45
RP-EKF	0.79

3.8.5 Evaluation for the Three-Dimensional Scenario

For this case, only one type of extended target is considered, namely, the convex-shaped extended target. Although it is possible to assume a filled interior, and to generate corresponding measurements, we will only be using a self-occluding boundary-frame model in our study here for two reasons. One is that the probability of the sensor receiving measurements from the interior of a three-dimensional object is considerably low [110]. The other is that there is no baseline algorithm against which the

(a) PCRLB and RMSE

(b) Polytope distance $\mathfrak{D}$
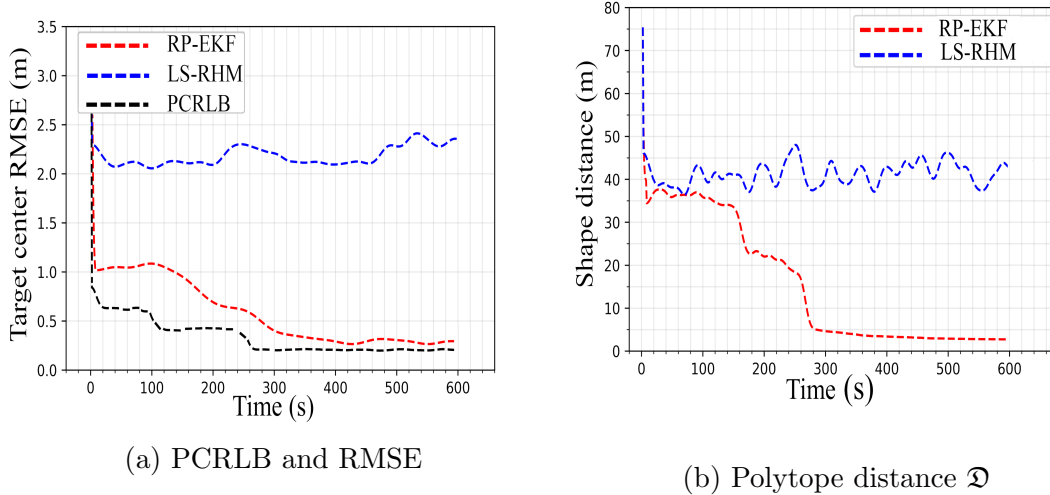
Figure 3.20: The RMSE and polytope distance metrics compared for the two-dimensional scenario for a convex target (a) RMSE (b) distance metric $\mathfrak{D}$.

proposed approach can be benchmarked. More specifically, we will be using the algorithm outlined in [110] as our baseline version. Other relevant data for the simulation are the same as in the two-dimensional case, except that the initial kinematic state of the target $\mathbf{x}_0$ is $\mathbf{x}_0 = \mathbf{x}_0^{True} + \tilde{\mathbf{x}}_0$, where $\tilde{\mathbf{x}}_0 \sim \mathcal{N}(\mathbf{0}, P_0)$. A cubic object with the length 3m is simulated. The motion model has a number of stages. First, it travels with a constant velocity motion model with $v = 12$m/s from time 0 to 150s. This is then followed by a constant turn model with small rotation rate of 0.0305rad/s from time 150 to 250s. This is then followed by a constant velocity model of $v = 12$m/s during time interval 250 to 400s before switching back to the constant turn model from time 450 to 550s.

Since the baseline recursive Gaussian Process algorithm supports observations only from the contour of the target, all measurements are generated from the contour as stated above. This results in replacing the s parameter with a constant value of

$s = 1$. The initial shape estimate is an arbitrary icosahedron, with the assumption of non-zero, non-negative height, matching the geometric properties of road or terrain. We show the resulting performance in Figures 3.21 and 3.22.

(a)   (b)
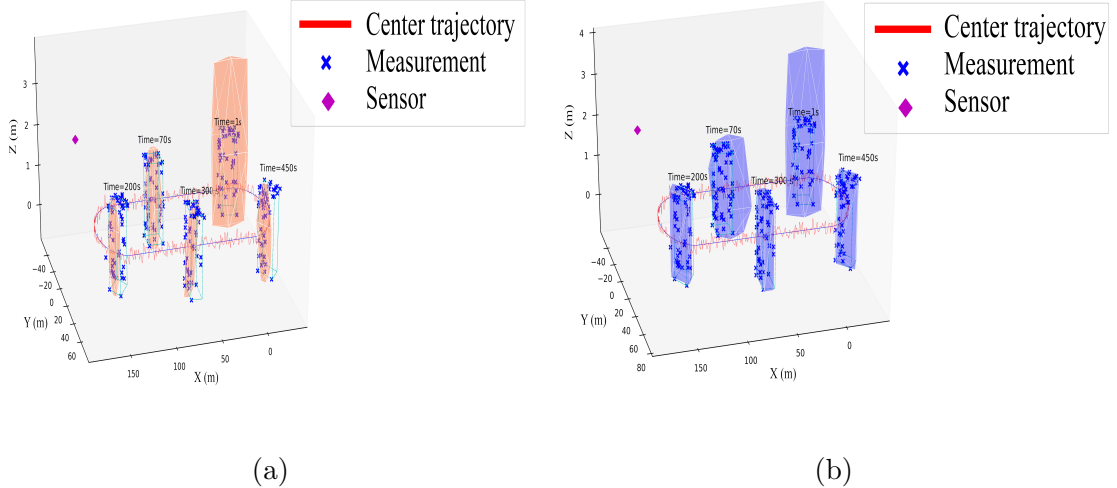
Figure 3.21: The state and shape estimates compared for the three-dimensional scenario for a convex target (a) GP (b) proposed RP-EKF.

In Figure, 3.21, the extended target is in cyan. Measurements are uniformly generated from the surface of the target along with a Gaussian noise term with covariance of $R = 0.1I$. Furthermore, the number of measurements are modeled with a Poisson distribution and the hyper-parameters of recursive Gaussian Process are set to be $\sigma_f = 2$, $\sigma_r = 2$ and $l = \pi/4$ following the original method in [110]. The results show the effectiveness of the proposed RP-EKF algorithm in estimating the true shape of the target.

3.8.6   Computational Complexity

We assess the computational complexity of the different algorithms using their runtime, more specifically the elapsed CPU time of the kernels of concern. All versions
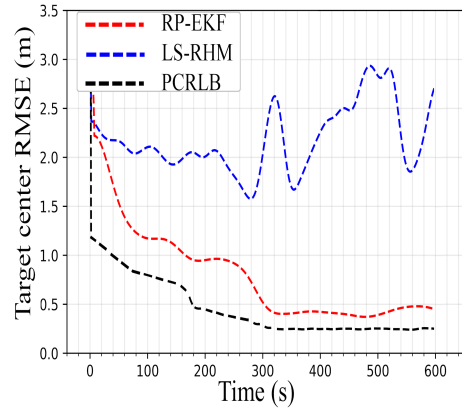
Figure 3.22: The RMSE values compared for the three-dimensional scenario for a convex target for the GP and RP-EKF algorithms.

Table 3.9: Average CPU runtimes for processing a single measurement and for single scan of the RP-EKF, GP and LS-RHM algorithms.

Filter	Single measurement (/s)	One scan (/s)
LS-RHM (2D)	0.82	12.09
RP-EKF (2D)	0.03	6.43
GP (3D)	1.35	9.42
RP-EKF (3D)	0.65	3.94

were implemented in Python (Version 3.6), and they were run on a system (Operating System: Windows 10, Build 19041.329, Processor: Intel i7-7th Gen, Number of Cores: 4, RAM: 16 GB at 2666 MHz) with 50 Monte Carlo runs. We report the average runtimes for the proposed RP-EKF, recursive GP and the LS-RHM algorithms are shown in Table 3.9. From these results, it can be seen that the proposed RP-EKF is computationally much cheaper than the baseline versions.

3.9 Conclusions

In this paper, we presented a novel extended target tracking algorithm using Random Polytopes shape function in a recursive Bayesian framework. The proposed method is capable of providing better shape estimation along with kinematic estimations for filled extended targets in two- and three-dimensional tracking scenarios. In particular, special attention was given to self-occlusions to handle practical applications, which is one of major limitations of existing algorithms in literature.

The utility of the proposed approach was evaluated under different conditions, such as varying measurement/sensor noise conditions, and two- and three-dimensional tracking scenarios, using a number of realistic simulations. The performance of the proposed algorithm, both shape and kinematic estimations, when compared against respective state-of-the-art methods, is significantly better. The proposed method can be extended further through a number of avenues. Examples include, but are not limited to, utilizing data association models such as JPDA or PMHT for handling heavy clutters, and handling inter-target occlusions caused by other objects. These extensions are likely to benefit a number of challenging real world applications.

3.10   Appendices

3.10.1   Jacobian Of Pseudo-Measurement Equation

The First derivative of the hyperbolic tangent function, which we will need for deriving the gradient of Random Polytope shape function, is derived below.

$$
\begin{aligned}
\frac{\partial}{\partial \aleph} \tanh(\aleph) &= \frac{\partial}{\partial \aleph} \frac{\sinh(\aleph)}{\cosh(\aleph)} = \frac{\frac{\partial}{\partial \aleph}\sinh(\aleph) \times \cosh(\aleph) - \frac{\partial}{\partial \aleph}\cosh(\aleph) \times \sinh(\aleph)}{\cosh^2(\aleph)} \\
&= \frac{\cosh^2(\aleph) - \sinh^2(\aleph)}{\cosh^2(\aleph)} = 1 - \frac{\sinh^2(\aleph)}{\cosh^2(\aleph)} \\
&= 1 - \tanh^2(\aleph) = 1 - \left(\frac{\exp(2\aleph) - 1}{\exp(2\aleph) + 1}\right)^2
\end{aligned}
\tag{3.10.1}
$$

The general case of RP shape function that represents objects with multiple convex Random Polytope is given by

$$
\frac{\partial}{\partial w} \Phi(n) = \prod_{k \neq i}(1 - \phi_k(n)) \frac{\partial \phi(n)}{\partial w}
\tag{3.10.2}
$$

where $\frac{\partial \phi(n)}{\partial w}$ is the derivative of a convex Polytope function that can be derived from (3.10.1) as follows:

$$
\frac{\partial \phi(n)}{\partial w} = 1 - \tanh^2(\aleph) x_D
\tag{3.10.3}
$$

Chapter 4

Tracking Multiple Extended Targets In Occlusion Using Splines and Set-Membership Uncertainty Models

4.1   Abstract

This paper presents a new technique for tracking a time-varying number of Extended Targets (ET) in the presence of occlusion and data association ambiguity. Extended target is an object whose size is not negligible compared to the sensor resolution, resulting in multiple measurements from different parts of the object in a sensor scan. A group of closely-spaced targets may also appear as a single extended target. In extended target tracking applications, such as autonomous vehicles and surveillance

systems, the shape of a target should be estimated along with its kinematic state. To achieve this, the technique proposed in this paper models the shape of a target using B-spline curves. Self and mutual occlusion of targets can significantly degrade the performance of existing ET tracking algorithms. To overcome this limitation, in this work, we first define the observable parts of an ET in the B-spline representation to handle self occlusion. Then, to deal with mutual occlusion, the probability of detection (p_D) of each ET is modeled by an adaptive state-dependent model, which is then used in the update equations of the conventional Gaussian mixture probability hypothesis density (GM-PHD) filter that normally uses a constant state-independent p_D. The proposed approach enables the track to prolong even under adverse conditions caused by occlusion. In addition, the proposed algorithm uses set-membership uncertainty models to bound the association and target shape uncertainties due to occlusion using virtual (negative) observations. The capabilities of the proposed algorithm are demonstrated on simulated vehicle-tracking scenarios and the advantages are quantified against the state-of-the-art ET tracking algorithms.

4.2   List of Notations

A list of used notations and their explanations are listed below.

$x_{k,n}$ Target n state at time k

$\mathcal{X}_k$ Multiple target state at time k

v_k Intensities associated with target multiple target posterior density

Z_k Multiple target measurement at time k

ζ Target previous state

$v_{S,k|k-1(x)}$ Predicted intensity of surviving targets

$v_{B,k|k-1(x)}$ Predicted intensity of spawned targets

$\gamma_k(x)$ New born targets intensity

$v_{k|k-1}(x)$ Predicted intensities

v_k Updated posterior density

$v_{D,k}(\bullet; z)$ Detection intensity for each measurement z

X_k Augmented target state

x_k^c Kinematic target state

x_k^s Extent target state

γ_k Rate parameter of number of measurements

p_i ith control point of B-spline curve

$\mathbb{P}_k$ Set of all control points of B-spline curve

p_D Adaptive state-dependant probability of detection

ϕ Maximum bearing angle of arc spanned by ET object

ϕ' Minimum bearing angle of arc spanned by ET object

R Range of an ET object center from sensor

$p_{D,max}$ Maximum possible probability of detection

p_O Probability of occlusion of an ET object

z_k Actual measurement at time k

z_k^- Negative (virtual) measurement at time k

W Cluster of measurements (cell)

$S(k)$ Vector of sensor location

4.3   Introduction

One major assumption in traditional multiple target tracking (MTT) applications is that each target can generate at most one measurement per scan. As a result, most tracking algorithms can only handle point targets [7]. However, in short-range applications such as autonomous vehicles [11, 111] or long-range applications such as airborne surveillance using high-resolution sensors [112] this assumption may be violated, necessitating extended target (ET) tracking methods [16]. Even with point targets, the true origin of a received measurement is unknown to the tracker, which is known as the data association problem [105]. That is, measurements may arise from true targets or from clutter (false alarm), and hence, the tracker needs to use appropriate data association methods to resolve the origin of each measurement [21]. With ET, the data association problem is exacerbated further due to multiple measurements in a scan per target.

In general, there are three main approaches to address the ET tracking problem. The first approach tries to group the observations that may have originated from each ET object and summarizes the group of observations as a joint measurement such as

the center of the cluster. After summarizing all observations as a single measurement (e.g., weighted centroid), the ET tracking problem is handled using conventional point target tracking algorithms [2, 113]. The major drawback of this approach is that it removes some of the crucial information about targets such as its shape and orientation through the grouping process. The second approach tries to model measurements in a sensor's field-of-view using some spatial distribution such as the Poison point process [4]. In this approach, the mean number of measurements generated from ET objects and the spatial extent (or shape) of ET objects are assumed to be constant and known to the filter. However, both parameters may change and depend on the geometry between the ET objects and the sensor. The third approach tries to model the shape of an ET object using geometric shapes such as sticks, rectangles and ellipses, and then estimates the shape parameters by constructing feasible measurement-to-source assignment hypotheses and their probabilities [7, 10, 11]. With computational load, accuracy and shape description in mind, the algorithm proposed in this paper relies on shape-modeling.

To model the target shape as an ellipse using a positive semi-definite matrix, the random matrices (RM) method is proposed in [7]. Extensions of the RM method to the multiple target case are proposed in [32] based on the Gaussian mixture probability hypothesis density (GM-PHD) filter, in [114] based on the probabilistic multiple hypothesis tracking (PMHT) algorithm, and in [115] based on the generalized labelled multi-Bernoulli (GLMB) filter.

Another shape-based ET tracking method uses the recursive Gaussian process (GP) approach in [11]. A box particle filter method is introduced in [116] and a GP

convolutional particle filter is proposed in [117] to extend the algorithm to the multitarget case. The random hyper surface model (RHM) proposed in [10] is another shape-based ET tracking algorithm that is expanded to handle multiple target scenarios in [118] and [119]. In addition to the above techniques, to model the extent or shape of an ET object, B-spline curves are used as shape descriptors in [16] and [15].

In these existing methods to track multiple ET objects, the critical and real-world problem of occlusion of targets is neglected, which may significantly degrade tracking performance in scenarios with self and mutual occlusions. Self-occlusion happens when a part of an object blocks another part on the same object [19]. Mutual-occlusion happens when one object blocks another [20]. Not accounting for the reduction in the detection probability due to self- or mutual-occlusion may result in track breakage or even track loss, resulting in track segmentation. Thus, it is necessity to account for the variation in the detection probability and its dependence on self- or mutual-occlusion to ensure accurate tracking. This challenge provides the motivation for this paper.

In this paper, we model the extent of an ET object using B-spline curves [16]. With B-splines as the shape descriptor, we define an adaptive probability of detection (p_D) model to calculate the p_D of an object in each scan according to its location in the sensor's field-of-view (FoV). Then, we use a time- and target-dependent variable p_D in the update equation of the GM-PHD filter instead of a fixed value.

Furthermore, the modeling of the extent of an ET object using B-splines has another advantage in that the self-occlusion of a target can also be modeled naturally. A B-spline curve can be controlled locally using only a few control points. Although

local shape control may help the filtering algorithm to obtain accurate shape esti-mates, it may also lead to catastrophic errors in estimation. For example, if the filter assumes that all the control points representing the shape of an ET are observable to the sensor in every scan, which may not be true in practice, the quality of state and shape estimates may suffer. To mitigate this, in this work, we define a weight parameter that can be seen as an auxiliary p_D for each control point in the B-spline representation of an ET object to improve the shape estimates, which in turn can lead to better state estimates.

Although an adaptive state-dependent p_D in the update stage of the filter may help mitigate the track segmentation caused by mutual occlusion, the accuracy of the state estimates of an occluded target may still suffer due to the p_D being almost zero and the filter continuing with prediction and skipping the update step. To alleviate this problem, we propose to take advantage of set-membership uncertainty models [120], which are useful in modeling bounded uncertainties whereas the stochastic un-certainties are useful in modeling unbounded noises such as false alarm rates [121]. With occluded targets, the occlusion phenomenon can be modeled as a bounded un-certainty with an unknown distribution [122]. That is, even the lack of ET detections contains some useful information about the object's centroid and extent state that may improve the corresponding estimates. The set-membership uncertainty bounds, in case of an occluded ET object, are the constraints that are imposed on the angu-lar and range span of the occluded ET object by the current sensor-to-group-target geometry. Since modelling these constraints directly is rather difficult, they are im-posed using virtual or negative observations similar to the concept introduced in [111]. Thus, the region where an occluded target may exist is bounded by these negative

measurements [121].

To model the number of measurements generated from each ET object, several methods are proposed in the literature. For example, in [4] and [3], the number of measurements are modelled using an non-homogeneous Poisson distribution with an unknown rate parameter to be estimated form measurements. These algorithms may not work well in the case of closely spaced targets. In [16], the measurement rate is modelled using a Poisson mixture and the Poisson mixture variational Bayesian (PMVB) method is proposed to simultaneously estimate the measurement rate parameter along with kinematic and extent states. However, this method is computationally expensive. In the method proposed in our paper, we use a recursive Bayesian approach with exponential forgetting factor to estimate the gamma distributed measurement rate parameter [123]. The gamma distribution is chosen to model the measurement rate parameter since it is assumed that the number of measurements generated from each ET object follows a Poisson distribution and the gamma distribution is the conjugate prior of the Poisson distribution [124].

To summarize, the main contribution of this works are as follows:

1. Using a B-spline representation of an ET, we define the observable parts of an object and use that knowledge to improve the ET-GM-PHD filter [28] to handle the problem of self-occlusion that is inevitable in real-world scenarios. The proposed algorithm is called the spline gamma Gaussian mixture probability hypothesis density (S-GGM-PHD) filter.

2. Using the Gaussian components in the ET-GM-PHD filter, the proposed method finds an adaptive state-dependent p_D for each ET target to identify and account for partially or fully occluded targets in the sensor's FoV. This reduces the track

segmentation caused by the occlusion due to dynamic or static obstacles.

3. The proposed method exploits the concept of set-membership uncertainties to find the bounded region where the occluded target may be present and uses this as negative information to obtain more accurate state and shape estimates of an ET object.

4. The performance improvements by the proposed algorithm are quantified on realistically simulated scenarios with self- and mutual-occlusions.

The rest of the paper is organized as follows. In Section 4.4, the standard GM-PHD filter is reviewed and the ET tracking problem is discussed. The use of B-splines to model the shape of an ET object is also discussed in Section 4.5.1. In Section 4.6, the adaptive state-dependent p_D and B-spline control point weights are derived. The derivation of the negative information used in the update stage of proposed filter is described in Section 4.7. The proposed S-GGM-PHD filter with adaptive p_D is presented in Section 4.8. Finally, simulation results along with comparison discussions are presented in Section 4.9. Conclusions are discussed in Section 4.10.

4.4   Background

This Section reviews the formulation of the multiple target tracking problem using the random finite set (RFS) theory using the standard Gaussian mixture probability hypothesis density (GM-PHD) filter. Then, the preprocessing of measurement sets from extended targets to make the observations ready for use within the standard GM-PHD filter framework is discussed. The augmented extended target state that is used in the proposed GM-PHD filter extension is also defined in this Section.

4.4.1   Standard GM-PHD Filter

In a Bayesian RFS setting, both the target states and the measurements are modelled using respective RFS. The PHD filter is an effective approximation to mitigate the computational intractability of the optimal multitarget tracking problem. In this paper, the same assumptions as in the original PHD framework [125], except for the one about a constant state-independent p_D are made. The following two equations represent the predicted and the posterior density steps of the RFS MTT algorithm based on the Chapman-Kolmogorov equation and Bayes' theorem [125]:

$$p_{k|k-1}(\mathcal{X}_k|Z_{1:k-1}) = \int f_{k|k-1}(\mathcal{X}_k|\mathcal{X}_{k-1})p_{k-1}(\mathcal{X}|Z_{1:k-1})dx \qquad (4.4.1)$$

$$p_k(\mathcal{X}_k|Z_{1:k}) = \frac{g_k(Z_k|\mathcal{X}_k)p_{k|k-1}(\mathcal{X}_k|Z_{1:k-1})}{\int g_k(Z_k|\mathcal{X}_k)p_{k|k-1}(\mathcal{X}_k|Z_{1:k-1})dx} \qquad (4.4.2)$$

where $f_{k|k-1}(\mathcal{X}_k|\mathcal{X}_{k-1})$ and $g_k(Z_k|\mathcal{X}_k)$ are multiple-target transition density and multiple-target likelihood, respectively, for an appropriate reference measure μ_s that belongs to all feasible subsets of X.

The above prediction and posterior recursion equations will become the following intensities in the PHD framework:

$$v_{k|k-1}(x) = \int p_{S,k}(\zeta)f_{k|k-1}(x|\zeta)v_{k-1}(\zeta)d\zeta + \int \beta_{k|k-1}(x|\zeta)v_{k-1}(\zeta)d\zeta + \gamma_k(x) \quad (4.4.3)$$

$$v_k(x) = [1 - p_{D,k}(x)]v_{k|k-1}(x) + \sum_{z\in Z_k} \frac{p_{D,k}(x)g_k(z|x)v_{k|k-1}(x)}{\kappa_k(z) + \int p_{D,k}(\zeta)g_k(z|\zeta)v_{k|k-1}(\zeta)} \qquad (4.4.4)$$

where $p_{S,k}$ is the probability that the target exists at time k given its previous state ζ, γ_k is the intensity of target birth, $\beta_{k|k-1}$ is the intensity of target spawning, κ_k is the intensity of clutter and $p_{D,k}(x)$ is the target probability of detection of given

state x. The detailed derivations of the prediction and update steps of the GM-PHD filter using only the positive information based on the measurements actually received by the sensor with state-independent constant probability of detection $(p_{D,k})$ and probability of survival $(p_{S,k})$ are given in [125]. The GM-PHD filter is a closed-form approximate solution to the PHD recursion with linear-Gaussian assumptions [125]. In the GM-PHD filter, each target follows a linear-Gaussian dynamical model and the sensor model is also linear and Gaussian, i.e.,

$$f(x_k|x_{k-1}) = \mathcal{N}(x_k; F_{k-1}x_{k-1}, Q_{k-1}) \tag{4.4.5}$$

$$g(z_k|x_k) = \mathcal{N}(z_k; H_k x_k, R_k) \tag{4.4.6}$$

where F_{k-1} and H_k are state transition and measurement matrices, respectively, while Q_k and R_k are the process noise and measurement noise covariance matrices, respectively. It is also assumed that the birth, spawning and posterior intensities at time t_k are Gaussian mixtures of the form

$$v_{\bullet,k} = \sum_{i=1}^{J_{\bullet,k}} \omega_{\bullet,k}^{(i)} \mathcal{N}(x; m_{\bullet,k}^{(i)}, P_{\bullet,k}^{(i)}) \tag{4.4.7}$$

where $\bullet$ denotes a place holder for operands, and can be replaced by γ to determine birth intensity, β for spawning intensity and S for surviving from the last time step and J, ω, m and P are model parameters to determine the shape of the PHD intensities

Thus, the following two equations show how the Gaussian components from time $k-1$ are propagated to the next time step k, replacing the prediction and posterior

recursions in (4.4.3) and (4.4.4), respectively:

$$v_{k|k-1}(x) = v_{S,k|k-1}(x) + v_{\beta,k|k-1}(x) + v_{\gamma,k}(x) \qquad (4.4.8)$$

$$v_k(x) = [1 - p_{D,k}(X)]v_{k|k-1}(x) + \sum_{z \in Z_k} v_{D,k}(x;z) \qquad (4.4.9)$$

where

$$v_{D,k}(x;z) = \sum_{j=1}^{J_{k|k-1}} \omega_k^{(j)} \mathcal{N}(x; m_{k|k}^{(j)}(z), P_{k|k}^{(j)}) \qquad (4.4.10)$$

with $\omega_k^{(j)}$ being weight of the jth Gaussian component. Note that the summation in the posterior calculation step in (4.4.9) is over all possible partitions of measurements and not over individual observations. More details are given in Section 4.8 and a brief review of existing techniques for generating the partitions for ET applications is given in the following sub-section.

4.4.2   Observation Set Partitioning

In point target tracking algorithms, the update step is carried out using each (actually received) measurement. On the other hand, in ET tracking algorithms, the update step often uses each partition (cluster) of measurements formed using a measurement partitioning algorithm [16]. Measurements in each partition are assumed to have originated from the same source, which can be either an ET or a false alarm.

Various techniques for measurement partitioning, such as distance partitioning and sub-partitioning [28], K-means clustering [126], and predictive partitioning and Expectation-Maximization (EM) [79], are discussed in the literature. Also, a method

to combine multiple partitioning techniques is proposed in [32] with improved results. In [127, 128], another algorithm for partitioning the measurements and generating clusters is proposed based on the Variational Bayesian technique [64]. Due to the computation efficiency of the VB technique, it is used in the partitioning stage of the multiple ET tracking algorithm proposed in this paper (S-GGM-PHD). More details on the VB technique can be found in [128].

4.4.3   Augmented Target State

The joint single target state X contains the kinematic state, extent state and the measurement rate, given by

$$X_k = [x_k^c, x_k^s, \gamma_k]^T \tag{4.4.11}$$

where the kinematic state (x_k^c) contains the Cartesian position, velocity and possibly the acceleration of the ET object's centroid, extent state (x_k^s) contains the parameters describing spatial shape of the ET and γ_k is the rate parameter of the Poisson distribution modeling the number of measurements generated by each ET.

In this work, the extent state x_k^s consists of the Cartesian coordinates (and their derivatives) of the closed B-spline curve control points representing the shape of the ET object. The extent state is further discussed in the following Section.

4.5   Extended Target Tracking Problem Formulation

In this Section, we present a brief review of the B-splines used to model the extent of the ET object in this paper. Then, the models for ET state dynamics and measurement generation used in this paper are presented.

4.5.1   Modeling Of Extended Target Extent Using B-splines

The B-spline [129] is a generalization of Bèzier curves [130] to represent arbitrary curves. The local controllability of a curve represented by B-splines with control points makes B-splines amenable for use in the Bayesian estimation of the shape of an ET and the continuity of B-splines makes it applicable in continuous state estimation [131]. The B-spline of curve $C(x)$ is defined as a linear combination of control points $\mathbb{P} = \{p_1, p_2, \ldots, p_N\}$ and basis functions $B_{i,\rho,\mathbf{t}}(x)$ given by

$$C(x) = \Sigma_{i=1}^{N} p_i B_{i,\rho,\mathbf{t}}(x) \tag{4.5.1}$$

where $\mathbf{t} = \{t_1, \ldots, t_\tau\}$ is the knot vector that consists of ascending real valued numbers and N is the total number of control points. The local controllability of a B-spline is the result of the basis functions being non-zero just for a short interval always being smaller than $[t_1, t_\tau]$. The order of a B-spline is defined using the length of the knot vector and the number of control points according to

$$\rho = \tau - N \tag{4.5.2}$$

128

and the degree of the corresponding B-spline is $\rho - 1$.

The basis function of a B-spline curve is defined using the Cox–de Boor recursive formula [132]. Thus, a basis function of order ρ, which can also be seen as a polynomial of degree $\rho - 1$, is defined by

$$B_{i,1}(x) = \begin{cases} 1, & \text{if } t_i \leq x \leq t_{i+1} \\ 0, & \text{otherwise} \end{cases} \tag{4.5.3}$$

$$B_{i,\rho}(x) = \frac{x - t_i}{t_{i+\rho+1} - t_i} B_{i,\rho-1}(x) + \frac{t_{i+\rho} - s}{t_{i+\rho} - t_{i+1}} B_{i+1,\rho-1}(x) \tag{4.5.4}$$

with t_i being the knot element.

There are three types of knot vectors that can be used in B-spline curve representation [133]. The first one is the uniform knot vector, which contains elements with equal distance from each other, $t_{i+1} - t_i = \text{constant}, \forall i$. The second is the open uniform knot vector, which contains elements that are uniformly distributed from each end. The third is the non-uniform knot vector, which contains elements in ascending order with no special constraint. To define a closed curve using B-splines, we need to design a uniform knot and repeat the first ρ control points from the beginning of the knot to the end of the control points sequence.

To generalize a unidimensional B-spline like the one defined in (4.5.1) to a multidimensional one, we need to define the B-spline subspace for each dimension and multiply them together, which is called the tensor product spline construction as

represented by

$$C(x_1, \ldots, x_m) = \Sigma_{i_1}^{N} \ldots \Sigma_{i_m}^{N} p_{i,\ldots,i_m} B_{i_1,\rho_1,\mathbf{t}_1}(x_1) \ldots B_{i_m,\rho_m,\mathbf{t}_m}(x_m) \qquad (4.5.5)$$

In the proposed method, the control points of a closed B-spline curve replaces the extent (or shape) state of an ET object similar to the one proposed in [16]. However, the proposed technique for updating the extent state is novel and mitigates the challenges posed by self- and mutual-occlusion by exploiting the local controllability of B-splines.

4.5.2 Extended Target Kinematic and Measurement Model

The target kinematic state x_k^c is evolving in time according to the following dynamic motion model:

$$x_k^c = F x_{k-1}^c + w_k$$

$$w_k \sim \mathcal{N}(0, Q_k) \qquad (4.5.6)$$

with the covariance matrix Q_k of the dynamic process noise vector w_k and state transition matrix F being respectively given by

$$Q_{k+1} = \begin{bmatrix} \sigma_Q^2 \frac{T^4}{4} & \sigma_Q^2 \frac{T^3}{2} \\ \sigma_Q^2 \frac{T^3}{2} & \sigma_Q^2 T^2 \end{bmatrix} \otimes \Sigma_k \qquad (4.5.7)$$

$$F = \begin{bmatrix} 1 & T \\ 0 & 1 \end{bmatrix} \otimes I_d \qquad (4.5.8)$$

130

where σ_Q is the process noise standard deviation, T is the sampling interval of the sensor and the symbol $\otimes$ represents the Kronecker product [54] and I_d is the identity matrix with appropriate dimensions. Thus, the process noise covariance is proportional to the covariance of the extent state Σ_k.

Following the random matrices (RM) algorithm [7], the actual measurements are modelled as the measurement of the ET object's centroid corrupted by a measurement error that is proportional to the ET object extent. An ET object that is present within the sensor's FoV and is not blocked will generate multiple measurements $\mathbf{z}_k = \{z_k^1, \ldots, z_k^{|W|}\}$ according to the following model

$$z_k^i = Hx_k^c + v_k, \ i \in \{1, |W|\}$$

$$v_k \sim \mathcal{N}(0, \Sigma_k) \tag{4.5.9}$$

where H is the measurement generation model and the covariance matrix Σ_k of the measurement noise vector v_k is the covariance of control points $\mathbb{P}_k$ that define the extent state of the ET object. The measurement covariance is calculated at each time step according to the sample covariance of the received measurements as defined in (4.8.12d).

4.6   Adaptive Detection Probability Model

As discussed in Section 4.4.1 the conventional GM-PHD assumes that both the probability of survival $p_{S,k}$ and the probability of detection $p_{D,k}$ are fixed and independent of target state, although a generalization to handle certain classes of state dependent $p_{D,k}$ and $p_{S,k}$ is proposed in [125]. However, $p_{D,k}$ is assumed to be constant and

state-independent in most PHD filter related works, specifically those for ET tracking [134, 135, 136].

Time-varying and state-dependent $p_{D,k}$ using GM-PHD for point target applications can be found in the literature. In [137], a GM-CPHD filter with time-varying adaptive $p_{S,k}$ is proposed based on terrain data to handle the possibility that a target may leave the surveillance region. A GM-PHD filter with a variable $p_{D,k}$ for tracking targets in a radar's Doppler blind zone is proposed in [138]. A GM-PHD filter capable of estimating the $p_{D,k}$ using the amplitude information by augmenting the target kinematic state with amplitude state is proposed in [139].

In this Section, we discuss how to use the B-spline concept, which is used to model the ET extent and target position, to address the occlusion problem. For a point on an object to be observable by the sensor, the line-of-sight between the sensor and that point on the target should be clear and not blocked either by a different object or some other part of the same object. To address the self-occlusion problem, the local-controllability of B-splines can be used. Although B-splines is used as the shape descriptor in [16] to model the extent of an ET, the assumption in [16] is that as long as the ET is within the sensor's FoV, it is fully observable. Thus, in real scenarios with self- and mutual-occlusion the performance of the algorithm in [16] suffers. In this paper, we propose an algorithm to alleviate the effects of occlusion.

First, we model the observable and unobservable parts of an object using the estimated B-splines at the current time handle self-occlusion. Figure 4.23 illustrates the observable and non-observable parts of a closed curve from the sensor's point of view.

It can be seen that an object's observable section can be represented with an arc
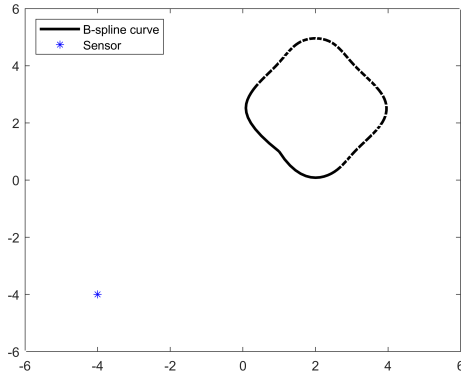
Figure 4.23: Observable (solid) and non-observable (dashed) parts of a closed curve from the sensor (blue star).

spanned by the ET object's minimum and maximum bearings. Each control point in the B-spline representation of a shape model is observable if it is on the same side of the line connecting the start and the end points of the arc spanned by the minimum and maximum bearings. Figure 4.24 illustrates the observable and occluded control points of the closed curve in Figure 4.23.
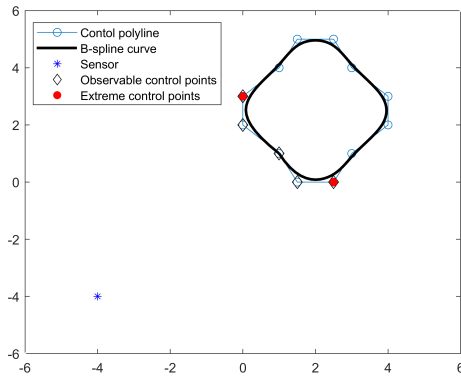
Figure 4.24: Observable and non-observable control points in the B-spline representation of a closed curve from a sensor. Control points corresponding to the minimum and maximum bearings are in red.

Thus, each control point located on the same side of the line connecting the two

control points corresponding to the minimum and the maximum bearings as the sensor will be observable with a p_D value of one. In contrast, the control points located on the opposite side of line will be unobservable with a p_D of zero. Time complexity of this algorithm to identify the observable and unobservable control points is $O(n)$ where n is the number of control points.

The proposed method can also associate a real value representing the probability of detection in the closed interval $[0, 1]$ to each control point instead of making a hard (binary) decision on being observable or occluded as described below. This approach has the advantage of considering the distance of each control point from the sensor in assigning the corresponding p_D.

If we assume that the line connecting the control points corresponding to the minimum and maximum observable bearings has a slope of m and a y-intercept of b, then the p_D of each control point $p_i = [x_{pi}, y_{pi}]^T$ of the ET can be approximated by following sigmoid function:

$$\text{Weight}_i = \sigma(p_i) = \frac{1}{1 + \exp(-mx_{pi} - y_{pi} + b)} \qquad (4.6.1)$$

with real values in the interval $[0, 1]$. This is based on the fact that the line connecting the two extreme bearings is a halfspace that can be approximated with the tangent hyperbolic function or the sigmoid function [140].

The values of the p_Ds of the control points defining the shape represented at Figure 4.24 are listed in Table 4.10. The final probability of detection of each control point in $\mathbb{P} = \{p_1, p_2, \ldots, p_N\}$ is calculated by multiplying the probability of detection of the

Table 4.10: Probability of detection of each control point

Control point	p_D	Control point	p_D
a	0.7	g	0.008
b	0.69	h	0.01
c	0.77	i	0.007
d	0.5	j	0.022
e	0.17	k	0.09
f	0.022	l	0.5

ET object's center and the corresponding p_D from Table 4.10. Then,

$$P_d^{(j)}(p_i) = \text{Weight}_i \times p_D^{(j)}(X_k), \ I \in 1, 2, \ldots, N \tag{4.6.2}$$

where $p_D^{(j)}(X_k)$ is the adaptive state-dependent probability of detection of the jth ET object and may be calculated as described below.

The calculated probability of detection for each control point in the extent state of the ET object can be used in a data association algorithm such as the joint probabilistic data association (JPDA) [105] algorithm or the game theoretic data association technique [141]. The equations in Section 4.8 are based on the JPDA algorithm.

The adaptive probability of detection of each B-spline gamma-Gaussian component used in the proposed PHD filter to mitigate the effects of mutual-occlusion is described next. First, the conditions for full and partial occlusion are investigated. A target is not observable by a sensor if there is another target at a range less than that of the first target within the bearing span of the first target. Figure 4.25 illustrates the case where target B is fully occluded by target A.

The necessary and sufficient conditions for target B to be fully occluded by target
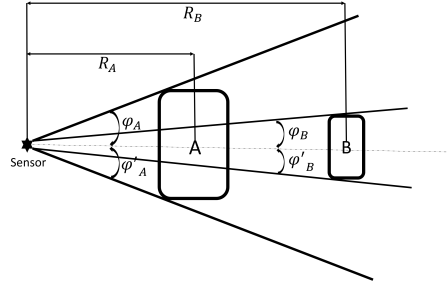
Figure 4.25: Full occlusion: Target A is occluding target B completely and sensor does not get any detection from target B.

A can be summarized as

$$\text{Bearing}^f_{A,B} = \{(\phi_A \geq \phi_B) \cap (\phi'_A \leq \phi'_B)\} \tag{4.6.3}$$

$$\text{Range}^f_{A,B} = \{R_A \leq R_B\} \tag{4.6.4}$$

where $R_\bullet$ is the range of an object form the sensor, $\phi_\bullet$ is the maximum bearing and $\phi'_\bullet$ is the minimum bearing angle corresponding to the target denoted by $\bullet$. In the above, $\text{Bearing}^f_{A,B}$ and $\text{Range}^f_{A,B}$ represent the bearing and the range value pairs of target A and target B, respectively, with full occlusion. The partial occlusion case needs different angle conditions than the ones in (4.6.3). Based on Figure 4.26, the following conditions for partial occlusion of target B by target A are derived:

$$\text{Bearing}^p_{A,B} = \{(\phi_A \geq \phi'_B) \cap (\phi_B \geq \phi'_A)\} \tag{4.6.5}$$

$$\text{Bearing}^p_{A,B} = \{(\phi'_A \geq \phi_B) \cap (\phi_B \geq \phi'_A)\} \tag{4.6.6}$$

where $\text{Bearing}^p_{A,B}$ means the bearing value pair of target A and target B with partial occlusion.

The cases in Figure 4.26(a) and 4.26(b) are represented by (4.6.5) and (4.6.6),

(a)   (b)   (c)
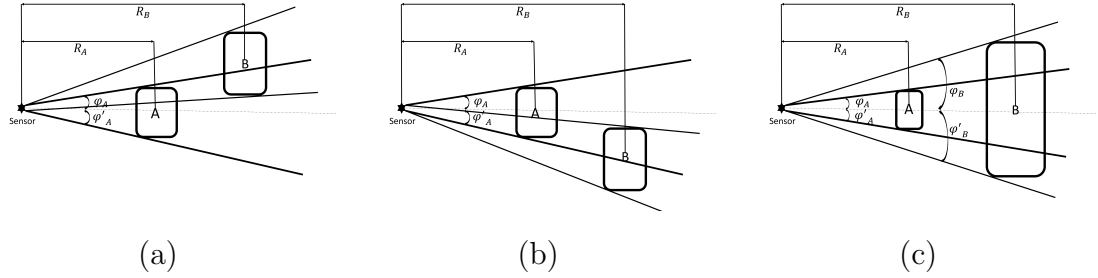
Figure 4.26: Three different geometries that may result in the partial occlusion of target B by target A.

respectively. Note that the case in Figure 4.26(c) in depicting partial occlusion is satisfied by the intersection of the conditions in (4.6.5) and (4.6.6).

The probability $p_D^{(i)}(X_k)$ calculated in (4.6.7) represents the probability of detection of the ith component with respect to all existing components and is given by

$$p_D^{(i)}(X_k) = \max\left((1 - \sum_{j=1}^{J_{k|k-1}} \omega_k^{(j)} p_O^{(i),(j)}) p_{D,\max}, 0\right) \qquad (4.6.7)$$

where $p_{D,max}$ is the maximum possible probability of detection, which is set to 0.99 in our work, $R^{(i)}$ and $R^{(j)}$ are the ranges to the the center of the ith and the jth components, respectively, and $p_O^{(i),(j)}$ is the probability of occlusion of the ith component by jth component.

The occlusion probability $p_O^{(i),(j)}$ is computed as

$$
p_O^{(i),(j)} = \begin{cases}
\Phi\left(\frac{\phi^{(j)}-\phi^{(i)}}{\sqrt{\sigma_\phi^{(i)}+\sigma_\phi^{(j)}}}\right) \times \Phi\left(\frac{\phi'^{(i)}-\phi'^{(j)}}{\sqrt{\sigma_{\phi'}^{(i)}+\sigma_{\phi'}^{(j)}}}\right) + \\
\Phi\left(\frac{\phi^{(j)}-\phi'^{(i)}}{\sqrt{\sigma_{\phi'}^{(i)}+\sigma_\phi^{(j)}}}\right) \times \Phi\left(\frac{\phi^{(i)}-\phi'^{(j)}}{\sqrt{\sigma_\phi^{(i)}+\sigma_{\phi'}^{(j)}}}\right) + \Phi\left(\frac{\phi'^{(j)}-\phi^{(i)}}{\sqrt{\sigma_\phi^{(i)}+\sigma_{\phi'}^{(j)}}}\right)\Big] \times \\
\Phi\left(\frac{\phi^{(i)}-\phi'^{(j)}}{\sqrt{\sigma_\phi^{(i)}+\sigma_{\phi'}^{(j)}}}\right) - \Phi\left(\frac{\phi^{(i)}-\phi^{(j)}}{\sqrt{\sigma_\phi^{(i)}+\sigma_\phi^{(j)}}}\right) \times \Phi\left(\frac{\phi'^{(j)}-\phi'^{(i)}}{\sqrt{\sigma_{\phi'}^{(i)}+\sigma_{\phi'}^{(j)}}}\right), & \text{if } R^{(j)} < R^{(i)} \\
0, & \text{if } R^{(j)} > R^{(i)}
\end{cases}
$$

$$(4.6.8)$$

where σ_ϕ and $\sigma_{\phi'}$ are the converted standard deviations of the two extreme control points and $\Phi(\bullet)$ is the cumulative distribution function of the Normal distribution [**?**].. More details on deriving (4.6.8) are given in Appendix 4.11.1.

Thus, the adaptive probability of detection for component $X_k^{(i)}$ given by $p_D^{(i)}$ is a function of each component weight $\omega_k^{(i)}$ in the proposed S-GGM-PHD algorithm, estimated control points $\mathbb{P}_k^{(i)}$ and the transformed uncertainties in these control points $\Sigma_k^{(i)}$. We analyse the occlusion at any time only for existing targets and newborn targets are assumed not to be occluded. This is not a major limitation since the occlusion conditions can be updated at subsequent times.

4.7   Set-Membership Uncertainty Model

When a target is under occlusion and its corresponding probability of detection is set to the minimum based on the adaptive model proposed in Section 4.6, the update step of the filter is skipped and the uncertainty in state estimation continues to grow. Although there is no direct measurement from the occluded ET, there are

some constraints on its state imposed by the sensor-to-target geometry and these constraints are modelled in this work using the set-membership concept with the help of virtual sensor evidence, also called negative measurements. The negative measurements limit the space that the occluded object can occupy in the sensor's FoV based on the current information about the geometry, i.e., the probability of an occluded target being in non-occluded space of the sensor's FoV is zero.

4.7.1 Virtual Measurements for Angular Constraints of an Occluded Target

As discussed above, the ET object's center in the kinematic state and control points in the extent state representing the shape of the occluded ET should fall between the minimum and the maximum bearings of the occluding target. The use of negative measurements directly to reduce the uncertainties in the occluded ET object's state estimate is challenging due to the nature of the negative measurement likelihood [111]. Thus, appropriate approximations are necessary to compute the likelihood and to derive the measurement model.

In this work, to bring the negative measurements and impose the constraints on the ET object state, a set of virtual measurements are generated to impose the same constraints and to make their likelihoods computable. Each positive (actual) measurement $z_{k,i}$, $i = 1, 2, \ldots, m_k$ in cluster W, which contains m_k measurements with its center being within a range less than the range of the occluded target, go through a post-processing algorithm and the corresponding bearings angles are calculated. Later, the minimum and the maximum angles are found and the angular extent of the ET object is defined using only the two measurements that correspond to the

minimum and the maximum angles, represented by $\bar{Z}_k = \{z_{k,\min}, z_{k,\max}\}$. Then, an imaginary line from the sensor to infinity in the following direction is drawn:

$$\hat{n}_{k,l}(j) = \frac{\bar{Z}_k(j) - S(k)}{||\bar{Z}_k(j) - S(k)||_2}, \ j = 1, 2 \tag{4.7.1}$$

where $S(k)$ is the sensor location in Cartesian coordinates at time k.

Then, each line is checked if it intersects with the surface of the occluded ET object. In case of intersection, each intersection point $I_{k,j}$ is described as a virtual measurement and is used to update the two extreme control points of the occluded ET object. The measurement model for these virtual observations can be described by

$$I_{k,j} = \mathfrak{h}(X) + \mathfrak{v}_{I_{k,j}} \tag{4.7.2}$$

where $\mathfrak{h}$ is a nonlinear function that computes the expected extreme control points of the object based on the sensor location and $\mathfrak{v}_{I_{k,j}}$ is a zero-mean Gaussian random noise with covariance $R_{I_{k,j}}$. This measurement model imposes the essential constraints on the ET object's state by assigning a low likelihood value to the states that do not satisfy the angular constraints. The nonlinear model in (4.7.2) is difficult to derive directly due to the arbitrary shapes represented by B-spline curve and therefore, it needs to be computed numerically as follows.

Using the sensor location $S(k)$ at the current time and the control points $x_k^s = \mathbb{P}(k)$ of the occluded object's B-spline curve, the corresponding angle to each control point

$p_i = [x_{pi}, y_{pi}]^T$ is calculated by

$$\text{Bearing}(p_i) = \tan^{-1}\left(\frac{y_{pi} - S_y(k)}{x_{pi} - S_x(k)}\right) \tag{4.7.3}$$

Among the computed angles, the minimum and the maximum angles are determined.

4.8   S-GGM-PHD Filter For Multiple Extended Target Tracking Application

In this section, the B-spline gamma Gaussian mixture PHD (S-GGM-PHD) filter with negative information for ET tracking will be derived in detail. The adaptive state-dependant probability of detection helps the S-GGM-PHD filter to track an occluded ET with a time-varying probability of detection. Exploiting the negative information will result in more accurate estimates of occluded targets' states.

To derive the prediction and update equations of the S-GGM-PHD filter with negative information for ET tracking, we model different parts of the augmented state X_k in (4.4.11) as follows:

- The kinematic state of the ET object center x_k^c is modelled by a Gaussian distribution.

- The extent state x_k^s is modelled by a spatial probability distribution that is derived from the control points of the B-spline curve representation of the object shape. Since the measurement model derived in Section 4.5.2 is Gaussian and the ET object control points are functions of this measurements, the extent state follows a Gaussian density function.

- The rate parameter γ_k is modelled by the gamma distribution. Because the gamma distribution is known to be the conjugate prior for the Poisson distribution [124], which models the number of measurements generated by each ET in each scan.

Therefore, for the ET state X_{k-1} the posterior distribution at time $k-1$ is defined according to the following density:

$$p(X_{k-1}|Z_{1:k-1}) = p(x_{k-1}^c|Z_{1:k-1}, x_{k-1}^s)p(x_{k-1}^s|Z_{1:k-1})p(\gamma_{k-1}|Z_{1:k-1}) \qquad (4.8.1)$$

The prediction step of the proposed S-GGM-PHD filter is derived by solving the (4.4.1) in Section 4.8.1 and the update step resulting from Bayes' theorem is given in Section 4.8.2 with consideration to an adaptive $p_{D,k}$ and negative observations.

4.8.1   Prediction Equations of the S-GGM-PHD Filter

Since an adaptive $p_{D,k}$ and the negative information will only affect the update step of the filter the prediction equations of the B-spline gamma Gaussian components in the S-GGM-PHD filter are similar to the ones proposed in previous works with no occlusion assumptions [28]. Based on (4.4.1) and the independence assumption among the kinematic state x_k^c and the extent state x_k^s, which is usually made in many ET tracking applications [7], the predicted density of the ET state at time k is given by

$$p(X_k|Z_{1:k-1}) = \int p(x_{k-1}^c|Z_{1:k-1}, x_{k-1}^s)f(x_k^c|x_{k-1}^c, x_k^s)dx_{k-1}^c \times$$

$$\int p(x_{k-1}^s|Z_{1:k-1})f(x_k^s|x_{k-1}^s)dx_{k-1}^s \times \int p(\gamma_{k-1}|Z_{1:k-1})f(\gamma_k|\gamma_{k-1})d\gamma_{k-1} \quad (4.8.2)$$

The first integral in (4.8.2) corresponds to the Gaussian kinematic state and has the following closed from solution for the linear-Gaussian dynamic motion model defined in Section 4.5.2:

$$\int \mathcal{N}(x_{k-1}^c; m_{k-1}, P_{k-1} + \Sigma_{k-1}) \mathcal{N}(x_k^c; F x_{k-1}^c, Q + \Sigma_{k-1}) dx_{k-1}^c$$
$$= \mathcal{N}(x_k^c; m_k, P_k + \Sigma_k) \tag{4.8.3}$$

where $m_k = F m_{k-1}$ is the predicted mean, $P_k = F P_{k-1} F^T + Q$ is the predicted covariance, F is state transition model, Q is the process noise covariance matrix and Σ_{k-1} represents the covariance of the control points in the extent state x_{k-1}^s.

The second term, which represents the extent state prediction, will be approximated with the following spatial distribution where each control point evolves in time with the same linear-Gaussian model as the kinematic state, x_k^c, except with a different noise covariance:

$$\int p(x_{k-1}^s | Z_{1:k-1}) \mathcal{N}(x_k^s; F \mathbb{P}_{k-1}, \Sigma_{k-1}) dx_{k-1}^s$$
$$\approx \mathbb{S}_k(x_k^s; \mathbb{P}_k) \tag{4.8.4}$$

where $\mathbb{S}_k$ is the B-spline curve determined by the predicted control points $\mathbb{P}_k = F\mathbb{P}_{k-1} + \omega_{k-1}$, F is the kinematic state transition model and ω_{k-1} is a white Gaussian noise with covariance Σ_{k-1}. The closed B-splines are constructed using the method described in Section 4.5.1.

The final integral, which models the density of the predicted rate parameter, is approximated by the exponential forgetting prediction method, similar to the approach

in [112], according to

$$\int \Gamma(\gamma_{k-1}, \alpha_{k-1}, \beta_{k-1}) f(\gamma_k | \gamma_{k-1}) d\gamma_{k-1}$$

$$\approx \Gamma(\gamma_k; \alpha_k, \beta_k) \tag{4.8.5}$$

where Γ represents that the predicted rate parameter γ_k has a gamma distribution function with $\alpha_k = \frac{\alpha_{k-1}}{u}$ and $\beta_k = \frac{\beta_{k-1}}{u}$ being its predicted shape and rate parameter, respectively, and u is a positive scaling factor (forgetting factor) that guaranties that the expectation of γ remains the same but its uncertainty increases. The effective length of the window for this prediction is $w_e = \frac{u}{u-1}$, which means that we only trust the information that are contained in the measurements from the last w_e time steps [143]. The expected value and the variance of the measurement rate are respectively given by

$$E[\gamma_k] = \frac{\alpha_k}{\beta_k}, \quad Var[\gamma_k] = \frac{\alpha_k}{\beta_k^2} \tag{4.8.6}$$

With the predicted densities of the kinematic, extent and measurement rate states calculated above, the final predicted intensity in the S-GGM-PHD framework (4.4.3) can be rewritten as

$$v_{k|k-1}(X) = \sum_{j=1}^{J_{k|k}} \omega_{k|k-1}^{(j)} \Gamma(\gamma_k, \alpha_k^{(j)}, \beta_k^{(j)}) \mathcal{N}(x_k^c; m_k^{(j)}, P_k^{(j)} + \Sigma_k^{(j)}) \mathbb{S}(x_k^s; \mathbb{P}_k) +$$

$$\sum_{j=1}^{J_{b,k}} \omega_{b,k}^{(j)} \Gamma(\gamma_k, \alpha_{b,k}^{(j)}, \beta_{b,k}^{(j)}) \mathcal{N}((x_k^c; m_{b,k}^{(j)}, P_{b,k}^{(j)} + \Sigma_k^{(j)}) \mathbb{S}(x_k^s; \mathbb{P}_{b,k}^{(j)}) \tag{4.8.7}$$

where the jth surviving component's weight is $\omega_{k|k-1}^{(j)} = p_s \times \omega_{k-1|k-1}^{(j)}$, p_s is the state-independent probability of survival and $\omega_{b,k}^{(j)}$ is the jth birth component weight.

Following previous works [16, 28] the spawning term in the predicted density is neglected since the partitioning algorithm used as a preprocessor to the update step can efficiently capture the spawning event in multiple-ET tracking scenarios.

4.8.2   Update Equations of S-GGM-PHD Filter

The correction step in the proposed S-GGM-PHD filter for a single ET object, with its predicted density (4.8.7) and receiving measurements set W at time k, is described in this Section. Prior to deriving the correction step of the proposed algorithm, the distribution to model the clutters in the surveillance region should be chosen. Here, the false alarm numbers are modelled using a Poisson distribution with application-dependant rate parameter λ_k and the false alarms are Uniformly positioned over the sensor's FoV. Thus, if the surveillance region has area or volume S, the mean number of false alarms is $\lambda_k \times S$ in each scan.

According to (4.4.4), the corrected S-GGM-PHD intensity of an ET object has the following form:

$$v_k(X_k) \triangleq \left((1 - p_D(X_k)) + p_D(X_k) \times \sum w_p \sum \frac{\gamma(X_k)^{|W|}}{dW} \prod \frac{g(W|X_k)}{\beta_{FA,k}} \right) v_{k|k-1}(X)$$

(4.8.8)

where $p_D(X_k)$ is the state-dependant probability of detection, $| \bullet |$ represents the counting operator, ω_p and dW are two coefficients defined for each partition p and cell W as defined in the following Section, $\gamma(X_k)$is a non-negative measurement rate, $\beta_{FA,k}$ is the intensity of clutter and $g_k(W|X_k)$ is the single ET likelihood. The single ET

likelihood term $g_k(W|X_k)$ used in (4.8.8) can be derived assuming the independence

of measurements in cell W, that is one of the cell in the partitions generated by VB

technique describe in Section 4.4.2, and using the measurement equation of the ET

defined in Section 4.5.2 as

$$g_k(W|X_k) = \mathcal{PS}(|W|; \gamma_k) \prod_{j=1}^{|W|} \mathcal{N}(z_j; H_k x_k^c, \Sigma_k) \tag{4.8.9}$$

where $\mathcal{PS}$ represents a Poisson distribution to capture the number of observations

generated form the ET object with rate parameter γ_k, H_k is measurement matrix and

Σ_k is the covariance of the Cartesian coordinates of control points of the ET object.

Then, by substituting the likelihood function (4.8.9) and the predicted density

(4.8.7) into (4.8.8) and applying the product formula for the normal densities, as

documented in Appendix 4.11.2, the updated intensities are computed by

$$v_k(X_k|Z_{1:k}) = \sum_{j=1}^{J_{k|k}} \omega_{k|k}^{(j)} \Gamma(\gamma_k, \alpha_{k|k}^{(j)}, \beta_{k|k}^{(j)}) \times \mathcal{N}(x_k^c; m_{k|k}^{(j)}, P_{k|k}^{(j)} + \Sigma_{k|k}^{(j)}) \times \mathbb{S}(x_k^s; \mathbb{P}_{k|k})$$

$$= \sum_{j=1}^{J_{k|k-1}} \omega_{k|k,z^-}^{(j)} \Gamma(\gamma_k, \alpha_{k|k,z^-}^{(j)}, \beta_{k|k,z^-}^{(j}) \times \mathcal{N}(x_k^c; m_{k|k,z^-}^{(j)}, P_{k|k,z^-}^{(j)} + \Sigma_{k|k,z^-}^{(j)}) \times \mathbb{S}(x_k^s; \mathbb{P}_{k|k,z^-}) +$$

$$\sum_{W(Z_k)\in\mathcal{P}_i(Z_k)} \sum_{W\in W(Z_k)} \sum_{j=1}^{J_{k|k-1}} \omega_{k|k}^{(j)}(W) \Gamma(\gamma_k, \alpha_{k|k}^{(j)}(W), \beta_{k|k}^{(j}(W)) \times \mathcal{N}(x_k^c; m_{k|k}^{(j)}(W), P_{k|k}^{(j)}(W)$$

$$+ \Sigma_k^{(j)}(W)) \times \mathbb{S}(x_k^s; \mathbb{P}_{k|k}(\mathbf{z}))$$

$$\tag{4.8.10}$$

where $\mathcal{P}_i$ represents the ith partition that partitions the positive (actual) measure-

ments Z_k into non-vacant cells W and when used under the summation it means that

the summation is over all possible partitions. Also, cell W represents one of the cells belonging to the ith partition and when used under summation it means that the summation is over all cells in the corresponding partition. In the above, $J_{k|k}$ is the updated number of components, $J_{k|k-1}$ is the predicted number of components, $w_{k|k}^{(j)}$ is the weight of the jth component, and $\mathbf{z}^-$ represents negative observations. Each set of the components in the correction equation in (4.8.10) is updated based on the following procedure whose details are given in Appendix 4.11.3. The jth component with weight $\omega_{k|k,z^-}^{(j)}$ in the first line of (4.8.10) and its sufficient statistics $X_{k|k,z^-}^{(j)}$, which are the result of updating with negative measurement if occluded and conventional missed detection in case of no occlusion, are calculated below. Note that the nonlinearity of the negative measurement update step is handled using the unscented Kalman filter (UKF) [107], since the measurement equation (4.7.2) for negative measurements is highly nonlinear and exact equations are not available. Then,

$$\bar{z}^- = \frac{1}{|\mathbf{z}^-|} \sum_{i=1}^{|\mathbf{z}^-|} z_i^- \tag{4.8.11a}$$

$$m_{k|k}^{(j)}(\mathbf{z}^-) = m_{k|k-1}^{(j)} + K^{(j)}(\bar{z}^- - \hat{z}_k^{(j)}), \ \ P_{k|k}^{(j)}(\mathbf{z}^-) = P_{k|k-1}^{(j)} - K^{(j)}P_{z,k}(K^{(j)})^T \tag{4.8.11b}$$

$$\alpha_{k|k,z^-}^{(j)} = \alpha_{k|k-1}^{(j)} \ , \beta_{k|k,z^-}^{(j)} = \beta_{k|k-1}^{(j)} \tag{4.8.11c}$$

147

$$\Sigma_{k|k}^{(j)}(\mathbf{z}^-) = \frac{1}{|\mathbf{z}^-|-1}\sum_{i=1}^{|\mathbf{z}^-|}(z_i^- - \bar{z}^-)(z_i^- - \bar{z}^-)^T, \quad \mathbb{P}_{k|k}(\mathbf{z}^-) = \mathbb{P}_{k|k-1}^{(j)} \qquad (4.8.11d)$$

$$\omega_{k|k,z^-}^{(j)} = (1 - (1 - e^{-\gamma_k^{(j)}})p_D^{(j)})\omega_{k|k-1}^{(j)} \qquad (4.8.11e)$$

where $\bar{z}^-$ is the negative measurement's sample mean and represents the measurement of the occluded ET object center, $m_{k|k-1}^{(j)}$ is the predicted mean, $P_{k|k-1}^{(j)}$ is the predicted covariance, $\alpha_{k|k-1}^{(j)}$ is the predicted shape parameter of gamma distribution, $\beta_{k|k-1}^{(j)}$ is the predicted rate parameter of gamma distribution, $\mathbb{P}_{k|k-1}^{(j)}$ contains the predicted control points of the ET object and $\Sigma_{k|k-1}^{(j)}$ is the predicted covariance of the control points in S-GGM-PHD for the jth component as defined in (4.8.7), $\hat{z}_k$ is the mean of the measurement vector and $P_{z,k}$ is the covariance of the measurement vector, which is calculated using the unscented transformation technique [144]. The Kalman gain $K^{(j)}$ in the UKF framework is calculated by multiplying the cross covariance, $P_{zx,k}$, and inverse of measurement covariance, $P_{z,k}$. The term $(1 - e^{-\gamma^{(j)}})p_D^{(j)}$ is called the effective probability of detection [6] to account for the effect of measurement rate parameter γ_k.

A close look into (4.8.11c)–(4.8.11d) reveals that the measurement rate state γ and the control points $\mathbb{P}$ are kept equal to their predicted values for occluded components and are not updated by the negative measurements. This is due to the fact that the negative measurements are defined to impose the necessary constraints due to the sensor-to-group-target geometry and do not contain any information about the measurement rate or the extent of the occluded ET object.

The jth component with weight $\omega_{k|k}^{(j)}(W)$ in the second line of (4.8.10) is obtained

by processing the positive (actual) measurements. Then,

$$\bar{z} = \frac{1}{|W|} \sum_{i=1}^{|W|} z_i \tag{4.8.12a}$$

$$m_{k|k}^{(j)}(W) = m_{k|k-1}^{(j)} + K^{(j)}(\bar{z} - Hm_{k|k-1}^{(j)}), \;\; P_{k|k}^{(j)}(W) = P_{k|k-1}^{(j)} - K^{(j)}S(K^{(j)})^T \tag{4.8.12b}$$

$$\alpha_{k|k}^{(j)}(W) = \alpha_{k|k-1}^{(j)} + |W|, \;\; \beta_{k|k,0}^{(j)}(W) = \beta_{k|k-1}^{(j)} + 1 \tag{4.8.12c}$$

$$\Sigma_{k|k}^{(j)}(W) = \frac{1}{|W|-1} \sum_{i=1}^{|W|}(z_i - \bar{z})(z_i - \bar{z})^T, \;\; \mathbb{P}_{k|k}(W) = \mathbb{P}_{k|k-1}^{(j)} + K^{(j)}(W - H\sum_{r=1}^{|W|}\Theta_r^m \mathbb{P}_{k|k-1}^{(j)}) \tag{4.8.12d}$$

$$\omega_{k|k}^{(j)}(W) = \frac{w_p p_D^{(j)}(X_k) g_k(W|X_k)^{(j)} \omega_{k|k-1}^{(j)}}{d_W \beta_{FA,k}^{|W|}} \tag{4.8.12e}$$

where $\bar{z}$ is the positive measurement sample mean representing the measurement of the ET object center, $\omega_{k|k}^{(j)}(W)$ is the updated weight, $m_{k|k}^{(j)}(W)$ is the updated mean, $P_{k|k}^{(j)}(W)$ is the updated covariance, $\alpha_{k|k}^{(j)}(W)$ is the updated shape parameter of gamma distribution, $\beta k|k^{(j)}(W)$ is the update rate parameter of gamma distribution, $\mathbb{P}_{k|k}^{(j)}(W)$ is the updated control points of the ET object and $\Sigma_{k|k}^{(j)}(W)$ is the updated covariance of the control points of the jth component using the positive measurements in cell W. The details on deriving the likelihood term $g_k(W|X_k)^{(j)}$ in (4.8.12e) is presented

in Appendix 4.11.3. The use of $|W| - 1$ instead of $|W|$ in (4.8.12d) improves the statistical properties of the estimated covariance, resulting in an unbiased estimate whereas using $|W|$ will lead to a biased estimate.

Coefficient w_p, which can be regarded as the probability of the partition $\mathcal{P}$ being the true partition among all possible partitions, is calculated according to

$$w_p = \frac{\prod_{W \in \mathcal{P}} d_W^{(j)}}{\sum_{\mathcal{P}' Z_k} \prod_{W' \in \mathcal{P}'} d_{W'}} \tag{4.8.12f}$$

$$d_W = \delta_{|W|,1} + \sum_{j=1}^{J_{k|k-1}} \frac{p_D^{(j)} g_k^{(j)}(W|X_k) \omega_{k|k-1}^{(j)}}{\beta_{FA,k}} \tag{4.8.12g}$$

where $\delta_{|W|,1}$ is the Kronecker delta.

Once the ET center and rate parameter are updated, the control points that define the extent state of the ET are updated in according to (4.8.12d).

The JPDA data association technique [105] is used to update the control points using the measurements in cell $|W|$. The procedure for calculating Θ_r^m is explained here. First, the validation matrix Ω for the N control points and the measurements in cell $|W|$ is constructed. Assuming that feasible data association events are represented by $\Xi(\hat{\Omega})$, their conditional probability is calculated by the formula proposed in [105] as

$$P\{\Xi(\hat{\Omega})||W|\} = \frac{1}{c} P_0^{\min(N,|W|)-W_a} \prod_{r:\hat{\eta}_{rm}=1} P_{rm} \tag{4.8.13}$$

where W is the set of all measurements in the current partition, c is a normalization constant, W_a is the number of control points detected in this feasible event $\Xi(\hat{\eta})$,

$\eta_{rm} = 1$ indicates that measurement r is associated with control point m in the event and terms P_{rm} and P_0 are calculated according to

$$P_{rm} = \begin{cases} P_d^{(i)}(p_m)\mathcal{N}(\tilde{z}_j^{p_m}; 0, S^{p_m}), & \text{if } \hat{\eta}_{rm} = 1 \\ \\ 0, \text{otherwise} \end{cases} \tag{4.8.14}$$

$$P_0 = (\lambda_k S)(1 - P_d^{(i)}(m)) \tag{4.8.15}$$

where λ_k is the density of clutter, S is the surveillance region area (or volume) and $P_d^{(i)}(m)$ is the calculated probability of detection for control point m given in (4.6.2).

Then, the posteriori probability Θ_r^m that the rth measurement in partition W is the correct measurement arising from the corresponding control point (p_m) is computed from the conditional probability in (4.8.13) according to

$$\Theta_r^m = \sum_{\Xi(\hat{\Omega})} P(\Xi(\hat{\Omega})|W)\hat{\eta}_{rm} \tag{4.8.16}$$

$$\Theta_0^m = 1 - \sum_{r=1}^{m} \Theta_r^m \tag{4.8.17}$$

The summary of the proposed S-GGM-PHD filter update is given in Algorithm 1 given the partitions $\mathcal{P}_i$ generated by a measurement set partitioning algorithm and a predefined threshold $p_{D,\text{th}}$ on the minimum probability of detection to identify the occluded targets.

Since the number of B-spline gamma Gaussian components may increase over time, a pruning and merging step is necessary to keep the number of components low [125].

Algorithm 1 Summary of the update step in the proposed algorithm given partition $\mathcal{P}_i$

Input:$\{\omega_{k|k-1}^{(j)}, m_{k|k-1}^{(j)}, P_{k|k-1}^{(j)}, \alpha_{k|k-1}^{(j)}, \beta_{k|k-1}^{(j)}, \Sigma_{k|k-1}^{(j)}, \mathbb{P}_{k|k-1}^{(j)}\}$ and the measurement set cells $|W| \in \mathcal{P}_i$.

Output:$\{\omega_{k|k}^{(j)}, m_{k|k}^{(j)}, P_{k|k}^{(j)}, \alpha_{k|k}^{(j)}, \beta_{k|k}^{(j)}, \Sigma_{k|k}^{(j)}, \mathbb{P}_{k|k}^{(j)}\}$.

for $j = 1, \ldots, J_{k|k-1}$ **do**

    Compute p_D using (27) and save the value of $p_D^{(j)}$

    if $P_D^{(j)} \leq p_{D,th}$ **then**

        Find the cells in $\mathcal{P}_i$ that have range values less than the jth components range

        Find the two measurements in each cell that correspond to the minimum and the maximum bearings of source of measurements in cell W: $\bar{z}_k = \{z_{k,\min}, z_{k,\max}\}$

        Find the intersection of the line connecting the sensor to $z_{k,\min}$ and $z_{k,\max}$ with the jth component extent state: $\mathbf{z}^-(j)$

        Compute the following using (42(a)–42(e)):

        $\{\omega_{k|k}^{(j)} = \omega_{k|k}^{(j)}(\mathbf{z}^-(j)), m_{k|k}^{(j)} = m_{k|k}^{(j)}(\mathbf{z}^-(j)), P_{k|k}^{(j)} = P_{k|k}^{(j)}(\mathbf{z}^-(j)), \alpha_{k|k}^{(j)} = \alpha_{k|k}^{(j)}(\mathbf{z}^-(j)), \beta_{k|k}^{(j)} = \beta_{k|k}^{(j)}(\mathbf{z}^-(j)), \Sigma_{k|k}^{(j)} = \Sigma_{k|k}^{(j)}(\mathbf{z}^-(j)), \mathbb{P}_{k|k}^{(j)} = \mathbb{P}_{k|k}^{(j)}(\mathbf{z}^-(j))\}$

    else

        Compute the following:

        $\{\omega_{k|k}^{(j)} = (1 - (1 - e^{-\gamma_k^{(j)}})p_D^{(j)})\omega_{k|k-1}^{(j)}, m_{k|k}^{(j)} = m_{k|k-1}^{(j)}, P_{k|k}^{(j)} = P_{k|k-1}^{(j)}, \alpha_{k|k}^{(j)} = \alpha_{k|k-1}^{(j)}, \beta_{k|k}^{(j)} = \beta_{k|k-1}^{(j)}, \Sigma_{k|k}^{(j)} = \Sigma_{k|k-1}^{(j)}, \mathbb{P}_{k|k}^{(j)} = \mathbb{P}_{k|k-1}^{(j)}\}$

    end

end

$l = 0$

for for each $W \in \mathcal{P}_i$ **do**

    $l = l + 1$

    for $j = 1, \ldots, J_{k|k-1}$ **do**

        Compute the following using (43(a)–43(e)):

        $\{\omega_{k|k}^{(l.J_{k|k-1}+j)}, m_{k|k}^{(l.J_{k|k-1}+j)}, P_{k|k}^{(l.J_{k|k-1}+j)}, \alpha_{k|k}^{(l.J_{k|k-1}+j)}, \beta_{k|k}^{(l.J_{k|k-1}+j)}, \Sigma_{k|k}^{(l.J_{k|k-1}+j)},$

        $\mathbb{P}_{k|k}^{(l.J_{k|k-1}+j)}\}$

    end

end

4.9   Simulations

To show the superiority of the proposed method over the state-of-the-art methods in multiple ET tracking application, two different scenarios are considered. Each scenario has multiple ET objects with non-identical kinematic states, extent states and measurement rates. The performance of different methods are evaluated using their run-time, track loss, cardinality and a metric based on the modified optimal sub-pattern assignment (m-OSPA) [123].

Track loss is calculated according to the circular position error probability (CPEP) method [125] as follows:

$$CPEP_k = \frac{1}{\mathcal{X}_k} \sum_{x_k^c \in \mathcal{X}_k} \rho_k(x_k^c, r) \qquad (4.9.1)$$

for some position error radius r, with

$$\rho_k(x_k^c, r) = \text{Prob}\{||\mathcal{H}\hat{x}_k^c - \mathcal{H}x_k^c||_2\} > r \qquad (4.9.2)$$

where $\mathcal{H}$ is the transformation to select only the location indexes of the ET kinematic state, i.e., $\mathcal{H} = \begin{bmatrix} 1 & 0 & 0 & 0 \\ 0 & 0 & 1 & 0 \end{bmatrix}$, and $|| \bullet ||_2$ is the 2-norm operator.

The cardinality estimate is calculated according to the sum of the weights $\sum_l \omega_{k|k}^{(l)}$. The m-OSPA metric is a modification to the conventional OSPA [145]. This metric considers the errors in the estimated measurement rate (γ), in the estimated extent state (x_k^s), in the estimated kinematic state (x_k^c) and in the estimated target cardinality. The distance between the ET measurement rate parameter and the target center

153

is calculated as follows [123]:

$$d_{j,i}^{(c_\gamma)} = \min\left(c_\gamma, |\gamma_k^{(j)} - \hat{\gamma}_{k|k}^{(i)}|\right) \tag{4.9.3}$$

$$d_{j,i}^{(c_{x^c})} = \min\left(c_{x^c}, ||x_k^{c(j)} - \hat{x}_{k|k}^{c(i)}||_2\right) \tag{4.9.4}$$

The distance between the true extent and the estimated extent of ET object is calculated as [16]

$$d_{j,i}^{(c_{x^s})} = \min\left(c_{x^s}, \frac{1}{B}\sum_{}^{B} |r\left(x_k^{s(j)}\right) - r\left(\hat{x}_{k|k}^{s(i)}\right)|^2\right) \tag{4.9.5}$$

where $r(\bullet)$ represents the radial function that calculates the distance of a point on the contour of an object from its distance in a specific angle and B is the number of such points on the contour of the ET object. The constants c_{x^c}, c_γ and c_{x^s} represent the maximum expected error in the center, measurement rate and the extent, respectively. Thus, the distance between the sufficient statistic $X_k^{(j)}$ and $\hat{X}_{k|k}^{(i)}$ is equal to

$$d\left(X_k^{(j)}, \hat{X}_{k|k}^{(i)}\right) = \frac{\omega_\gamma}{c_\gamma}d_{j,i}^{(c_\gamma)} + \frac{\omega_{x^c}}{c_{x^c}}d_{j,i}^{(c_{x^c})} + \frac{\omega_{x^s}}{c_{x^s}}d_{j,i}^{(c_{x^s})} \tag{4.9.6}$$

where $\omega_\gamma + \omega_{x^c} + \omega_{x^s} = 1$.

The optimal assignment $\bar{\pi}$ of order p with cut-off $c = c_{x^c} + c_\gamma + c_{x^s}$ is computed as [145]

$$\bar{\pi} = \arg\min \sum_{i=1}^{N_{X,k}} \left(d_{j,i}^{(c)}\right)^p \tag{4.9.7}$$

$$d_{j,i}^{(c)} = \min\left(c, d\left(X_k^{(j)}, \hat{X}_{k|k}^{(i)}\right)\right) \tag{4.9.8}$$

Thus, the metric m-OSPA to measure the performance of multiple ET target tracking algorithms is given by

$$\text{m-OSPA}_p^{(c)} = \left(\frac{1}{n} \sum_{i=1}^{N_{X,k}} (d_{i,\bar{\pi}(i)}^{(c)})^p + c^p \left(\hat{N}_{X,k} - N_{X,k} \right) \right)^{\frac{1}{p}} \tag{4.9.9}$$

where $\hat{N}_{X,k}$ is the cardinality estimate, which is equal to sum of the weights in this work and the optimal point assignment $(\bar{\pi})$ is calculated using the Hungarian method [146].

To analyze the performance of the proposed algorithm, two existing state-of-the-art ET tracking methods are implemented in addition to the proposed S-GGM-PHD filter. The first existing algorithm used for comparison is the ET Gaussian-mixture PHD (ET-GM-PHD) filter [28], which tracks multiple ET objects and handles situations where the targets are closely spaced. The ET-GM-PHD models the extent of an ET object according to the RM [7] method. The second existing method implemented for comparison is the ET generalized labeled multi-Bernoulli (ET-GLMB) filter [16] for tracking multiple extended targets. In ET-GLMB, the shape of an ET objects is modelled using the B-spline approximation.

The clutter (or false alarm) measurements are generated with $\lambda_k \times S = 50$ in both scenarios, where λ_k is the rate parameter of Poisson distribution and S is the surveillance area in each scenario. Also, the spatial distribution of clutter measurements is assumed uniform over the surveillance area as described in Section 4.8.

4.9.1 Scenario 1

In this scenario, three targets are tracked. All three targets are present during the whole 80 seconds that the scenario lasts. Target 1 follows a straight line path, while target 2 starts with a constant velocity model followed by a moderate constant turn at intersection A. At this time, target 2 blocks the line-of-sight from the sensor to target 1 as illustrated in Figure 4.27. Target 2 continues with the constant velocity model until intersection B and changes to another constant turn model, clearing the line-of-sight from the sensor to target 1, followed by a constant velocity motion. The third target follows a constant velocity model until intersection A and then switches to a constant turn model followed by another constant velocity model.
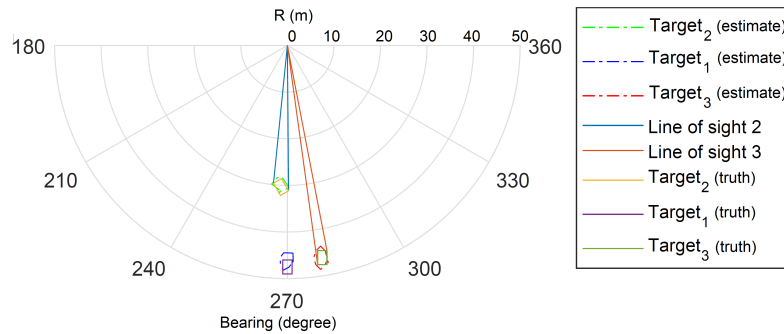
Figure 4.27: Occlusion of target 1 by target 2 at time 12s.

The ET objects' extent and kinematic state estimates in a single run by ET-GM-PHD versus the proposed filter and those by ET-GLMB versus the proposed filter are shown in Figure 4.28 and Figure 4.29, respectively. It can be seen that S-GGM-PHD is able to estimate the center, size, shape and orientation of the targets more accurately compared to the other algorithms. The increased accuracy in the estimated kinematic and extent states is a direct result of incorporating the self-occlusion concept in the update step of proposed filter.

156
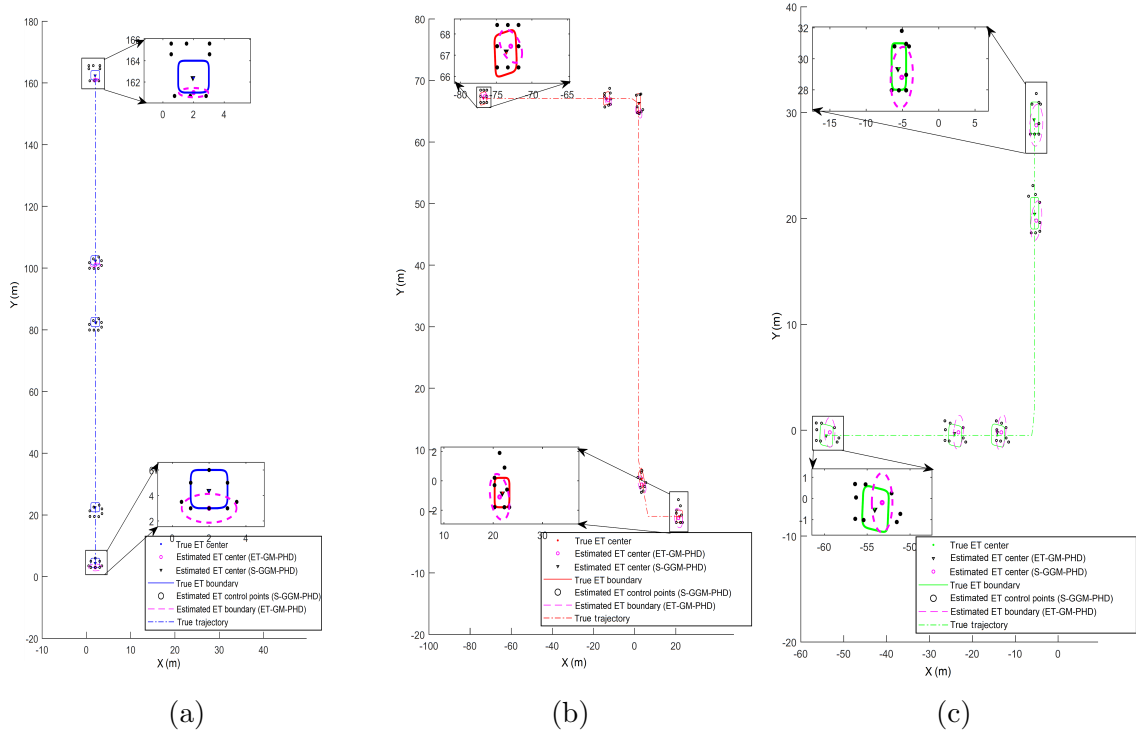
Figure 4.28: The true ET centers and control points along with corresponding estimates by the proposed algorithm and by ET-GM-PHD.

Figure 4.30a and Figure 4.30b illustrates the m-OSPA and CPEP performance metrics of all three algorithms over 100 Monte Carlo runs, respectively. The figures show that the proposed filter outperforms ET-GM-PHD and ET-GLMB in terms of both accuracy of estimates and track loss. The improvement in track continuity is achieved by using an adaptive state-dependent probability of detection in the update step of S-GGM-PHD to mitigate the challenges posed by mutual-occlusion. The proposed algorithm's lower m-OSPA values is a consequence of using a dynamic p_D for each control point contained in the extent state of ET objects and negative measurements.

Figure 4.31 compares the uncertainties in the occluded ET object's (target 1)
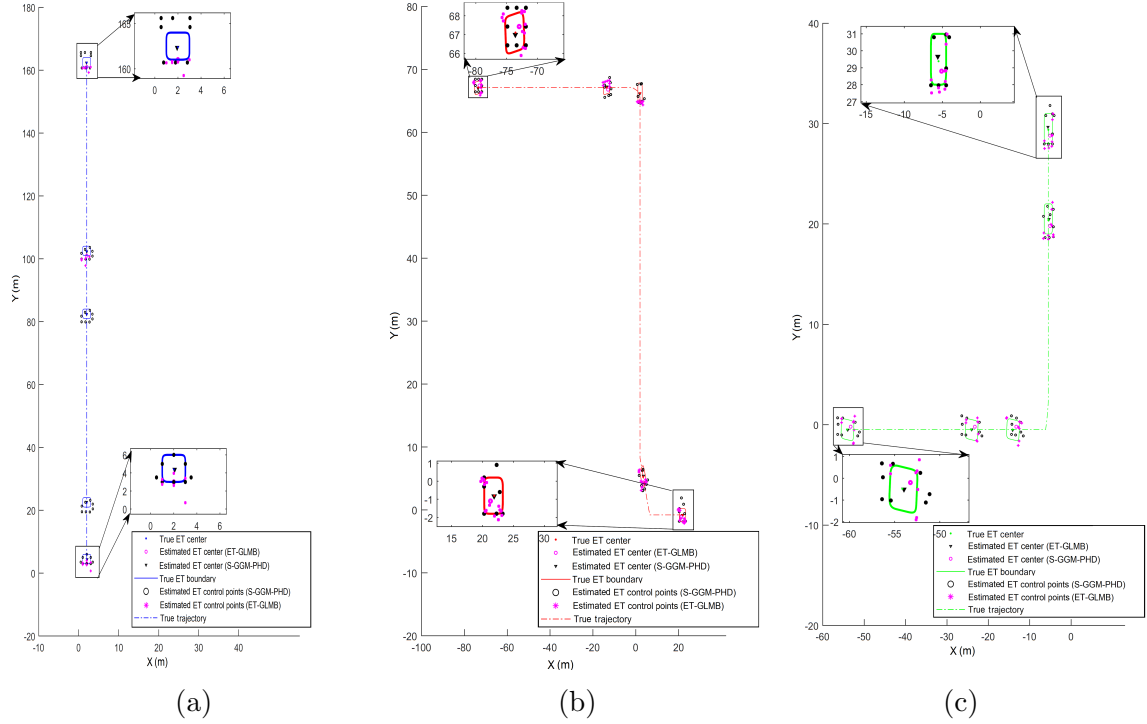
Figure 4.29: The true ET centers and control points along with corresponding estimates by the proposed algorithm and by ET-GLMB.

estimated state by S-GGM-PHD when using the negative measurements versus not using the negative measurements. The uncertainties in the kinematic state and the extreme control points in the ET extent state, which is approximated using the control points of a B-spline curve, are lower when using the negative measurements generated by target 2.

To compare the computational times of three algorithms, false alarm density, which may affect the run-times of algorithms, is set to two different values. The first false alarm rate results in an average of 50 false alarms per scan while the second results in an average of 90 false alarms. The average run-times of the three algorithms over 100 Monte Carlo runs are given in Table 4.11.

(a)   (b)
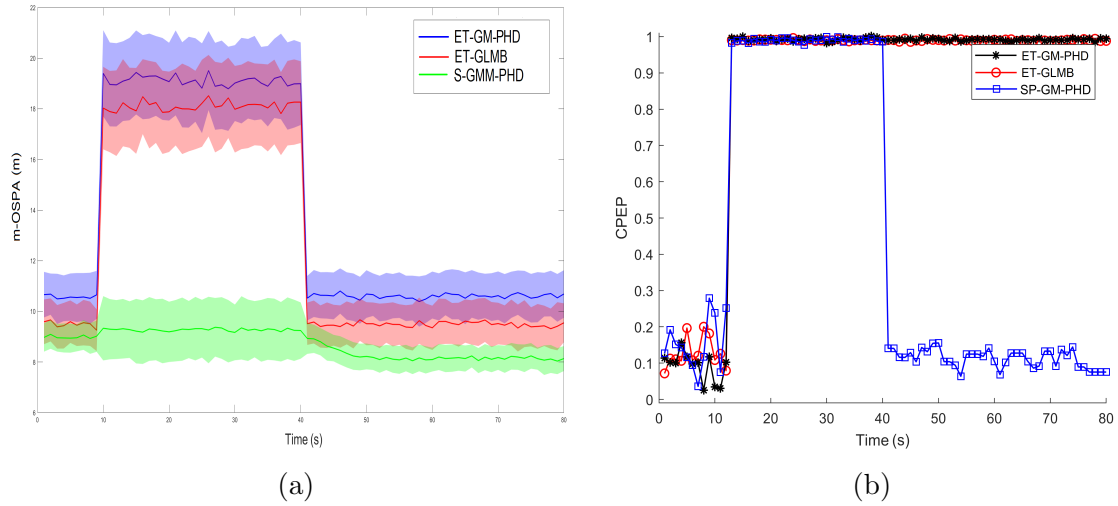
Figure 4.30: (a): m-OSPA measure (solid line) $\pm$ one standard deviation (shaded area) over 100 Monte Carlo runs. (b): CPEP measure over 100 Monte Carlo runs.
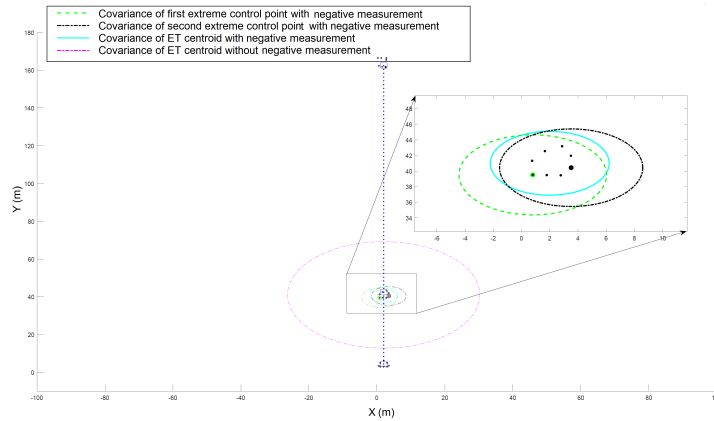
Figure 4.31: The $1 - \sigma$ ellipse with and without negative information for center and two extreme control points of occluded ET (target 1).

Table 4.11: Run-times of algorithms for two different clutter densities

Algorithm	run-time	
	$S \times \lambda_k = 50$	$S \times \lambda_k = 90$
ET-GM-PHD	7.7s	9.01s
ET-GLMB	8.69s	11.01s
S-GGM-PHD	10.37s	11.01s

4.9.2 Scenario 2

In this simulation, there are 6 ET objects during the course of tracking. Each ET object has a different shape, measurement rate and birth/death times. The scenario parameters are given in Table 4.12.

Table 4.12: Target parameters in Scenario 2

Target	Measurement rate γ_k	Target birth time t_b	Target death time t_d
1	17	1s	40s
2	10	1s	100s
3	15	12s	80s
4	20	1s	100s
5	8	75s	100s
6	10	50s	90s

Since not all targets are present for the whole tracking duration, the accuracy of the cardinality estimates are more important than in the previous scenario. The errors in the cardinality estimates are shown in Figure 4.34. Also, in scenario 2, an ET may be occluded by multiple objects, in contrast to scenario 1 where an ET object was occluded only by one other object. Thus, the closest object to the sensor generates negative measurements to impose the constraints on the state of the occluded ET object. Also, in addition to the mobile ET objects, we simulate a stationary obstacle on the road. The location and extent of the obstacle are assumed to be known as
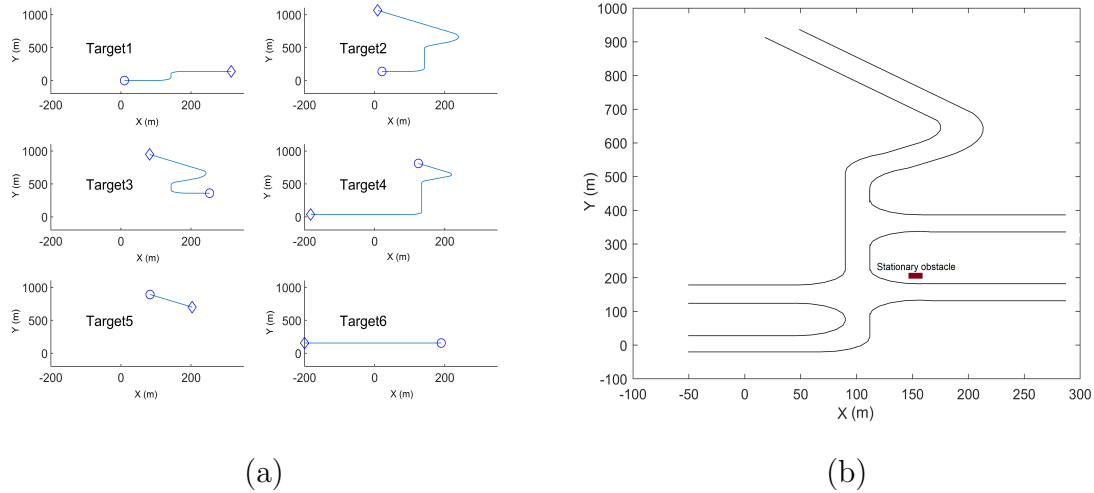
Figure 4.32: (a): The trajectories of existing ET objects. Circle and diamond represent the start and end positions of each ET, respectively. (b): Road map.

prior and are used in generating the negative measurements of occluded objects.

The targets' true trajectories with road maps and the targets' shapes are shown in Figure 4.32 and Figure 4.33, respectively. One snapshot of the results for the exiting targets is depicted in Figure 4.35 for a single run at time 32s. To see how negative measurements can reduce the uncertainties in the state estimates of an occluded ET, the 1-σ ellipse for the occluded object's kinematic state with and without the negative measurements are shown in the magnified window.

Figures 4.36a and 4.36b illustrate the m-OSPA and CPEP performance metrics of the three algorithms over 100 Monte Carlo runs, respectively. Similar to scenario 1, the performance metrics demonstrates that the proposed algorithm outperforms ET-GM-PHD and ET-GLMB in terms of the accuracy of kinematic and extent state estimates, the error in the estimated number of the targets and track loss.

In scenario 2, at least one target is occluded at all times and as a result, the CPEP value does not provide a meaningful measure of the quality of algorithms.

161
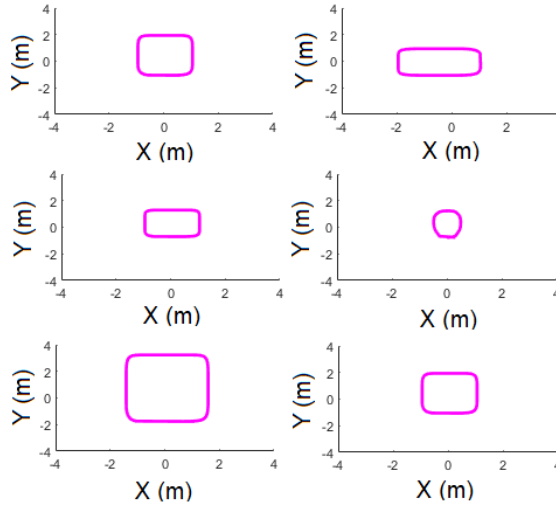
Figure 4.33: Contours of 6 ET objects.
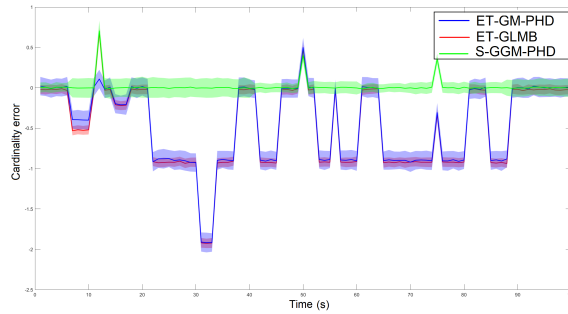
Figure 4.34: Error in the estimated number of ETs.

The average number of track breakages (TB) [147], which quantifies the ability of an algorithm in maintaining track continuity, is then used as an additional metric. The average TB over 100 Monte Carlo runs for the proposed S-GGM-PHD filter is 1.7 compared to the the corresponding values of 11.7 and 12.3 for ET-GM-PHD and ET-GLMB, respectively. The lower value of TB by the proposed algorithm is another indication of improved track continuity in complex environments such as urban areas with occlusions.
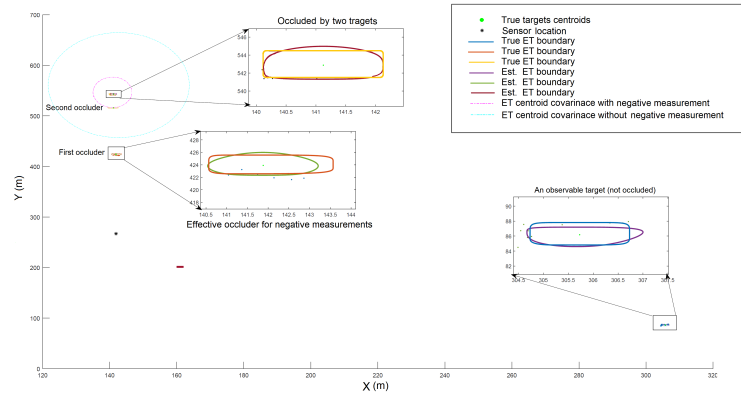
Figure 4.35: Occlusion of one target by two targets at time 32s.

4.10   Conclusions

In this paper, we proposed a new algorithm for tracking multiple extended targets in the presence of clutter and occlusion. The algorithm is based on the probability hypothesis density filter to track the centroids of multiple ET targets and their shapes or extents using a B-spline approximation. The challenges posed by self- and mutual-occlusion are mitigated in the proposed method using the observable arc of each object and an adaptive state-dependent probability of detection, respectively. Another advantage of the proposed algorithm is the use of negative information to bound the uncertainties in estimating the states of occluded objects. The superiority of our method was demonstrated on two realistically simulated scenarios with improved state and shape estimates compared to the existing methods.
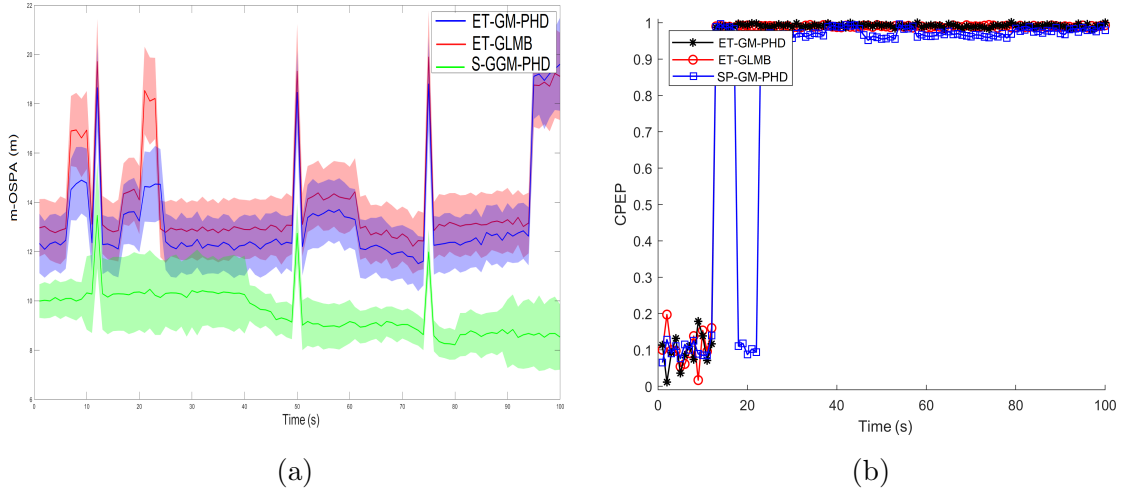
Figure 4.36: (a): m-OSPA measure (solid line) ± one standard deviation (shaded area) over 100 Monte Carlo runs. (b): CPEP measure over 100 Monte Carlo runs.

4.11   Appendices

4.11.1   Probability Of Occlusion

To find the statistics of the conditions for partial and full occlusion in multiple ET object tracking scenarios, we can use some of the properties of the Gaussian distribution. The distribution of the bearing angle corresponding to each control point follows a normal Gaussian distribution, which this is the direct result of the measurement model in (4.5.9). Each condition on the bearing angle of ET objects is constructed from the intersection of two independent conditions on minimum and maximum bearings. The independence among these two allows us to write their joint distribution as a product as

$$p(\phi_A \geq \phi_B) \cap p(\phi'_A \leq \phi'_B) = p(\phi_A \geq \phi_B) \times p(\phi'_A \leq \phi'_B) \tag{4.11.1}$$

164

With Normal distributions, we have [148]

$$p(\phi_A \geq \phi_B) = p(\phi_A - \phi_B \geq 0) = \mathcal{N}(\phi_A - \phi_B; \sigma_{\phi_A}^2 + \sigma_{\phi_B}^2) \qquad (4.11.2)$$

Therefore, we can find the probability of the difference being greater than zero by means of the cumulative distribution function (CDF) of the underlying Gaussian variable as

$$p(\phi_A \geq \phi_B) = \Phi\left(\frac{\phi_A - \phi_B}{\sqrt{\sigma_{\phi_A}^2 + \sigma_{\phi_B}^2}}\right) \qquad (4.11.3)$$

where the CDF of a Normal distribution is equal to

$$\Phi(x) = \frac{1}{2}\left(1 + \mathrm{erf}(\frac{x}{\sqrt{2}})\right) \qquad (4.11.4)$$

4.11.2   Product Formula For Normal Densities

The product of two Normal densities with appropriately dimensioned matrices H, R and P can be calculated according to

$$\mathcal{N}(z; Hx, R)N(x; m, P) =$$
$$\mathcal{N}(z; Hm, S)\mathcal{N}(x; m + G(z - Hm), P - KSK^T) \qquad (4.11.5)$$

where $S = HPH^T + R$ and $K = PH^TS^{-1}$ represents the innovation covariance and the Kalman gain, respectively. Note that matrices P and R are positive definite.

4.11.3   Derivation of The Update Step

According to the measurement model defined in Section 4.5.2, the likelihood of $|W|$ measurements is

$$
g_k(D|X_k) = \mathcal{PS}(|W|; \gamma_k) \prod_{j=1}^{|W|} \mathcal{N}(z_j; Hx_k^c, \Sigma_k)
$$

$$
= \frac{\gamma_k^{|W|} e^{-\gamma_k}}{|W|!} (2\pi)^{\frac{-|W|d}{2}} |\Sigma_k|^{\frac{-|W|}{2}} \times etr\Big(-\frac{1}{2\Sigma_k} \big(\sum_{j=1}^{|W|} (z_j - Hx_k^c)(z_j - Hx_k^c)^T \big) \Big)
$$

$$(4.11.6)$$

where d is the dimension of the kinematic state, $etr(\bullet) = \exp(Trace(\bullet))$, $|\Sigma|$ denotes determinant of Σ and $|W|$ is the number of measurements in partition W. By replacing the kinematic measurement $\bar{z}$ and its spread $C_{\bar{z}} \triangleq \frac{1}{|W|-1} \sum_{j=1}^{|W|} (z - \bar{z})(z - \bar{z})^T$, we can rewrite (4.11.6) as follows:

$$
g_k(D|X_k) = \frac{\gamma_k^{|W|} e^{-\gamma_k}}{|W|!} (2\pi)^{\frac{-|W|d}{2}} |\Sigma_k|^{\frac{-|W|}{2}} \times etr\Big(-\tfrac{1}{2} C_{\bar{z}} \Sigma_k^{-1} \Big) \times etr\Big(-\frac{|W|}{2\Sigma_k} (\bar{z} - Hx_k^c)(\bar{z} - Hx_k^c)^T \Big)
$$

$$
= \frac{\gamma_k^{|W|} e^{-\gamma_k}}{|W|!} (2\pi)^{\frac{-(|W|-1)d}{2}} |\Sigma_k|^{\frac{-(|W|-1)}{2}} |W|^{\frac{-d}{2}} \times etr(-\frac{1}{2} C_{\bar{z}} \Sigma_k^{-1}) \mathcal{N}(\bar{z}; Hx_k^c, \frac{\Sigma_k}{|W|}) \quad (4.11.7)
$$

Then, with the predicted target distribution at time k according to (4.8.7) being equal to

$$
v_{k|k-1}(X) = \Gamma(\gamma_k, \alpha_{k|k-1}, \beta_{k|k-1}) \mathcal{N}(x_k^c; m_{k|k-1}, P_{k|k-1} + \Sigma_k) \mathbb{S}(x_k^s; \mathbb{P}_{k|k-1}) \quad (4.11.8)
$$

the posterior distribution can be calculated by multiplying the predicted distribution (4.11.8) and the measurement likelihood in (4.11.7) according to

$$
\mathrm{v}_k(X|Z_{1:k}) = \frac{\gamma_k^{|W|}e^{-\gamma_k}}{|W|!} \times \Gamma(\gamma_k, \alpha_{k|k-1}, \beta_{k|k-1}) \times (2\pi)^{\frac{-(|W|-1)d}{2}} |\Sigma_k|^{\frac{-(|W|-1)}{2}} |W|^{\frac{-d}{2}} \times
$$

$$
etr(-\frac{1}{2}C_{\bar{z}}\Sigma^{-1}) \times \mathcal{N}(\bar{z}; Hx_k^c, \frac{\Sigma_k}{|W|}) \times \mathcal{N}(x_k^c; m_{k|k-1}, P_{k|k-1} + \Sigma_k) \times \mathbb{S}(x_k^s; \mathbb{P}_{k|k-1})
$$

$$(4.11.9)$$

The first line of (4.11.9) represents the corrected gamma distribution, which is recursively estimated using the sequence of measurement Z_k as follows:

$$
\begin{aligned}
p(\gamma_{k|k}||W|) &= \frac{\gamma_k^{|W|}e^{-\gamma_k}}{|W|!} \times \frac{\beta_{k|k-1}^{\alpha_{k|k-1}}\gamma_k^{\alpha_{k|k-1}+-1}e^{-\beta_{k|k-1}\gamma_k}}{\Gamma(\alpha_{k|k-1})} \\
&= \frac{\beta_{k|k-1}^{\alpha_{k|k-1}}\gamma_k^{\alpha_{k|k-1}+|W|-1}e^{-(\beta_{k|k-1}+1)\gamma_k}}{\Gamma(\alpha_{k|k-1})|W|!} \\
&= \Gamma(\gamma_k, \alpha_{k|k-1}+|W|, \beta_{k|k-1}+1) \times \frac{\Gamma(\alpha_{k|k-1}+|W|)\beta_{k|k-1}^{\alpha_{k|k-1}}}{\Gamma(\alpha_{k|k-1})(\beta_{k|k-1}+1)^{\alpha_{k|k-1}+|W|}W!} \\
&= \Gamma(\gamma_k, \alpha_{k|k-1}+|W|, \beta_{k|k-1}+1) \times \mathcal{L}^{\gamma}(\alpha_{k|k-1}, \beta_{k|k-1}, |W|) \quad (4.11.10)
\end{aligned}
$$

where $\mathcal{L}^{\gamma}$ is the measurement rate likelihood that follows a negative Binomial distribution [149].

The second and the third lines of (4.11.9) capture the corrected Gaussian distribution with the following mean and covariance, which are calculated using the product

formula for Normal densities as described in Appendix 4.11.2. Then,

$$p(x_{k|k}^c|W) = \mathcal{N}(x_{k|k}^c; m_{k|k}, P_{k|k} + \Sigma_k) \qquad (4.11.11a)$$

$$m_{k|k} = m_{k|k-1} + K(\bar{z} - Hm_{k|k-1}) \qquad (4.11.11b)$$

$$P_{k|k} = P_{k|k-1} - KSK^T \qquad (4.11.11c)$$

where $S = HP_{k|k-1}H^T + \frac{1}{|W|}$ and $K = P_{k|k-1}H^TS^{-1}$ are the innovation covariance and the Kalman gain, respectively.

Thus, (4.11.9) becomes

$$v_k(X|Z_{1:k}) = \Gamma(\gamma_k, \alpha_{k|k}, \beta_{k|k}) \times \mathcal{L}^\gamma \times \mathcal{N}(x_{k|k}^c; m_{k|k}, P_{k|k} + \Sigma_k) \times \mathbb{S}(x_k^s; \mathbb{P}_{k|k}) \times \mathcal{L}^{x^{c,s}}$$

$$(4.11.12)$$

where $\mathcal{L}^{x^{c,s}}$ is the likelihood of the kinematic and extent states and $\mathbb{S}$ representing the spline density is the pdf of the control points, which according to measurement model in this work is Gaussian distributed. The updated control points and their covariance are calculated according to

$$\mathbb{P}_{k|k} = \mathbb{P}_{k|k-1} + K(W - H\mathbb{P}_{k|k-1}) \qquad (4.11.13a)$$

$$\Sigma_{k|k} = \frac{1}{|W| - 1} \sum_{j=1}^{W} (z_j - \bar{z})(z_j - \bar{z})^T \tag{4.11.13b}$$

with respect to the data association method described in Section 4.6.

The term $\mathcal{L}^{x^{c,s}}$ can be calculated from (4.11.9) by using the product formula for Gaussian distribution as

$$\mathrm{L}^{x^{c,s}} = (2\pi)^{\frac{-(|W|-1)d}{2}} |\Sigma_k|^{\frac{-(|W|-1)}{2}} |W|^{\frac{-d}{2}} \times etr\left(-\tfrac{1}{2}C_{\bar{z}}\Sigma_k^{-1}\right) \times (2\pi)^{\frac{-d}{2}} |S\Sigma_k|^{-1} etr\left(-\tfrac{1}{2(S\Sigma_k)}(\bar{z} - Hm_{k|k-1})(z - Hm_{k|k-1})^T\right)$$

$$= (2\pi)^{\frac{-|W|d}{2}} |\Sigma_k|^{-\frac{|W|+1}{2}} |W|^{-\frac{d}{2}} |S|^{-1} etr\left(-\tfrac{1}{2}\left(C_{\bar{z}} + S^{-1}(z - Hm_{k|k-1})(z - Hm_{k|k-1})^T\right)\Sigma_k^{-1}\right) \tag{4.11.14}$$

where $|S|$ is the determinant of the innovation matrix S and $|W|$ is the number of measurements in cell W.

Chapter 5

Conclusions and Future Work

5.1   Conclusions

In this thesis, the ET tracking problem in modern sensor applications has been studied. The proposed algorithms try to address some of the major drawbacks in previously developed ET tracking methods.

The non-Gaussian system and sensor noise which can cause divergence in different stages of a tracking algorithms, such as the data association stage and the shape estimation stage, have been addressed through modeling the shape of ET object using the Student's-t process and recursively estimating it using a novel Student's-t extended Kalman filter (EKF). The model takes advantage of the desirable characteristics of the Student's-t distribution like its heavy tails, which can handle outliers and results in a more accurate center and extent estimation in ET object tracking framework.

Considering the previously imposed constraints on the shape of ET objects, a novel shape descriptor using random Polytopes (RP) has been introduced to relax any constraint on the shape of ET objects in chapter 2. Formulating the shape of ET

object with RP concept provides a valuable information that can be used for solving the self-occlusion challenge of ET objects. Using the sensor's current location and current ET estimated shape of ET object the observable parts and non-observable parts can be determined and feed to the proposed filtering method to improve the center and shape estimation results. The proposed RP-based algorithm has been applied to track an ET object both in 2 dimensional and 3 dimensional spaces with self-occlusions and the promising simulation results have been reported.

Due to the nature of real world applications, a multiple ET object tracking method has been introduced in the third chapter, which tries to wrap up all critical conditions which may usually be neglected in ET tracking frameworks. In the proposed method the shape of ET objects are modeled with the help of B-splines. The measurement origin uncertainty is handled using a modified Gaussian mixture probabilistic hypothesis density (GM-PHD) framework which uses a non-constant adaptive probability of detection ,in contrast to the traditional GM-PHD filter, which is calculated according to the ET estimated kinematic state, extent state and sensor's location. Also, the self-occlusion is solved by taking advantage of local controllability provided by B-spline shape descriptors.

5.2   Future Work

The field of ET tracking is an open problem and further researches may be conducted to address the existing challenges and make the algorithm more efficient. To name some of the existing problems, which might be worth working on, we can point to the dependency among the motion models of multiple ET objects, which are present in each scenario. For example, the motion model that a particular vehicle (ET) follows

in a road is dependent to the other vehicles on the road. Some attempts toward defining such models for point targets can be found in [150] but an extension to ET application may be beneficial. Also, exploiting the constraints imposed by the road map [151, 152] as prior can significantly improve the tracking and uncertainty result.

In the development of Student's-t process EKF in chapter 2, we assumed only one ET object is present. The forthcoming extension would be to expand the algorithm to handle multiple ET objects using probabilistic data association (PDA) and random finite set (RFS) frameworks. The same approach can be applied for the method introduced in chapter 3 using RP shape descriptor, since the single ET object assumption also holds there and needs to be expanded to a multitarget case.

The RP method developed in chapter 2 only addresses the troubles caused by self-occlusion in ET tracking. The algorithm can be combined with similar approaches in chapter 4 for handling the mutual-occlusion in a multitarget framework.

One of possible extension to the algorithm proposed in forth chapter is to use the road map, when available, as some additional constraints on existing targets extent and center by using the same negative measurement approach for improving the estimation results.

Bibliography

[1] N. T. Gordon, D. J. Salmond, and D. J. Fisher, "Bayesian target tracking after group pattern distortion," in *Signal and Data Processing of Small Targets 1997*, vol. 3163. International Society for Optics and Photonics, 1997, pp. 238–248.

[2] D. J. Salmond and N. J. Gordon, "Group and extended object tracking," in *Signal and Data Processing of Small Targets 1997*. IET, 1999.

[3] K. Gilholm and D. Salmond, "Spatial distribution model for tracking extended objects," *IEE Proceedings-Radar, Sonar and Navigation*, vol. 152, no. 5, pp. 364–371, 2005.

[4] K. Gilholm, S. Godsill, S. Maskell, and D. Salmond, "Poisson models for extended target and group tracking," in *Signal and Data Processing of Small Targets 2005*, vol. 5913. International Society for Optics and Photonics, 2005, p. 59130R.

[5] A. Swain and D. Clark, "Extended object filtering using spatial independent cluster processes," in *2010 13th International Conference on Information Fusion*. IEEE, 2010, pp. 1–8.

[6] R. Mahler, "PHD filters for nonstandard targets, I: Extended targets," in *2009*

12th International Conference on Information Fusion.   IEEE, 2009, pp. 915–921.

[7] J. W. Koch, "Bayesian approach to extended object and cluster tracking using random matrices," *IEEE Transactions on Aerospace and Electronic Systems*, vol. 44, no. 3, pp. 1042–1059, 2008.

[8] K. Granström, P. Willett, and Y. Bar-Shalom, "An extended target tracking model with multiple random matrices and unified kinematics," in *2015 18th International Conference on Information Fusion.*   IEEE, 2015, pp. 1007–1014.

[9] M. Beard, S. Reuter, K. Granström, B.-T. Vo, B.-N. Vo, and A. Scheel, "Multiple extended target tracking with labeled random finite sets," *IEEE Transactions on Signal Processing*, vol. 64, no. 7, pp. 1638–1653, 2015.

[10] M. Baum and U. D. Hanebeck, "Extended object tracking with random hypersurface models," *IEEE Transactions on Aerospace and Electronic systems*, vol. 50, no. 1, pp. 149–159, 2014.

[11] N. Wahlström and E. Özkan, "Extended target tracking using Gaussian processes," *IEEE Transactions on Signal Processing*, vol. 63, no. 16, pp. 4165–4178, 2015.

[12] Y. Guo, Y. Li, R. Tharmarasa, T. Kirubarajan, M. Efe, and B. Sarikaya, "Gppda filter for extended target tracking with measurement origin uncertainty," *IEEE Transactions on Aerospace and Electronic Systems*, vol. 55, no. 4, pp. 1725–1742, 2018.

[13] W. Aftab, A. De Freitas, M. Arvaneh, and L. Mihaylova, "A Gaussian process convolution particle filter for multiple extended objects tracking with non-regular shapes," in *2018 21st International Conference on Information Fusion*. IEEE, 2018, pp. 1–8.

[14] J.-l. Yang, P. Li, and H.-w. Ge, "Extended target shape estimation by fitting b-spline curve," *Journal of Applied Mathematics*, vol. 2014, 2014.

[15] H. Kaulbersch, J. Honer, and M. Baum, "A Cartesian B-spline vehicle model for extended object tracking," in *2018 21st International Conference on Information Fusion*.   IEEE, 2018, pp. 1–5.

[16] A. Daniyan, S. Lambotharan, A. Deligiannis, Y. Gong, and W.-H. Chen, "Bayesian multiple extended target tracking using labeled random finite sets and splines," *IEEE Transactions on Signal Processing*, vol. 66, no. 22, pp. 6076–6091, 2018.

[17] G. Agamennoni, J. I. Nieto, and E. M. Nebot, "An outlier-robust kalman filter," in *2011 IEEE International Conference on Robotics and Automation*.   IEEE, 2011, pp. 1551–1558.

[18] I. Bilik and J. Tabrikian, "Maneuvering target tracking in the presence of glint using the nonlinear Gaussian mixture Kalman filter," *IEEE Transactions on Aerospace and Electronic Systems*, vol. 46, no. 1, pp. 246–262, 2010.

[19] V. Gay-Bellile, A. Bartoli, and P. Sayd, "Direct estimation of nonrigid registrations with image-based self-occlusion reasoning," *IEEE Transactions on Pattern Analysis and Machine Intelligence*, vol. 32, no. 1, pp. 87–104, 2008.

[20] Y. Cai, N. de Freitas, and J. J. Little, "Robust visual tracking for multiple targets," in *European Conference on Computer Vision*.   Springer, 2006, pp. 107–118.

[21] T. L. Song, D. Musicki, and Y. Kim, "Tracking through occlusions and track segmentation reduction," *IEEE Transactions on Aerospace and Electronic Systems*, vol. 49, no. 1, pp. 623–631, 2013.

[22] A. Andriyenko, S. Roth, and K. Schindler, "An analytical formulation of global occlusion reasoning for multi-target tracking," in *2011 IEEE International Conference on Computer Vision Workshops (ICCV Workshops)*.   IEEE, 2011, pp. 1839–1846.

[23] M. Yang, Y. Liu, L. Wen, Z. You, and S. Z. Li, "A probabilistic framework for multitarget tracking with mutual occlusions," in *Proceedings of the IEEE Conference on Computer Vision and Pattern Recognition*, 2014, pp. 1298–1305.

[24] J. Chen, H. Sheng, C. Li, and Z. Xiong, "Pstg-based multi-label optimization for multi-target tracking," *Computer Vision and Image Understanding*, vol. 144, pp. 217–227, 2016.

[25] R. P. Mahler, "Multitarget Bayes filtering via first-order multitarget moments," *IEEE Transactions on Aerospace and Electronic Systems*, vol. 39, no. 4, pp. 1152–1178, 2003.

[26] B.-T. Vo, B.-N. Vo, and A. Cantoni, "Analytic implementations of the cardinalized probability hypothesis density filter," *IEEE Transactions on Signal Processing*, vol. 55, no. 7, pp. 3553–3567, 2007.

[27] U. Orguner, C. Lundquist, and K. Granström, "Extended target tracking with a cardinalized probability hypothesis density filter," in *2011 Proceedings of the 14th International Conference on Information Fusion.*   IEEE, 2011, pp. 1–8.

[28] K. Granstrom, C. Lundquist, and O. Orguner, "Extended target tracking using a Gaussian-mixture PHD filter," *IEEE Transactions on Aerospace and Electronic Systems*, vol. 48, no. 4, pp. 3268–3286, 2012.

[29] J. L. Williams, "Marginal multi-Bernoulli filters: RFS derivation of MHT, JIPDA, and association-based member," *IEEE Transactions on Aerospace and Electronic Systems*, vol. 51, no. 3, pp. 1664–1687, 2015.

[30] B.-T. Vo and B.-N. Vo, "Labeled random finite sets and multi-object conjugate priors," *IEEE Transactions on Signal Processing*, vol. 61, no. 13, pp. 3460–3475, 2013.

[31] J. Lan and X. R. Li, "Tracking of maneuvering non-ellipsoidal extended object or target group using random matrix," *IEEE Transactions on Signal Processing*, vol. 62, no. 9, pp. 2450–2463, 2014.

[32] K. Granstrom and U. Orguner, "A PHD filter for tracking multiple extended targets using random matrices," *IEEE Transactions on Signal Processing*, vol. 60, no. 11, pp. 5657–5671, 2012.

[33] M. Beard, S. Reuter, K. Granström, B.-T. Vo, B.-N. Vo, and A. Scheel, "Multiple extended target tracking with labeled random finite sets." *IEEE Transactions on Signal Processing*, vol. 64, no. 7, pp. 1638–1653, 2016.

[34] C. E. Rasmussen, "Gaussian processes in machine learning," in *Advanced Lectures on Machine Learning*.   Springer, 2004, pp. 63–71.

[35] A. P. Dawid, "Some matrix-variate distribution theory: Notational considerations and a Bayesian application," *Biometrika*, vol. 68, no. 1, pp. 265–274, 1981.

[36] A. Shah, A. Wilson, and Z. Ghahramani, "Student-*t* processes as alternatives to Gaussian processes," in *Artificial Intelligence and Statistics*, 2014, pp. 877–885.

[37] J. Prüher, F. Tronarp, T. Karvonen, S. Särkkä, and O. Straka, "Student-t process quadratures for filtering of non-linear systems with heavy-tailed noise," in *2017 20th International Conference on Information Fusion*.   IEEE, 2017, pp. 1–8.

[38] N. J. Gordon and A. F. Smith, "Approximate non-Gaussian Bayesian estimation and modal consistency," *Journal of the Royal Statistical Society. Series B (Methodological)*, pp. 913–918, 1993.

[39] S. C. Kramer and H. W. Sorenson, "Recursive Bayesian estimation using piecewise constant approximations," *Automatica*, vol. 24, no. 6, pp. 789–801, 1988.

[40] G. Kitagawa, "Monte Carlo filter and smoother for non-Gaussian nonlinear state space models," *Journal of Computational and Graphical Statistics*, vol. 5, no. 1, pp. 1–25, 1996.

[41] W. Li, Y. Jia, J. Du, and J. Zhang, "PHD filter for multi-target tracking with glint noise," *Signal Processing*, vol. 94, pp. 48–56, 2014.

[42] Y. Huang and Y. Zhang, "Robust Student's t-based stochastic cubature filter for nonlinear systems with heavy-tailed process and measurement noises," *IEEE Access*, vol. 5, pp. 7964–7974, 2017.

[43] G. Agamennoni, J. I. Nieto, and E. M. Nebot, "Approximate inference in state-space models with heavy-tailed noise," *IEEE Transactions on Signal Processing*, vol. 60, no. 10, pp. 5024–5037, 2012.

[44] Y. Huang, Y. Zhang, N. Li, Z. Wu, and J. A. Chambers, "A novel Robust Student's t-based Kalman filter," *IEEE Transactions on Aerospace and Electronic Systems*, vol. 53, no. 3, pp. 1545–1554, 2017.

[45] Z. Zhang, G. Wu, and E. Y. Chang, "Semiparametric regression using student-t processes," *IEEE Transactions on Neural Networks*, vol. 18, no. 6, pp. 1572–1588, 2007.

[46] Q. Tang, T. Dai, L. Niu, Y. Wang, S.-T. Xia, and J. Cai, "Robust survey aggregation with student-t distribution and sparse representation," in *Proceedings of the 26th International Joint Conference on Artificial Intelligence*. AAAI Press, 2017, pp. 2829–2835.

[47] Q. Tang, L. Niu, Y. Wang, T. Dai, W. An, J. Cai, and S.-T. Xia, "Student-t process regression with Student-t likelihood," in *Proceedings of the 26th International Joint Conference on Artificial Intelligence*. AAAI Press, 2017, pp. 2822–2828.

[48] Y.-C. Lu, F. Chen, Y. Wang, and C.-T. Lu, "Discovering anomalies on mixed-type data using a generalized Student-t based approach," *IEEE Transactions on Knowledge and Data Engineering*, vol. 28, no. 10, pp. 2582–2595, 2016.

[49] Y. Zhang, Q. Tang, L. Niu, T. Dai, X. Xiao, and S.-T. Xia, "Self-paced mixture of T distribution model," in *2018 IEEE International Conference on Acoustics, Speech and Signal Processing (ICASSP)*.   IEEE, 2018, pp. 2796–2800.

[50] Y. Wang, F. Liu, S.-T. Xia, and J. Wu, "Link sign prediction by variational bayesian probabilistic matrix factorization with Student-t prior," *Information Sciences*, vol. 405, pp. 175–189, 2017.

[51] Y. Chen, F. Chen, J. Dai, T. C. Clancy, and Y.-J. Wu, "Student-t based robust spatio-temporal prediction," in *2012 IEEE 12th International Conference on Data Mining (ICDM)*.   IEEE, 2012, pp. 151–160.

[52] Y.-C. Lu, F. Chen, Y. Chen, and C.-T. Lu, "A generalized student-t based approach to mixed-type anomaly detection," in *Proceedings of the Twenty-Seventh AAAI Conference on Artificial Intelligence*, ser. AAAI'13.   AAAI Press, 2013, p. 633–639.

[53] M. Lanne and P. Saikkonen, "GMM estimation with non-causal instruments," *Oxford Bulletin of Economics and Statistics*, vol. 73, no. 5, pp. 581–592, 2011.

[54] A. K. Gupta and D. K. Nagar, *Matrix Variate Distributions*.   CRC Press, 2018, vol. 104.

[55] C. E. Rasmussen and C. K. Williams, *Gaussian Process For Machine Learning*.   MIT press, 2006.

[56] M. F. Huber, "Recursive Gaussian process: On-line regression and learning," *Pattern Recognition Letters*, vol. 45, pp. 85–91, 2014.

[57] Z. Wang, J. Q. Shi, and Y. Lee, "Extended t-process regression models," *Journal of Statistical Planning and Inference*, vol. 189, pp. 38–60, 2017.

[58] A. Solin and S. Särkkä, "State space methods for efficient inference in Student-t process regression," in *Artificial Intelligence and Statistics*, 2015, pp. 885–893.

[59] M. Roth, E. Özkan, and F. Gustafsson, "A Student's t filter for heavy tailed process and measurement noise," in *2013 IEEE International Conference on Acoustics, Speech and Signal Processing (ICASSP)*. IEEE, 2013, pp. 5770–5774.

[60] X. Hu, Y.-H. Hu, and B. Xu, "Generalised Kalman filter tracking with multiplicative measurement noise in a wireless sensor network," *IET Signal Processing*, vol. 8, no. 5, pp. 467–474, 2014.

[61] Y. Bar-Shalom and X.-R. Li, *Estimation and Tracking- Principles, Techniques, and Software*. Norwood, MA: Artech House, Inc, 1993., 1993.

[62] B. D. Anderson and J. B. Moore, *Optimal Filtering*. Englewood Cliffs, 1979, vol. 21.

[63] M. Roth, "Kalman filters for nonlinear systems and heavy-tailed noise," Ph.D. dissertation, Linköping University Electronic Press, 2013.

[64] C. M. Bishop, *Pattern Rrecognition and Machine Learning*. Springer, 2006.

[65] P. Dong, Z. Jing, H. Leung, K. Shen, and J. Wang, "Student-t mixture labeled multi-Bernoulli filter for multi-target tracking with heavy-tailed noise," *Signal Processing*, 2018.

[66] R. P. Mahler, *Statistical multisource-multitarget information fusion.* Artech House Norwood, MA, 2007, vol. 685.

[67] Y. Bar-Shalom and E. Tse, "Tracking in a cluttered environment with probabilistic data association," *Automatica*, vol. 11, no. 5, pp. 451–460, 1975.

[68] H. Quan, D. Peng, and J. Li, "Tracking gate algorithm for general nonlinear systems with target class information," *Engineering Review*, vol. 36, no. 1, pp. 1–6, 2016.

[69] P. Tichavsky, C. H. Muravchik, and A. Nehorai, "Posterior Cramér-Rao bounds for discrete-time nonlinear filtering," *IEEE Transactions on Signal Processing*, vol. 46, no. 5, pp. 1386–1396, 1998.

[70] Z. Wang and W. Zhou, "Robust linear filter with parameter estimation under Student-t measurement distribution," *Circuits, Systems, and Signal Processing*, pp. 1–26, 2018.

[71] L. Zuo, R. Niu, and P. K. Varshney, "Conditional posterior Cramér–Rao lower bounds for nonlinear sequential Bayesian estimation," *IEEE Transactions on Signal Processing*, vol. 59, no. 1, pp. 1–14, 2011.

[72] H. L. Van Trees, *Detection, Estimation, and Modulation Theory, part I: Detection, Estimation, and Linear Modulation Theory.* John Wiley & Sons, 2004.

[73] K. Granström, C. Lundquist, and U. Orguner, "Tracking rectangular and elliptical extended targets using laser measurements," in *14th International Conference on Information Fusion*, 2011, pp. 592–599.

[74] Y. Huang, Y. Zhang, N. Li, and J. Chambers, "Robust Student's t based nonlinear filter and smoother," *IEEE Transactions on Aerospace and Electronic Systems*, vol. 52, no. 5, pp. 2586–2596, 2016.

[75] M. Baum and U. D. Hanebeck, "Tracking an extended object modeled as an axis-aligned rectangle." in *GI Jahrestagung*.   Citeseer, 2009, pp. 2422–2427.

[76] L. Sun, X. R. Li, and J. Lan, "Modeling of extended objects based on support functions and extended Gaussian images for target tracking," *IEEE Transactions on Aerospace and Electronic Systems*, vol. 50, no. 4, pp. 3021–3035, 2014.

[77] M. Werman and D. Keren, "A bayesian method for fitting parametric and nonparametric models to noisy data," *IEEE Transactions on Pattern Analysis & Machine Intelligence*, no. 5, pp. 528–534, 2001.

[78] M. Baum and U. D. Hanebeck, "Shape tracking of extended objects and group targets with star-convex rhms," in *14th International Conference on Information Fusion*.   IEEE, 2011, pp. 1–8.

[79] K. Granström, C. Lundquist, and U. Orguner, "A Gaussian mixture PHD filter for extended target tracking," in *2010 13th International Conference on Information Fusion*.   IEEE, 2010, pp. 1–8.

[80] A. Zea, F. Faion, M. Baum, and U. D. Hanebeck, "Level-set random hypersurface models for tracking nonconvex extended objects," *IEEE Transactions on Aerospace and Electronic Systems*, vol. 52, no. 6, pp. 2990–3007, 2016.

[81] N. Corby and J. Mundy, "Applications of range image sensing and processing," in *Analysis and interpretation of range images.* Springer, 1990, pp. 255–272.

[82] F. Faion, A. Zea, M. Baum, and U. D. Hanebeck, "Partial likelihood for unbiased extended object tracking," in *2015 18th International Conference on Information Fusion.* IEEE, 2015, pp. 1022–1029.

[83] D. Cremers, F. R. Schmidt, and F. Barthel, "Shape priors in variational image segmentation: Convexity, lipschitz continuity and globally optimal solutions," in *2008 IEEE Conference on Computer Vision and Pattern Recognition.* IEEE, 2008, pp. 1–6.

[84] S. N. Majumdar, A. Comtet, and J. Randon-Furling, "Random convex hulls and extreme value statistics," *Journal of Statistical Physics*, vol. 138, no. 6, pp. 955–1009, 2010.

[85] R. C. Veltkamp, "Boundaries through scattered points of unknown density," *Graphical Models and Image Processing*, vol. 57, no. 6, pp. 441–452, 1995.

[86] Y. Hosoe, Y. Nagira, and T. Hagiwara, "Random polytope representation of discrete-time uncertain stochastic switched systems and robust stabilization," in *2016 European Control Conference (ECC).* IEEE, 2016, pp. 2029–2034.

[87] R. Deits and R. Tedrake, "Computing large convex regions of obstacle-free space

through semidefinite programming," in *Algorithmic foundations of robotics XI*. Springer, 2015, pp. 109–124.

[88] B. Efron, "The convex hull of a random set of points," *Biometrika*, vol. 52, no. 3-4, pp. 331–343, 1965.

[89] V. E. Brunel, "Non parametric estimation of convex bodies and convex polytopes," Ph.D. dissertation, Université Pierre et Marie Curie-Paris VI, 2014.

[90] P. M. Gruber and J. M. Wills, *Handbook of Convex Geometry*. North Holland, 1993, vol. 2.

[91] L. Pachter and B. Sturmfels, "Parametric inference for biological sequence analysis," *Proceedings of the National Academy of Sciences*, vol. 101, no. 46, pp. 16 138–16 143, 2004.

[92] Y. Hosoe, T. Hagiwara, and D. Peaucelle, "Robust stability analysis and state feedback synthesis for discrete-time systems characterized by random polytopes," *IEEE Transactions on Automatic Control*, vol. 63, no. 2, pp. 556–562, 2018.

[93] R. Meier, F. Ackermann, G. Herrmann, S. Posch, and G. Sagerer, "Segmentation of molecular surfaces based on their convex hull," in *Proceedings., International Conference on Image Processing*, vol. 3, 1995, pp. 552–555 vol.3.

[94] J. Pardon, "Central limit theorems for uniform model random polygons," *Journal of Theoretical Probability*, vol. 25, no. 3, pp. 823–833, 2012.

[95] K. Böröczky, M. Reitzner *et al.*, "Approximation of smooth convex bodies by

random circumscribed polytopes," *The Annals of Applied Probability*, vol. 14, no. 1, pp. 239–273, 2004.

[96] R. Hartley and A. Zisserman, *Multiple view geometry in computer vision.* Cambridge university press, 2003.

[97] F. Mesadi, E. Erdil, M. Cetin, and T. Tasdizen, "Image segmentation using disjunctive normal bayesian shape and appearance models," *IEEE transactions on medical imaging*, vol. 37, no. 1, pp. 293–305, 2018.

[98] E. W. Weisstein, *CRC concise encyclopedia of mathematics.* Chapman and Hall/CRC, 2002.

[99] R. Seidel, "Constructing higher-dimensional convex hulls at logarithmic cost per face," in *Proceedings of the eighteenth annual ACM symposium on Theory of computing.* ACM, 1986, pp. 404–413.

[100] A. Atamturk, G. L. Nemhauser, and M. W. P. Savelsbergh, "Conflict graphs in solving integer programming problems," *European Journal of Operational Research*, vol. 121, no. 1, pp. 40–55, February 2000.

[101] M. Baum, B. Noack, and U. D. Hanebeck, "Extended object and group tracking with elliptic random hypersurface models," in *2010 13th International Conference on Information Fusion.* IEEE, 2010, pp. 1–8.

[102] F. Faion, A. Zea, and U. D. Hanebeck, "Reducing bias in bayesian shape estimation," in *17th International Conference on Information Fusion.* IEEE, 2014, pp. 1–8.

[103] M. Baum and U. D. Hanebeck, "Fitting conics to noisy data using stochastic linearization," in *2011 IEEE/RSJ International Conference on Intelligent Robots and Systems.* IEEE, 2011, pp. 2050–2055.

[104] M. Baum, V. Klumpp, and U. D. Hanebeck, "A novel bayesian method for fitting a circle to noisy points," in *2010 13th International Conference on Information Fusion.* IEEE, 2010, pp. 1–6.

[105] T. Fortmann, Y. Bar-Shalom, and M. Scheffe, "Sonar tracking of multiple targets using joint probabilistic data association," *IEEE Journal of Oceanic Engineering*, vol. 8, no. 3, pp. 173–184, 1983.

[106] Y. Bar-Shalom, X. R. Li, and T. Kirubarajan, *Estimation with applications to tracking and navigation: theory algorithms and software.* John Wiley & Sons, 2004.

[107] E. A. Wan and R. Van Der Merwe, "The unscented Kalman filter for nonlinear estimation," in *Proceedings of the IEEE 2000 Adaptive Systems for Signal Processing, Communications, and Control Symposium.* IEEE, 2000, pp. 153–158.

[108] F. Gustafsson, F. Gunnarsson, N. Bergman, U. Forssell, J. Jansson, R. Karlsson, and P.-J. Nordlund, "Particle filters for positioning, navigation, and tracking," *IEEE Transactions on Signal processing*, vol. 50, no. 2, pp. 425–437, 2002.

[109] L. Ljung, "Asymptotic behavior of the extended kalman filter as a parameter estimator for linear systems," *IEEE Transactions on Automatic Control*, vol. 24, no. 1, pp. 36–50, 1979.

[110] M. Kumru and E. Özkan, "3D Extended object tracking using recursive Gaussian processes," in *2018 21st International Conference on Information Fusion*. IEEE, 2018, pp. 1–8.

[111] S. Lee and J. McBride, "Extended object tracking via positive and negative information fusion," *IEEE Transactions on Signal Processing*, vol. 67, no. 7, pp. 1812–1823, 2019.

[112] K. Granström and U. Orguner, "Estimation and maintenance of measurement rates for multiple extended target tracking," in *2012 15th International Conference on Information Fusion*, July 2012, pp. 2170–2176.

[113] N. T. Gordon, D. J. Salmond, and D. J. Fisher, "Bayesian target tracking after group pattern distortion," in *Signal and Data Processing of Small Targets 1997*, vol. 3163, International Society for Optics and Photonics.   SPIE, 1997, pp. 238–248.

[114] M. Wieneke and W. Koch, "Probabilistic tracking of multiple extended targets using random matrices," in *Signal and Data Processing of Small Targets 2010*, O. E. Drummond, Ed., vol. 7698, International Society for Optics and Photonics.   SPIE, 2010, pp. 416–427.

[115] M. Beard, S. Reuter, K. Granström, B. Vo, B. Vo, and A. Scheel, "Multiple extended target tracking with labeled random finite sets," *IEEE Transactions on Signal Processing*, vol. 64, no. 7, pp. 1638–1653, April 2016.

[116] A. De Freitas, L. Mihaylova, A. Gning, M. Schikora, M. Ulmke, D. Angelova, and W. Koch, "A box particle filter method for tracking multiple extended

objects," *IEEE Transactions on Aerospace and Electronic Systems*, vol. 55, no. 4, pp. 1640–1655, August 2019.

[117] W. Aftab, A. De Freitas, M. Arvaneh, and L. Mihaylova, "A Gaussian process convolution particle filter for multiple extended objects tracking with non-regular shapes," in *2018 21st International Conference on Information Fusion*, July 2018, pp. 1–8.

[118] M. Baum, B. Noack, and U. D. Hanebeck, "Mixture random hypersurface models for tracking multiple extended objects," in *2011 50th IEEE Conference on Decision and Control and European Control Conference.* IEEE, 2011, pp. 3166–3171.

[119] H. Zhang, H. Xu, X.-Y. Wang, and W. An, "A PHD filter for tracking closely spaced objects with elliptic random hypersurface models," in *Proceedings of the 16th International Conference on Information Fusion.* IEEE, 2013, pp. 1558–1565.

[120] Y. Wang, V. Puig, and G. Cembrano, "Set-membership approach and Kalman observer based on zonotopes for discrete-time descriptor systems," *Automatica*, vol. 93, pp. 435–443, 2018.

[121] W. Koch, "On exploiting negative sensor evidence for target tracking and sensor data fusion," *Information Fusion*, vol. 8, no. 1, pp. 28–39, 2007.

[122] B. Noack, F. Pfaff, and U. D. Hanebeck, "Optimal Kalman gains for combined stochastic and set-membership state estimation," in *2012 IEEE 51st IEEE Conference on Decision and Control.* IEEE, 2012, pp. 4035–4040.

[123] C. Lundquist, K. Granström, and U. Orguner, "An extended target CPHD filter and a gamma Gaussian inverse Wishart implementation," *IEEE Journal of Selected Topics in Signal Processing*, vol. 7, no. 3, pp. 472–483, June 2013.

[124] P. Diaconis and D. Ylvisaker, "Conjugate priors for exponential families," *The Annals of Statistics*, vol. 7, pp. 269–281, 1979.

[125] B. Vo and W. Ma, "The Gaussian mixture probability hypothesis density filter," *IEEE Transactions on Signal Processing*, vol. 54, no. 11, pp. 4091–4104, 2006.

[126] A. Likas, N. Vlassis, and J. J. Verbeek, "The global k-means clustering algorithm," *Pattern Recognition*, vol. 36, no. 2, pp. 451–461, 2003.

[127] T. De Laet, H. Bruyninckx, and J. De Schutter, "Shape-based online multi-target tracking and detection for targets causing multiple measurements: Variational Bayesian clustering and lossless data association," *IEEE Transactions on Pattern Analysis and Machine Intelligence*, vol. 33, no. 12, pp. 2477–2491, 2011.

[128] A. Ur-Rehman, S. M. Naqvi, L. Mihaylova, and J. A. Chambers, "Multi-target tracking and occlusion handling with learned variational Bayesian clusters and a social force model," *IEEE Transactions on Signal Processing*, vol. 64, no. 5, pp. 1320–1335, 2015.

[129] G. D. Knott, *Interpolating Cubic Splines*. Springer Science & Business Media, 2012, vol. 18.

[130] H. Prautzsch, W. Boehm, and M. Paluszny, *Bézier and B-spline Techniques*. Springer Science & Business Media, 2013.

[131] K. Punithakumar, M. McDonald, and T. Kirubarajan, "Spline filter for multidimensional nonlinear/non-Gaussian Bayesian tracking," in *Signal and Data Processing of Small Targets 2008*, vol. 6969. International Society for Optics and Photonics, 2008, p. 69690K.

[132] S. R. Buss, *3D Computer Graphics: A Mathematical Introduction with OpenGL*. Cambridge University Press, 2003.

[133] L. Piegl and W. Tiller, "Curve and surface constructions using rational B-splines," *Computer-aided Design*, vol. 19, no. 9, pp. 485–498, 1987.

[134] J. Yang, P. Li, Z. Li, and L. Yang, "Multiple extended target tracking algorithm based on Gaussian surface matrix," *Journal of Systems Engineering and Electronics*, vol. 27, no. 2, pp. 279–289, 2016.

[135] E. Pollard, A. Plyer, B. Pannetier, F. Champagnat, and G. Le Besnerais, "GM-PHD filters for multi-object tracking in uncalibrated aerial videos," in *2009 12th International Conference on Information Fusion*, 2009, pp. 1171–1178.

[136] Y. Zhang and H. Ji, "A novel fast partitioning algorithm for extended target tracking using a Gaussian mixture PHD filter," *Signal Processing*, vol. 93, no. 11, pp. 2975–2985, 2013.

[137] M. Yazdian-Dehkordi and Z. Azimifar, "Refined GM-PHD tracker for tracking targets in possible subsequent missed detections," *Signal Processing*, vol. 116, pp. 112–126, 2015.

[138] W. Wu, W. Liu, J. Jiang, L. Gao, Q. Wei, and C. Liu, "GM-PHD filter-based

multi-target tracking in the presence of Doppler blind zone," *Digital Signal Processing*, vol. 52, pp. 1–12, 2016.

[139] C. Li, W. Wang, T. Kirubarajan, J. Sun, and P. Lei, "PHD and CPHD filtering with unknown detection probability," *IEEE Transactions on Signal Processing*, vol. 66, no. 14, pp. 3784–3798, 2018.

[140] D. B. Epstein and A. Marden, "Convex hulls in hyperbolic space, a theorem of sullivan, and measured pleated surfaces," *Analytical and Geometric Aspects of Hyperbolic Space*, vol. 111, pp. 113–253, 1987.

[141] P. Chavali and A. Nehorai, "Concurrent particle filtering and data association using game theory for tracking multiple maneuvering targets," *IEEE Transactions on Signal Processing*, vol. 61, no. 20, pp. 4934–4948, 2013.

[142] L. C. Andrews, *Special Functions of Mathematics for Engineers.* SPIE Press, 1998, vol. 49.

[143] K. Granström and U. Orguner, "Estimation and maintenance of measurement rates for multiple extended target tracking," in *2012 15th International Conference on Information Fusion.* IEEE, 2012, pp. 2170–2176.

[144] S. J. Julier, "The scaled unscented transformation," in *Proceedings of the 2002 American Control Conference*, vol. 6. IEEE, 2002, pp. 4555–4559.

[145] D. Schuhmacher, B.-T. Vo, and B.-N. Vo, "A consistent metric for performance evaluation of multi-object filters," *IEEE Transactions on Signal Processing*, vol. 56, no. 8, pp. 3447–3457, 2008.

[146] C. H. Papadimitriou and K. Steiglitz, *Combinatorial Optimization: Algorithms and Complexity*. Courier Corporation, 1998.

[147] S. Zhang and Y. Bar-Shalom, "Track segment association for GMTI tracks of evasive move-stop-move maneuvering targets," *IEEE Transactions on Aerospace and Electronic Systems*, vol. 47, no. 3, pp. 1899–1914, July 2011.

[148] K. Wyffels and M. Campbell, "Negative information for occlusion reasoning in dynamic extended multiobject tracking," *IEEE Transactions on Robotics*, vol. 31, no. 2, pp. 425–442, 2015.

[149] R. A. Fisher, "The negative binomial distribution," *Annals of Eugenics*, vol. 11, pp. 182–187, 1941.

[150] D. Song, R. Tharmarasa, T. Kirubarajan, and X. N. Fernando, "Multi-vehicle tracking with road maps and car-following models," *IEEE Transactions on Intelligent Transportation Systems*, vol. 19, no. 5, pp. 1375–1386, 2017.

[151] Y. Cheng and T. Singh, "Efficient particle filtering for road-constrained target tracking," *IEEE Transactions on Aerospace and Electronic Systems*, vol. 43, no. 4, pp. 1454–1469, 2007.

[152] C. Hasberg, S. Hensel, and C. Stiller, "Simultaneous localization and mapping for path-constrained motion," *IEEE Transactions on Intelligent Transportation Systems*, vol. 13, no. 2, pp. 541–552, 2011.